Multifunctional Materials based on TTF-PTM dyads: towards new Molecular Switches, Conductors and Rectifiers

Manuel Souto Salom

Tesi doctoral

Programa de Doctorat en Ciència de Materials

Directors

Prof. Jaume Veciana i Dr. Imma Ratera

Departament de Química

Facultat de Ciències

2016

Chapter 4

Towards neutral radical conductors in the solid state

4.1. Introduction

In the last few decades, there has been a large development of organic molecular materials exhibiting high or metallic-like electrical conductivities.[1,2] A major breakthrough in the field of organic conductors came with the discovery of salts of the radical anion formed by the addition of one-electron to the tetracyanoquinodimethane (TCNQ) by Kepler et *al.* in 1960.[3] A second important breakthrough followed with the synthesis of the electron-donor tetrathiafulvalene (TTF) by Wudl and coworkers[4] in 1970 and the discovery by Coleman et *al.*[5] in 1973 of metallic conductivity in TTF-TCNQ charge transfer salts (Figure 4.1a). Since then a vast number of organic conductors has been prepared due to their interesting physical properties and low dimensionalities. In the 1980s, Bechgaard and coworkers reported the first molecular superconductor at ambient pressure, (TMTSF)$_2$ClO$_4$, that exhibits superconductivity at very low temperatures (Figure 4.1b).[6,7]
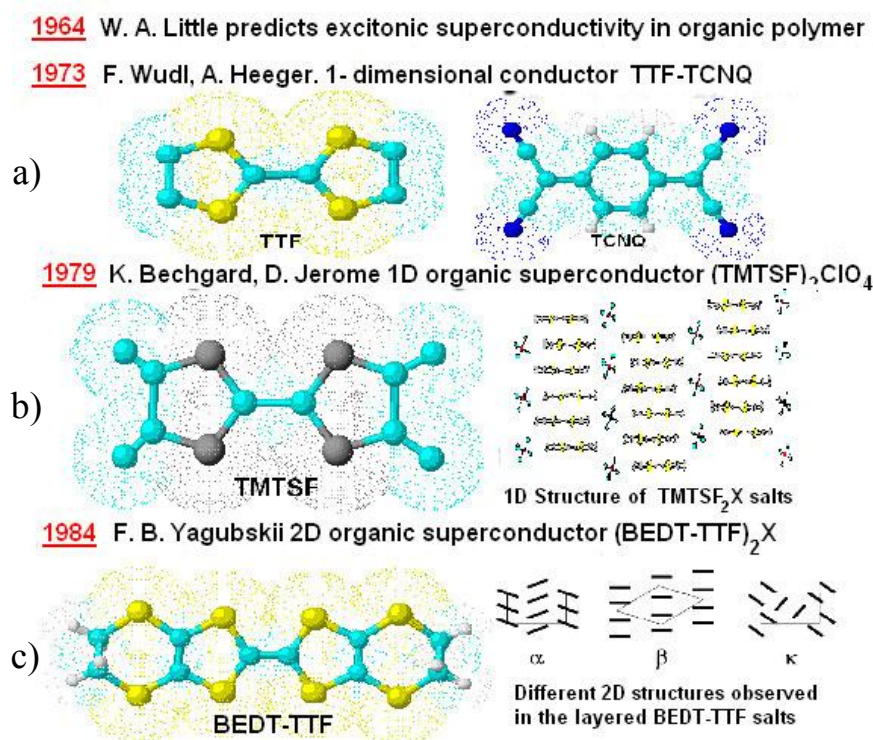

Figure 4.1. Chronological development of organic conductors.

The two-component organic conductors have been classified in two main groups depending on its composition: charge transfer (CT) complexes and ion-radical (IR) salts. The CT complexes are formed by an electron donor and an acceptor with a partial degree of charge transfer and segregated stacking (Figure 4.1a). IR salts are formed by an organic radical and its corresponding counteranion (Figures 4.1b and 4.1c) and must exhibit sufficient degree of spin delocalization and be thermodynamically stable to avoid, for example, disproportionation or dimerization. A large energy gap should prevent the disproportionation of ion radicals into neutral and dication species.

One of the basic requirements for the electronic structure of organic metals components is the presence of unpaired electrons in the donor and/or acceptor molecules through the oxidation of the neutral molecules (p-type doping). On the other hand, an important requisite for the molecular structure is the formation of uniform spacing between donor or acceptor component molecules to permit intermolecular delocalization of the charge and, thus, form partially energy bands at the Fermi level (highest occupied energy level) associated with the overlap of p-orbitals within and between stacks of radical ions. The electrical conductivity (σ) is directly proportional to the number and mobility (μ) of the charge carriers (e) and this will become higher as the overlap between the involved orbitals of the molecules increases. For this reason, building blocks for organic conductors are usually flat molecules with good π-orbital contacts in order to interact in the solid and form energy bands.

On the other hand, organic semiconductors have also received much attention from the field of spintronics which takes advantage of not only the charge, but also the spin of the electron.[8,9] In this sense, there is a high interest in developing organic conducting magnets exhibiting both magnetism and conductivity in a cooperative manner.[10]

4.1.1. Single-component conductors

Besides the well-known cation (or anion) radical organic salts investigated since the 1970s for their conducting (or even superconducting) properties,[11] single-component conductors based on one single neutral radical molecular entity have recently attracted much attention as they offer indeed the possibility for three-dimensional electronic structure, because of the absence of any counterion.[12]

Realization of purely organic single-component conductors is a major challenge chemistry and materials science since purely organic materials are normally insulating. This is mainly due to two main reasons: a) the valence band is completely filled with electrons, and b) a large energy band exists between the valence and conduction bands. From a molecular-level perspective, these reasons correspond to the closed-shell electron configuration of the HOMO (highest occupied molecular orbital) and the large excitation energy from the HOMO to the LUMO (lowest unoccupied molecular orbital), together with the small intermolecular overlap of HOMOs. Then, to produce molecular conductors we should remove (or add) electrons partly from HOMO (to LUMO), and reduce the HOMO–LUMO energy gap and enhance the intermolecular orbital overlap. The first single-component molecular metal was reported in 2001 and based on a nickel complex, [Ni(tmdt)$_2$] (tmdt, trimethylenetetrathiafulvalene dithiolate) (Figure 4.2), in which conductive π-electrons delocalize over the TTF-type large ligand skeleton and the HOMO-LUMO gap becomes smaller.[13] The compact molecular arrangement and intermolecular overlap integrals of the HOMO and the LUMO orbitals revealed that this single-component conductor was a three-dimensional synthetic metal composed of planar molecules.
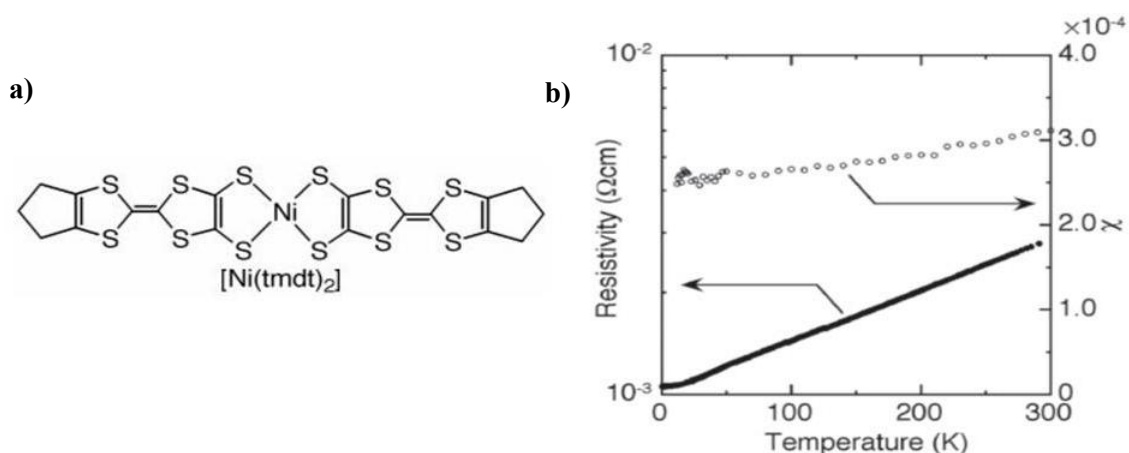
Figure 4.2. a) Molecular structure of [Ni(tmdt)$_2$]. b) Temperature dependence of the resistivity and magnetic susceptibility (χ) of [Ni(tmdt)$_2$] crystals.[13]

Since this first single-component molecular metal, different examples of single-component conductors based on metal complexes have been reported.[12,14–16] Whereas all these examples are based on neutral tetrathiafulvalenedithiolate complexes with metals, during the last decades they have been reported some purely organic neutral radical species that have demonstrated to be a new family of single-component conductors.

4.1.2. Neutral radical conductors

In 1975, Haddon suggested that molecular radicals could represent ideal building blocks towards conductivity since the unpaired electron supplied by a neutral radical can serve as a charge carrier without the need of a previous doping process.[17] However, the neutral-radical system falls into the Mott insulating states due to the intrinsic half-filled nature of the valence band consisting of the singly occupied molecular orbital (SOMO).

The solid state electronic structure of such systems is best described in terms of the half-filled band ($f = 1/2$) Mott-Hubbard model with one electron associated with each radical site. Within this context, one requirement for high conductivity is that intermolecular interactions, expressed in terms of the nearest neighbor resonance integral β, be maximized, and minimize the intra-site Coulomb repulsion energy U. In principle, when the electronic bandwidth W ($= 4\beta$) is sufficient to offset the Coulomb potential ($W > U$) conductivity would take place.[18] In addition to the charge correlation issue, all radicals suffer from a tendency to dimerize in the solid state, either through localized σ-bonds or multicenter π-π interactions.

In this sense, there is a high interest in developing organic radicals as building blocks for single-component materials. From a synthetic perspective, the challenge is to design radicals with enough thermal stability to achieve conductivity. If, for example, the unpaired electron is strongly localized in each radical molecule the system will be insulator. This is the case of radicals with light heteroatoms (N, O), such as nitroxyls, verdazyls, and thiazyls, in which conductivity is very low.[19]

Thus, synthetic efforts to produce conductive radical-based materials have focused on a) the use of highly delocalized organic systems which enjoy a low value of U, and b) the incorporation of heavy (soft) heteroatoms, which can lead to an enhanced bandwidth W. Regarding the first synthetic strategy, phenalenyl and spirophenalenyl radicals recently developed by Haddon and coworkers,[20–28] which exhibit three redox states (cation, radical, and anion), have been widely used for exploring new conjugated organic electronic and magnetic materials. In a spiro-biphenalenyl radical, composed by two phenalenyl rings that are held in perpendicular, the usual superimposed π-stacking arrangement is inhibited and the electronic structure will lead to a one-quarter-filled band in the solid state, minimizing the on-site Coulombic repulsion U. Thus, the availability of the two distinct sites of reduction in the same molecule reduces considerably the disproportionation potential ($\Delta E_{2\text{-}1} = E_2^{1/2} - E_1^{1/2}$) (Figure 4.3).
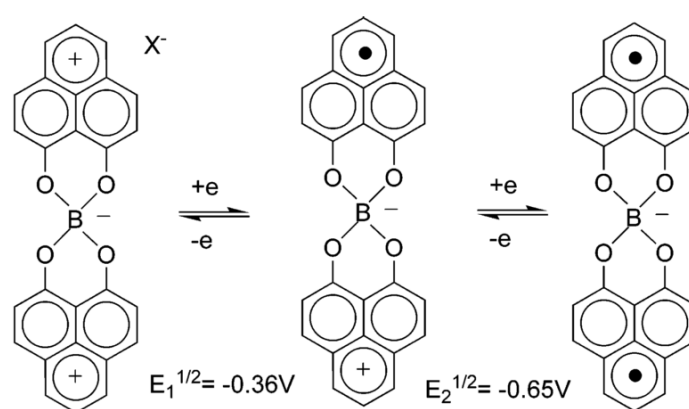

Figure 4.3. The three-redox states of a *spiro*-biphenalenyl radical derivative.[22]

Regarding the second synthetic strategy, Oakley and coworkers have also recently reported several heterocyclic thiazyl radicals (Figure 4.4) that hold considerable potential in the development of conductive and magnetic materials.[18,29–32] In an attempt to balance the potentially conflicting electronic requirements for charge transport and magnetic performance, that is, spin delocalization versus spin localization, they have developed heavy-heteroatom radicals, namely thiazyls and selenazyls, as the presence of nitrogen atoms in spin-bearing sites can suppress dimerization while orbital interactions between neighboring sulfur and selenium atoms, respectively, will generate pathways for charge migration and/ or magnetic coupling. Moreover, some of them can cross the insulator-to-metal state upon application of pressure (Figure 4.5).[18,30–32]
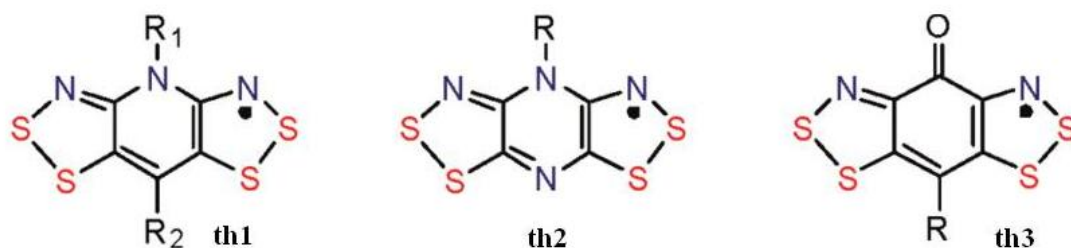

Figure 4.4. Molecular structures of thiazyl radicals (**th1-3**) developed by Oakley and coworkers.[31]
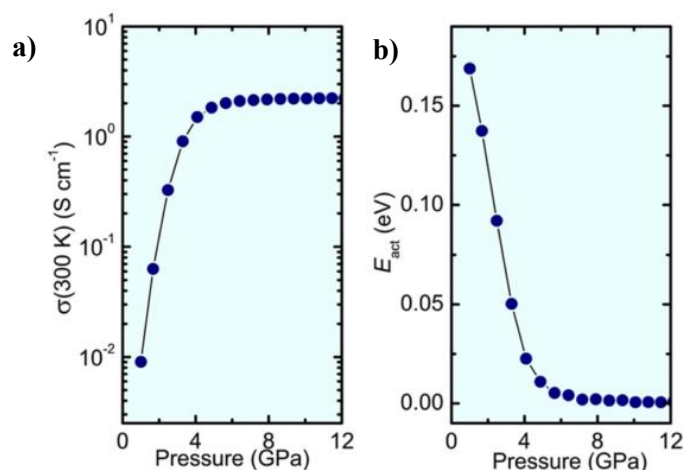
Figure 4.5. Pressure dependence of a) the conductivity σ(300 K) and b) of the thermal activation energy E_{act} of **th3** over the range T = 300−370 K.[32]

On the other hand, Mori and coworkers have very recently reported a new and different type of purely organic single-component conductor based on a catechol-fused ethylenedithiotetrathiafulvalene and its diselena analgoue, (H₂Cat-EDT-TTF and H₂Cat-EDT-ST) (Figure 4.6). This system can exhibit high electrical conductivity due to the hydrogen bond-promoted delocalization of charge carriers upon the partial oxidation of molecules.[33,34]
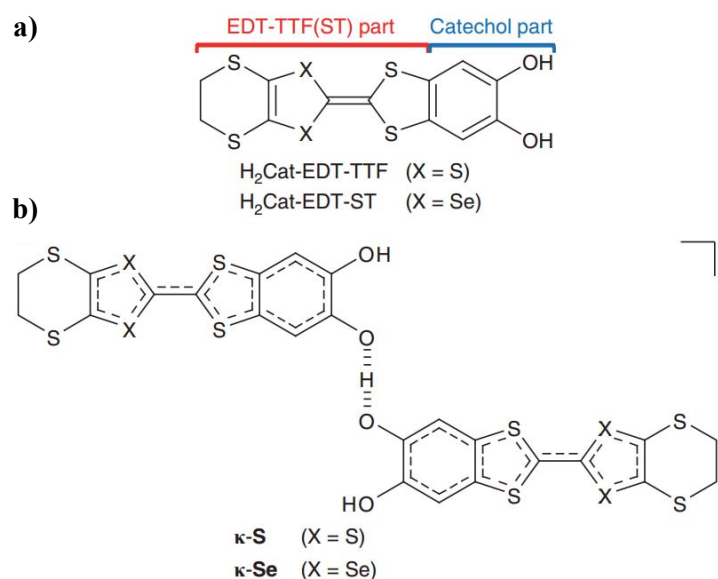

Figure 4.6. a) Chemical structure of H₂Cat-EDT-TTF. b) A hydrogen-bonded molecular unit, (*k*-S).[33]

As we have seen, all the reported examples of neutral organic radicals are based on highly delocalized or planar radicals with low disproportionation energy to offset charge repulsion. However, there are no reported examples of single-component molecular conductors based on non-planar and spin-localized carbon-centered organic radicals due to their weak electronic intermolecular interactions leading to narrow electronic bandwidth and large intra-site electronic repulsion.

4.1.3. Spin-polarized donor radicals

Organic spintronics, which utilizes not only the charge but also the spin of an electron, has received much attention because of its potential application in next-generation electronic systems.[35–37] To achieve this goal, a firm understanding of spin-polarized molecular materials must be established.

During the last decades organic radicals have emerged as building-blocks for spin-polarized magnetic materials. The interest arises in that the spins on the radical sites, when organic radicals are assembled, can interact cooperatively with each other in a regular molecular arrangement and all the spins spontaneously align in parallel at low temperature transforming the organic radical into an organic ferromagnet.[10]

The coexistence of charge transport and spin alignment in an organic molecular assembly was not achieved until 2007 when Sugawara and coworkers reported a radical ion salt of a TTF-based spin-polarized donor radical exhibiting giant negative resistance (the resistance of the salt decreased more than 70% under a magnetic field of 9T at 2 K).[38,39] This system was based on the diselena analogue of the tetrathiafulvalene (TTF)-based spin-polarized donor ESBN that afforded an ion radical salt $ESBN_2ClO_4$ through electrocrystallization (Figure 4.7). This spin-polarized donor radical, in which one-electron oxidation occurs from the HOMO rather than the SOMO, gave rise to a ground-state triplet diradical cation, because of the cross-conjugation between these π-radical and π-donor units.[10,37,40–43]

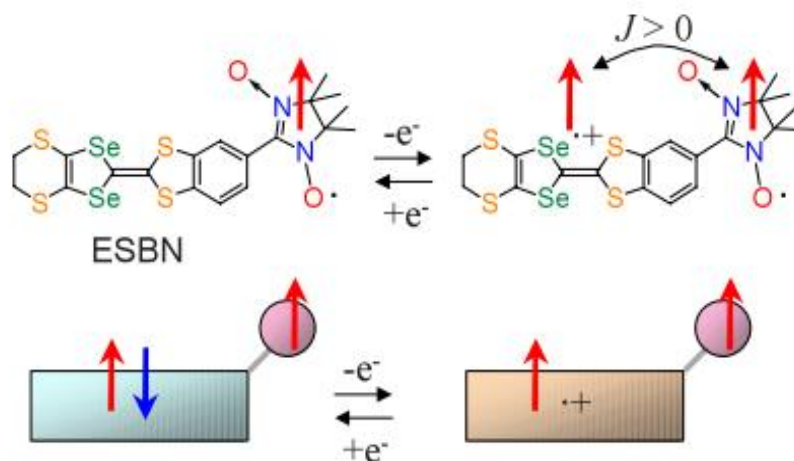**Figure 4.7.** Schematic of the generation of ground-state triplet cation-diradical species of **ESBN** upon one- electron redox process at the donor moiety.[39]

Figure 4.8 schematically shows a plausible mechanism to explain the giant negative magnetoresistance observed in $(ESBN)_2ClO_4$ with nonlinear conducting behavior. In the mixed valence donor column, electron transfer takes place between neighboring molecules, finding the same spin under a low electric field. When a magnetic field was applied, local spins were aligned to suppress the scattering of the conducting electron, causing the giant negative magnetoresistance.
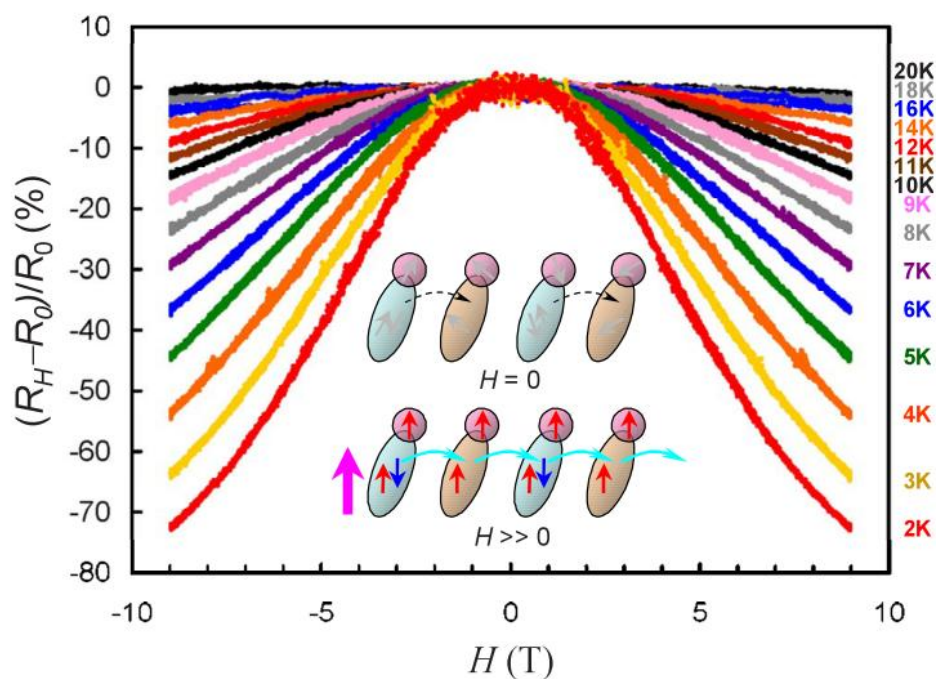
Figure 4.8. Magnetic field dependence of magnetoresistance of $ESBN_2ClO_4$ at various temperatures at a bias voltage of 7 V.[39]

Moreover, Sugawara *et al.* also reported a single-component neutral crystal of BTBN (Figure 4.9) that was conductive upon hole injection from electrodes and the conductance could be controlled by the application of an external magnetic field.[44] The molecule was designed with two bromine atoms into the dithiole ring in order to increase the intermolecular interactions within its crystal.
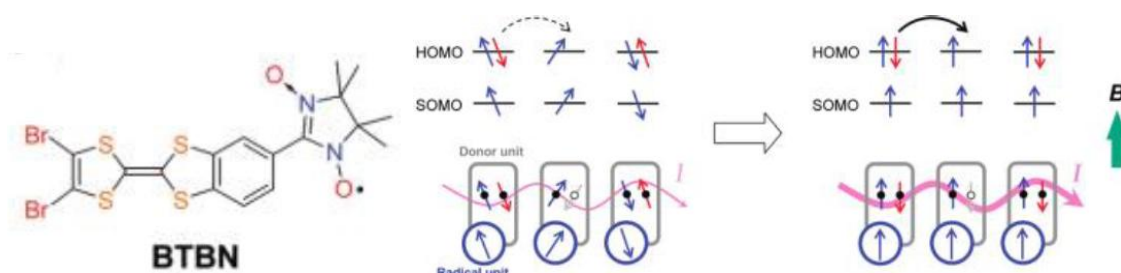

Figure 4.9. Molecular structure of BTBN and plausible mechanism for the increase of conductivity of a spin-polarized donor by the application of an external magnetic field.[44]

4.2. Results and discussion

In view of these interesting physical properties of such spin-polarized donor systems, we aim to design a similar system in which the localized spin will be into a PTM radical moiety that will be directly coupled to a TTF in a conjugated manner. For doing so, we need first to study in detail the self-assembled properties and intermolecular interactions of the TTF-PTM dyads in order to design the proper molecule to obtain an optimal system. As we have seen in Chapter 2, we have synthesized the TTF-PTM radical dyad **1** that could have a potential application for developing a new spin-polarized donor as we can exploit the magnetic properties from the PTM radical unit combined with the conducting properties of the electron-donor (TTF). Unfortunately, up to date, it has not been possible to study in detail its properties in the solid state because of the poor crystalline quality of radical dyad **1** that prevented the determination of its X-ray crystal structure.

4.2.1. Self-assembled architectures with segregated donor and acceptor units of a monopyrrolo-annulated TTF- PTM radical dyad

In order to improve the self-assembly of the TTF moieties of TTF-PTM dyads and their crystalline quality, we have designed the TTF-based radical dyad **5** (Figure 4.10) with a longer bridge between the TTF and PTM units.[45] The increased length of the bridge was obtained using a monopyrrolo-TTF (MPTTF) building block allowing a conjugated phenyl-pyrrole-vinylene ring to be annulated directly to the TTF moiety (see Publication #4).
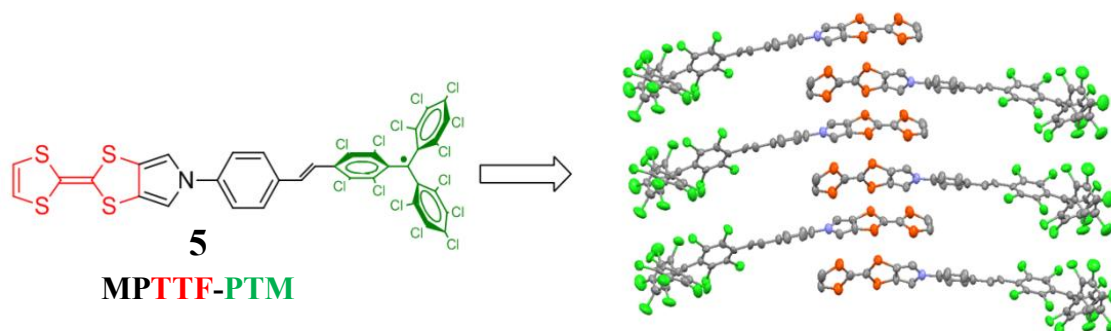

5
MPTTF-PTM

Figure 4.10. Molecular structure and crystal packing of MPTTF-PTM radical (**5**).

In this Chapter, we report the synthesis of this new donor-acceptor radical system **5** followed by its characterization using a variety of techniques including cyclic voltammetry (CV), UV-vis, Raman, and ESR spectroscopies as well as theoretical calculations. These studies reveal that the MPTTF-PTM radical dyad **5** exists in its neutral radical form both in the solid state and in solution rather that in a zwitterionic form. Furthermore, X-ray analysis of dyad **5** revealed an interesting self-assembly architecture with segregated donor and acceptor units that have been analyzed in detail using a variety of techniques.

Regarding the crystal packing, it is important to note that molecules of radical dyad **5** are arranged forming regular 1-D chains of one of the two non-equivalent molecules (**5A** or **5B**) where the MPTTF subunits form a *herringbone* structure along the *b*-axis with S···S short contacts of 3.90 Å (Figure 4.11a). This supramolecular assembly is different over the *a*-axis, where there is no overlap between the S atoms and the stacking is governed by S···Cl and S···C(pyrrole) interactions (Figure 4.11b).
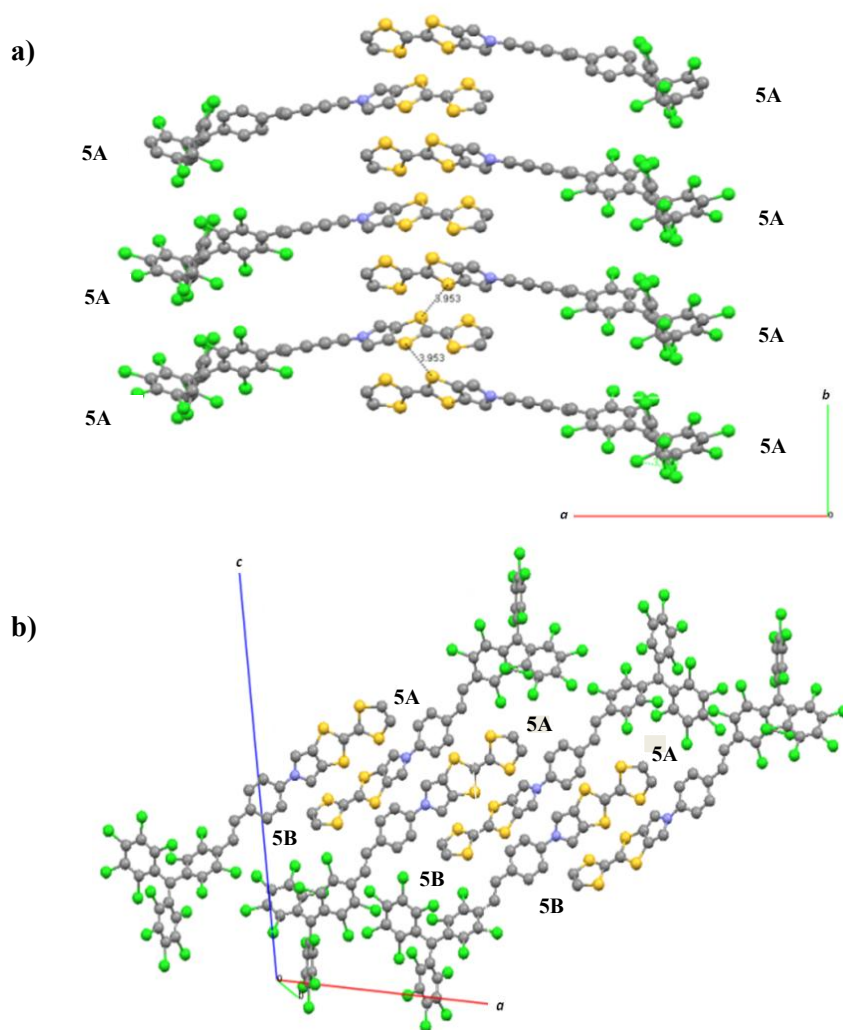

Figure 4.11. Molecular packing of radical dyad **5** at 300 K in the a) *bc* plane and b) *ac* plane.

Finally, analysis of bond lengths reveals opposite changes in the degree of delocalization for the two non-equivalent molecules constituting the crystallographic asymmetric unit when the temperature was decreased. Interestingly, when decreasing the temperature one of the two non-equivalent molecules (**5B**) becomes much more delocalized, as demonstrated by X-ray bond lengths, whereas the other non-equivalent molecule remains less delocalized (**5A**). In accordance with our original design strategy, the increasing of the distance between the MPTTF and PTM moieties has enabled to growth crystals of MPTTF-PTM radical dyad, with a packing in which the donor and the acceptor subunits are segregated and the neighboring MPTTFs show a (modest) degree of interaction.

4.2.2. Pressure-induced conductivity in a neutral non-planar spin-localized radical

As we have seen in the Introduction of this Chapter, there is a growing interest in the development of single-component molecular conductors based on neutral organic radicals that up to now are mainly formed by delocalized planar radicals, such as phenalenyl or thiazolyl radicals. However, there are no examples of systems based on non-planar and spin-localized C-centered radicals exhibiting electrical conductivity due to their large Coulomb energy (U) repulsion and narrow electronic bandwidth (W) that give rise to a Mott insulator behavior.

In the second part of this Chapter (see Publication #5), we present the conducting properties of the neutral radical conductor based on the MPTTF-PTM radical dyad (**5**) presented before. This system becomes semiconducting upon the application of high pressure and conductivity takes place through the radical molecules due to the increased electronic bandwidth W originated from the intermolecular interactions between the TTF units that enhance the overlap between the molecules. We have compared the appearance of conductivity in radical dyad **5** induced by pressure with the Mott insulator behavior that exhibits the unsubstituted perchlorotriphenylmethyl radical **PTM** under the same applied pressures (Figure 4.12). Indeed, the conductivity in dyad **5** could be related to the increasing of the electronic bandwidth W and decreasing of the Coulombic repulsion U due to incorporation of TTF units which force the formation of close packed stacks of radical molecules and enhance the charge delocalization.
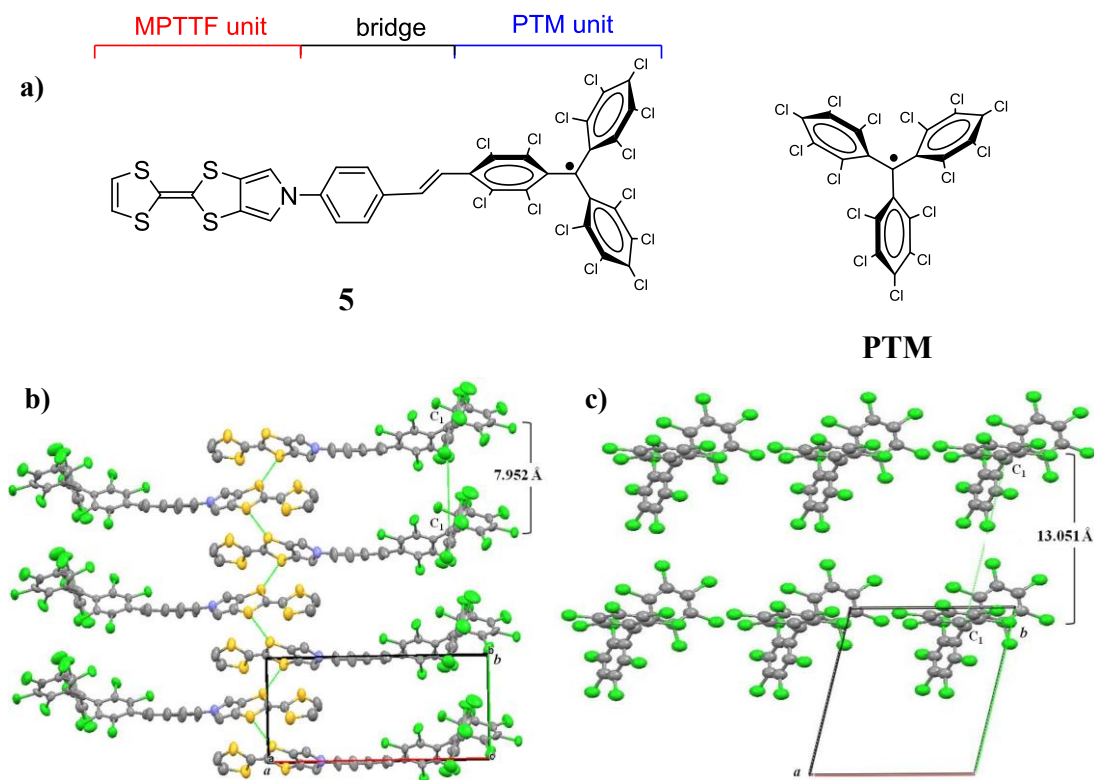

Figure 4.12. a) Molecular structures of radicals **5** and **PTM**. Crystal packing of radicals b) **5** and c) **PTM** on the *ab* plane showing the intermolecular distance between two adjacent PTM molecules.

According to the measurements made by H. Cui (RIKEN, Japan), crystals of **5** showed insulating behavior at ambient pressure while increasing the pressure the room-temperature resistivity rapidly decreased exhibiting a semiconducting behavior throughout the studied temperature range. The conductivity at 15.2 GPa and room temperature was found to be as high as 0.76 S cm^{-1} with a low activation energy (E_a) of 0.067 eV. Moreover, the temperature dependence of the magnetic susceptibility (χ) for the polycrystalline sample was measured over the temperature range of 2-300 K showing a Curie-Weiss behavior (C = 0.394 cm^3 K mol^{-1}) with a $\chi_m T$ at room temperature that fully agrees with the theoretical value of 0.375 expected for non-interacting S = ½ systems (Figure 4.13).
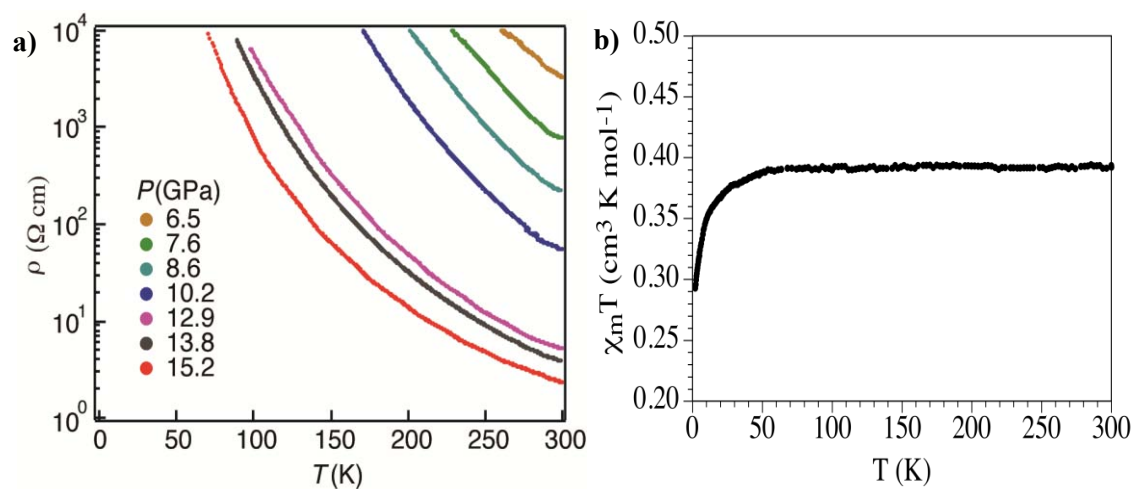

Figure 4.13. a) Temperature dependence of the resistivity of radical dyad **5** along the *b*-axis at different pressures. b) Magnetic susceptibility of crystals of radical dyad **5** as function of temperature.

On the other hand, the electronic bandstructure at ambient pressure (P=0) and P=8.6 GPa were calculated by R. Valenti and coworkers (University of Frankfurt) showing that at P=0 the system is a typical Mott insulator (Figure 4.14). There are four half-filled narrow bands at the Fermi level arising from the four molecules per unit cell of radical dyad **5**. The PTM+bridge region is contributing the majority of the carriers in the valence band with some participation of MPTTF. Upon increasing pressure the bandwidth *W* significantly increases due to enhanced intermolecular overlap and hybridizations and the system becomes more three dimensional. This increase in *W* and molecular hybridizations contributes to the increase of the ratio *W/U* and the appearance of enhanced conductivity at high pressures as observed in our measurements.

At 0 GPa the bandwidth of all four bands at the Fermi level is very narrow (<0.04 eV). However, with pressurization at 8.6 GPa, we observe that the gap in the valence states at -0.05 eV between the bands dominated by TTF orbitals and the bands dominated by PTM orbitals disappears and a wide band manifold of about 0.4 eV. Further compression to 18.9 GPa gives rise to a higher broadening of the bands with bandwidth near 0.8 eV.
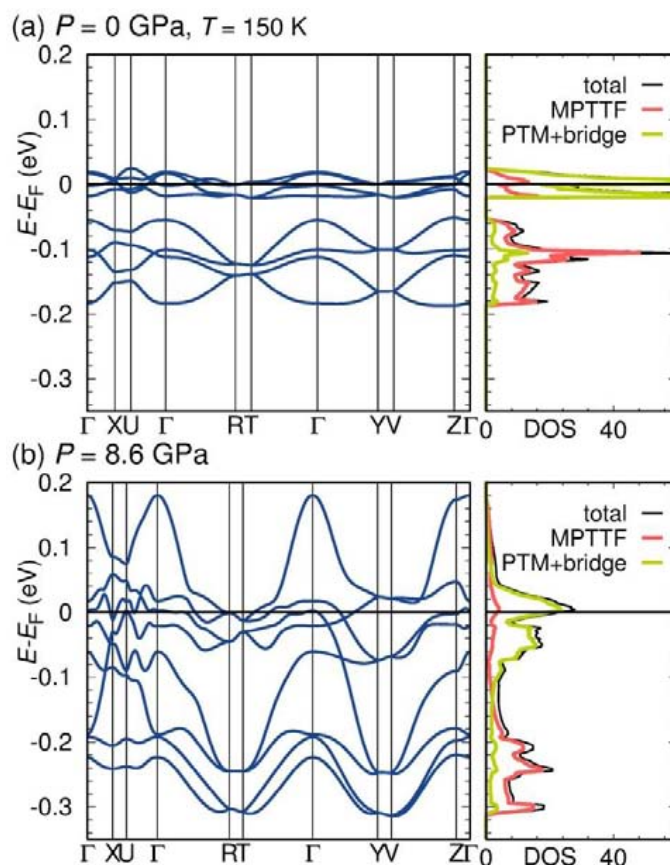
Figure 4.14. Electronic band structures and density of states of radical dyad **5** at (a) ambient pressure (P=0) and (b) P=8.6 GPa.

Moreover, calculations on the evolution of charge transfer in the different units of dyad **5** with pressure are shown in Figure 4.15. We chose to distinguish the PTM together with the phenyl-vinylene bridge as the acceptor unit and the MPTTF as donor unit observing that increasing the pressure, the charge transfer between the two units increases from 0.09e- at ambient pressure to 0.32e- at P = 18 GPa.
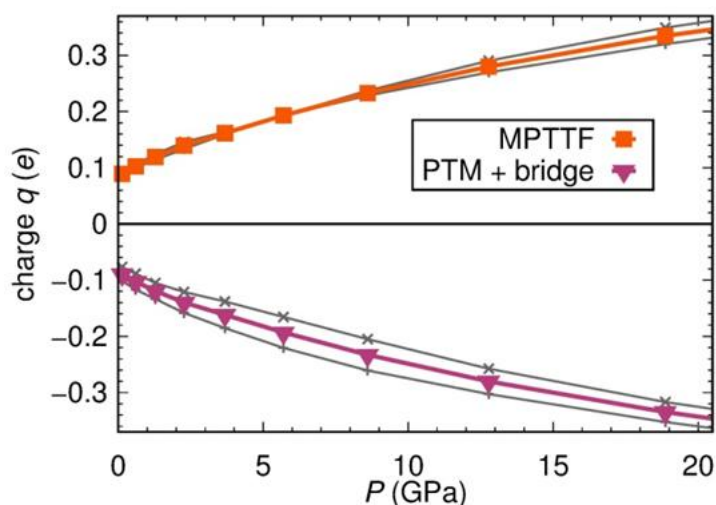

Figure 4.15. Calculated evolution of excess charge within the units of radical dyad **5** with hydrostatic pressure showing the excess of charge on the different units under high pressure.

High-pressure Raman spectroscopy, performed by V. G. Baonza and coworkers (Universidad Complutense de Madrid), supported this charge reorganization in a similar pressure regime in agreement with the decreasing of the electronic Coulomb repulsion. We performed a detailed analysis of the relative intensity variation of the measured Raman bands attributed to the vinylene bridge and those related to the PTM and TTF moieties along the entire pressure range. Figure 4.16 shows that while the system is reorganizing and readjusting the intermolecular spaces up to pressures of 8 GPa, the abrupt change of slope at 8 GPa indicates the presence of important intra- and intermolecular conformational changes that may originate from a crystalline phase transition. Finally, pressure-dependent Raman and photoluminescence measurements, also made by the group of Universidad Complutense, (Figure 4.17) indicated that there is a change in the electronic configuration of the system in agreement with the enhanced planarity of the molecules and the intermolecular reorganization that could hint a possible structural phase transition.
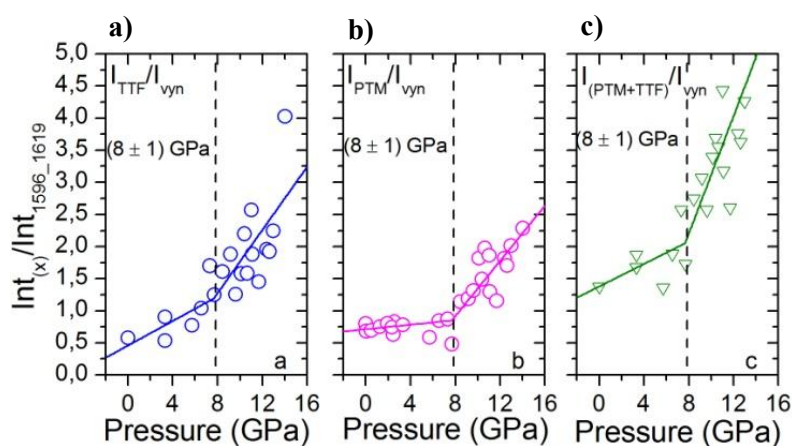
Figure 4.16. Intensity ratio of Raman bands of radical dyad **5** assigned to (a) C=C stretching of TTF/vinylene, (b) C=C stretching of PTM/vinylene bridge, and (c) C=C stretching of TTF+PTM/vinylene.

Figure 4.17. High resolution photoluminescence spectra of crystals of radical dyad **5** at selected pressures when the sample was excited at 532 nm. The sample was supported on a non-drilled gold gasket and compressed using sapphire anvils with a 380 μm culet.

4.3. Summary

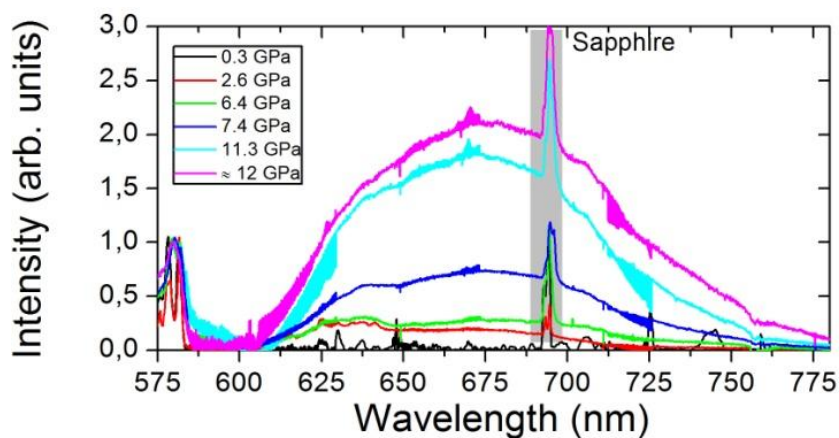In summary, in **Publication #4** we have presented a new electron donor-acceptor dyad based on a PTM radical linked to a TTF unit through a π-conjugated phenyl-pyrrole-vinylene bridge (**5**) that was synthesized and fully characterized. The intramolecular electron transfer (IET) process was evaluated by different spectroscopic techniques and compared with **1** in solution as well as in solid state. These studies reveal that **5** exists in its neutral radical form rather that in a zwitterionic form and the IET was less favored in **5** due to the lower interaction taking place between the D and A subunits because of the increased length of the bridge.

Moreover, we have improved the self-assembly of the TTF moieties and crystallinity thanks to the increased bridge length between the TTF and PTM units. In fact, crystal structure of **5** reveals an interesting self-assembly architecture with segregated D and A units forming a herringbone structure along the *b*-axis governed by S···S short contacts. On the other hand, X-ray crystal analysis at low temperature shows interesting changes in the electron delocalization of the two different non-equivalent molecules of dyad **5**. Whereas at room temperature both non-equivalent molecules exhibit a similar degree of charge delocalization, one of the two inequivalent molecules becomes more delocalized when decreasing the temperature as demonstrated by X-ray analysis bond lengths.

On the other hand, in **Publication#5** we have reported the appearance of conductivity in single crystals of radical dyad **5** induced by pressure in contrast to the Mott insulator behavior of the unsubstituted perchlorotriphenylmethyl **PTM** radical under all applied pressures. The semiconductor behavior of **5** was mainly attributed to the enhanced electronic bandwidth W due to incorporation of TTF units which force the formation of close packed stacks of molecules and to the reduction of the effective Coulomb U interaction attributed to the enhanced electron delocalization in the system due to the incorporation of a substituent donor unit.

Band structure calculations confirmed the significant increase of W in radical dyad **5** as a function of pressure. These calculations suggested important modifications on the electronic structure at pressures above 6-8 GPa with an increase in charge delocalization and of the W/U ratio. These effects were clearly observed in a combined analysis of Raman and DFT calculations under pressure. Moreover, high-pressure Raman and photoluminescence spectroscopy show important configurationally changes that could indicate a change of the crystalline phase when the system is compressed at high pressures.

These results describe a novel strategy that provides an important insight into the design of new radical-based conductors and opens the way to develop new families of purely organic single-component radical conductors. As future outlook, it may be possible to engineer new systems with enhanced intermolecular interactions between the radicals that could exhibit conductivity even without the need for applied pressure. Moreover, the influence of an external magnetic field on the conductance of such systems could be also of high interest.

4.4. References

1.   Farges, J. P. *Organics Conductors: Fundamental and Applications*. (Marcel Dekker, Inc., 1994).

2.   Ferraro, J. R. & Williams, J. M. *Introduction to synthetic electrical conductors*. (Academic Press, Inc., 1987).

3.   Kepler, R. G., Bierstedt, P. E. & Merrifield, R. E. Electronic conduction and exchange interaction in a new class of conductive organic solids. *Phys. Rev. Lett.* **5,** 503–504 (1960).

4.   Wudl, F., Smith, G. M. & Hufnagel, E. J. Unusually Stable Organic Radical. *Chem. Comm.* 1453–1454 (1970).

5.   Coleman, L. B. *et al.* Superconducting fluctuations and the Peierls instability in an organic solid. *Solid State Commun.* **12,** 1125–1132 (1973).

6.   Bechgaard, K., Jacobsen, C. S., Mortensen, K., Pedersen, H. J. & Thorup, N. The properties of five conducting salts: (TMTSF)$_2$X, derived from tetramethyletraselecafulvalene (TMTSF). *Solid State Commun.* **33,** 119–1125 (1980).

7.   Bechgaard, K., Carneiro, K., Rasmussen, F. B. & Olsen, M. Superconductivity in an Organic Solid. Synthesis, Structure, and Conductivity of Bis(tetramethyltetraselenafulva1enium) Perchlorate, (TMTSF)$_2$ClO$_4$. *J. Am. Chem. Soc.* **103,** 2440–2443 (1981).

8.   Dediu, V. A., Hueso, L. E., Bergenti, I. & Taliani, C. Spin routes in organic semiconductors. *Nat. Mater.* **8,** 707–716 (2009).

9.   Sun, D., Ehrenfreund, E. & Vardeny, Z. V. The first decade of organic spintronics research. *Chem. Comm.* **50,** 1781–1793 (2014).

10.   Sugawara, T., Komatsu, H. & Suzuki, K. Interplay between magnetism and conductivity derived from spin-polarized donor radicals. *Chem. Soc. Rev.* **40,** 3105–3118 (2011).

11.   Batail, P. Introduction: Molecular conductors. *Chem. Rev.* **104,** 4887–4890 (2004).

12.   Kobayashi, A., Fujiwara, E. & Kobayashi, H. Single-Component Molecular Metals with Extended-TTF Dithiolate Ligands. *Chem. Rev.* **104,** 5243–5264 (2004).

13.   Tanaka, H., Okano, Y. & Kobayashi, H. A Three-Dimensional Synthetic Metallic Crystal Composed of Single-Component Molecules. *Science* **291,** 285–288 (2001).

14.   Tenn, N., Bellec, N., Jeannin, O., Piekara-sady, L. & Auban-senzier, P. A Single-Component Molecular Metal Based on a Thiazole Dithiolate Gold Complex. *J. Am. Chem. Soc.* **131,** 16961–16967 (2009).

15.   Canadell, E., Lorcy, D., Fourmigue, M., Auban-senzier, P. & Jorge, I. Anisotropic Chemical Pressure Effects in Single-Component Molecular Metals Based on Radical Dithiolene and Diselenolene Gold Complexes. *J. Am. Chem. Soc.* **134,** 17138–17148 (2012).

16.   Higashino, T. *et al.* A Single-Component Conductor Based on a Radical Gold Dithiolene Complex with Alkyl-Substituted Thiophene-2,3-dithiolate Ligand. *Inorg. Chem.* **54,** 9908–9913 (2015).

17.   Haddon, R. C. Design of organic metals and superconductors. *Nature* **256,** 394–396 (1975).

18.	Leitch, A. a. *et al.* From magnets to metals: The response of tetragonal bisdiselenazolyl radicals to pressure. *J. Am. Chem. Soc.* **133,** 6050–6060 (2011).

19.	Hou, Y. *et al.* Organic radicals based on phenalenyl and verdazyl units. *Tetrahedron Lett.* **52,** 3670–3673 (2011).

20.	Pal, S. K. *et al.* Resonating valence-bond ground state in a phenalenyl-based neutral radical conductor. *Science* **309,** 281–284 (2005).

21.	Mandal, S. K. *et al.* Resonating valence bond ground state in oxygen-functionalized phenalenyl-based neutral radical molecular conductors. *J. Am. Chem. Soc.* **128,** 1982–1994 (2006).

22.	Pal, S. K. *et al.* Trisphenalenyl-based neutral radical molecular conductor. *J. Am. Chem. Soc.* **130,** 3942–3951 (2008).

23.	Chi, X. *et al.* Conducting pathways in organic solids: A phenalenyl-based neutral radical of low conductivity. *J. Phys. Chem. B* **106,** 8278–8287 (2002).

24.	Pal, S. K. *et al.* : Substituent Effects on Solid-State Structures and Properties. *J. Am. Chem. Soc.* **129,** 7163–7174 (2007).

25.	Haddon, R. C. *et al.* Localization of spin and charge in phenalenyl-based neutral radical conductors. *J. Am. Chem. Soc.* **130,** 13683–13690 (2008).

26.	Pal, S. K. *et al.* Hysteretic spin and charge delocalization in a phenalenyl-based molecular conductor. *J. Am. Chem. Soc.* **132,** 17258–17264 (2010).

27.	Sarkar, A., Itkis, M. E., Tham, F. S. & Haddon, R. C. Synthesis, structure, and physical properties of a partial p-stacked phenalenyl-based neutral radical molecular conductor. *Chem. - A Eur. J.* **17,** 11576–11584 (2011).

28.	Bag, P. *et al.* Synthesis, structure and solid state properties of benzannulated phenalenyl based neutral radical conductor. *J. Phys. Org. Chem.* **25,** 566–573 (2012).

29.	Brusso, J. L. *et al.* Resonance stabilized bisdiselenazolyls as neutral radical conductors. *J. Am. Chem. Soc.* **128,** 15080–15081 (2006).

30.	Mailman, A. *et al.* Crossing the insulator-to-metal barrier with a thiazyl radical conductor. *J. Am. Chem. Soc.* **134,** 9886–9889 (2012).

31.	Yu, X. *et al.* Semiquinone-bridged bisdithiazolyl radicals as neutral radical conductors. *J. Am. Chem. Soc.* **134,** 2264–2275 (2012).

32.	Wong, J. W. L. *et al.* Pressure induced phase transitions and metallization of a neutral radical conductor. *J. Am. Chem. Soc.* **136,** 1070–1081 (2014).

33.	Isono, T. *et al.* Hydrogen bond-promoted metallic state in a purely organic single-component conductor under pressure. *Nat. Commun.* **4,** 1344–1346 (2013).

34.	Ueda, A. *et al.* Hydrogen-Bond-Dynamics-Based Switching of Conductivity and Magnetism: A Phase Transition Caused by Deuterium and Electron Transfer in a Hydrogen-Bonded Purely Organic Conductor Crystal. *J. Am. Chem. Soc.* **136,** 12184–12192 (2014).

35.	Dau, F. N. Van. The emergence of spin electronics in data storage. *Nat. Mat.* **6,** 813–823 (2007).

36. Boehme, C. & Lupton, J. M. Challenges for organic spintronics. *Nat. Nanotechnol.* **8,** 612–615 (2013).

37. Sugawara, T. & Matsushita, M. M. Spintronics in organic π-electronic systems. *J. Mater. Chem.* **19,** 1738 (2009).

38. Matsushita, M. M., Kawakami, H., Kawada, Y. & Sugawara, T. Negative Magneto-resistance Observed on an Ion-radical Salt of a TTF-based Spin-polarized Donor. *Chem. Lett.* **36,** 110–111 (2007).

39. Matsushita, M. M., Kawakami, H., Sugawara, T. & Ogata, M. Molecule-based system with coexisting conductivity and magnetism and without magnetic inorganic ions. *Phys. Rev. B - Condens. Matter Mater. Phys.* **77,** 1–6 (2008).

40. Kumai, R., Matsushita, M. M., Izuoka, A. & Sugawara, T. Intramolecular Exchange Interaction in a Novel Cross-Conjugated Spin System Composed of π-Ion Radical and Nitronyl Nitroxide. *J. Am. Chem. Soc.* **116,** 4523–4524 (1994).

41. Nakazaki, J., Matsushita, M. M., Izuoka, A. & Sugawara, T. Novel Spin-Polarized TTF Donors Affording Ground State Triplet Cation Diradicals. *Tetrahedron Lett.* **40,** 5027–5030 (1999).

42. Nakazaki, J., Ishikawa, Y., Izuoka, A., Sugawara, T. & Kawada, Y. Preparation of isolable ion-radical salt derived from TTF-based spin-polarized donor. *Chem. Phys. Lett.* **319,** 385–390 (2000).

43. Sakurai, H., Izuoka, a. & Sugawara, T. Design, preparation, and electronic structure of high-spin cation diradicals derived from amine-based spin-polarized donors. *J. Am. Chem. Soc.* **122,** 9723–9734 (2000).

44. Komatsu, H., Matsushita, M. M., Yamamura, S., Sugawara, Y. & Suzuki, K. Influence of Magnetic Field upon Conductance of Unicomponent Crystal of TTF-based Nitronyl Nitroxide. *J. Am. Chem. Soc.* **132,** 4528–4529 (2010).

45. Souto, M. *et al.* Self-Assembled Architectures with Segregated Donor and Acceptor Units of a Dyad Based on a Monopyrrolo-Annulated TTF-PTM Radical. *Chem. - A Eur. J.* **21,** 8816–8825 (2015).

Publication #4

Title: Self-Assembled Architectures with Segregated Donor and Acceptor Units of a Dyad Based on a Monopyrrolo-Annulated TTF–PTM Radical

Authors: Manuel Souto, Marta V. Solano, Morten Jensen, Dan Bendixen, Francesca Delchiaro, Alberto Girlando, Anna Painelli, Jan O. Jeppesen, Concepció Rovira, Imma Ratera, and Jaume Veciana

Publication: *Chem. Eur. J.* 2015, 21, 8816 – 8825

Self-assembled architectures with segregated donor and acceptor units of a dyad based on a monopyrrolo-annulated TTF-PTM radical
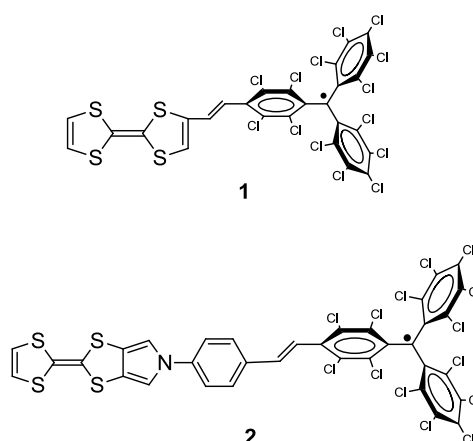
Manuel Souto,[a] Marta V. Solano,[b] Imma Ratera,[a] Morten Jensen,[b] Dan Bendixen,[b] Francesca Delchiaro,[c] Alberto Girlando,[c] Anna Painelli,[c] Jan O. Jeppesen,[b] Concepció Rovira,[a] and Jaume Veciana*[a]

Abstract: An electron donor-acceptor dyad based on a polychlorotriphenylmethyl (PTM) radical subunit linked to a tetrathiafulvalene (TTF) unit through a π-conjugated N-phenyl-pyrrole-vinylene bridge has been synthesized and characterized. The intramolecular electron transfer (IET) process and magnetic properties of the radical dyad have been evaluated by cyclic voltammetry, UV-Vis, vibrational, and ESR spectroscopies both in solution and in the solid state. The self-assembling ability of the radical dyad and of its protonated non-radical analogue has been investigated by X-ray crystallographic analysis which reveals that the radical dyad produces a supramolecular architecture with segregated donor and acceptor units where the TTF subunits are arranged in 1-D herringbone type stacks. Analysis of the X-ray data at different temperatures suggests that the two non-equivalent molecules that form the asymmetric unit of the crystal of the radical dyad evolve into an opposite degree of electronic delocalization as the temperature decrease.

Introduction

Molecules that can be switched between two or more states through the application of an external stimulus (i.e., temperature or light) have attracted a great deal of attention for application in information technology.[1-6] Organic molecules which contain electron donor (D) and electron acceptor (A) units linked by π-conjugated bridging groups (D-π-A dyads) are of interest in this respect on account of the presence of intramolecular electron transfer (IET) processes.[7-11] Some of us have been focused on the study of bistability of several D-A systems made of polychlorotriphenylmethyl (PTM) radicals, as electron acceptors, and ferrocene (Fc) derivatives, as electron donor units. These systems can be switched through an IET from the neutral (N) to the zwitterionic (Z) state by changing the polarity of the surrounding medium and in solvents of intermediate polarity both states can coexist simultaneously.[12-18]

[a]   M. Souto, Dr. I. Ratera, Prof. C. Rovira, Prof. J. Veciana
      Department of Molecular Nanoscience and Organic Materials
      Institut de Ciència de Materials de Barcelona (ICMAB-CSIC)/CIBER-BBN
      Campus Universitari de Bellaterra, 08193 (Barcelona), Spain
      E-mail: jveciana@icmab.es
[b]   Dr. M. V. Solano, M. Jensen, D. Bendixen, Prof. J. O. Jeppesen
      Department of Physics, Chemistry and Pharmacy
   University of Southern Denmark
      5230 Odense M, Denmark
[c]   F. Delchiaro, Prof. A. Girlando, Prof. A. Painelli
      Dipartamento di Chimica
      Parma University/INSTM-UdR Parma
      I-43124 Parma, Italy

      Supporting information for this article is given via a link at the end of the document.

Tetrathiafulvalene (TTF) and its derivatives have been frequently used as donor units in D-A ensembles that are of prime interest on account of their potential applications in electronic and optoelectronic devices.[19-26] More interesting are TTF-based dyads that exhibit molecular packings with a complete segregation of the donor and acceptor fragments forming homo-stacks of TTF subunits. Segregated stacks are in fact a prerequisite for obtaining conducting materials.[27-30] In addition, systems with segregated TTF subunits may bring the opportunity to study the interplay in the solid state between the bistability associated with IET and the intermolecular charge transfer (CT) phenomena typically related with stacks of neutral and/or charged TTF molecules of conducting solids. With this objective in mind, some of us have recently reported a D-A system **1**, which was based on a TTF electron π-donor connected to the PTM electron acceptor by a vinylene bridge (Scheme 1).[31] This radical dyad exists in solution in equilibrium with the homo- and the mixed-valence dimers under the influence of concentration, polarity of the solvent,[31,32] and temperature.[33,34] The appearance of both kinds of aggregates is governed by the reciprocal influence of the IET within the dyad and the intermolecular CT occurring in the dimers between the TTF subunits. Unfortunately, up to date, it has not been possible to study in detail the interplay between the IET and CT in the solid state and its relationship with the molecular packing because of the poor crystalline quality of radical dyad **1** that prevented the determination of its X-ray crystal structure.

Scheme 1. Molecular structures of radical D-A dyads **1** and **2**.

In order to improve the self-assembly of the TTF moieties of TTF-PTM dyads and their crystalline quality, we have designed a new TTF-based radical dyad **2** (Scheme 1) with a longer

bridge between the TTF and PTM units. The increased length of the bridge was obtained using a monopyrrolo-TTF (MPTTF) building block allowing a conjugated *N*-phenyl-pyrrole-vinylene ring to be annulated directly to the TTF moiety.

Herein, we report the synthesis of the new donor-acceptor system based on the MPTTF-PTM radical dyad **2** followed by its characterization carried out using a variety of techniques including cyclic voltammetry (CV), UV-Vis, Raman, and ESR spectroscopies as well as theoretical calculations. These studies reveal that the MPTTF-PTM radical dyad **2** exists in its neutral radical form both in the solid state and in solution rather that in a zwitterionic form. Furthermore, X-ray analysis of dyad **2** revealed an interesting self-assembly architecture with segregated donor and acceptor units that have been analyzed in detail using a variety of techniques. Finally, analysis of bond lengths reveals opposite changes in the degree of delocalization for the two non-equivalent molecules constituting the crystallographic asymmetric unit when the temperature was decreased.

Results and Discussion

Synthesis: Initially, we describe an improved synthesis of the MPTTF derivative[35] **6** before outlining the synthesis of the novel MPTTF-PTM dyad **2**. The synthesis of the MPTTF derivative **6** was carried out as outlined in Scheme 2. Cross-coupling of 1,3-dithiole-2-thione (**3**) and 5-tosyl-(1,3)-dithiolo[4,5-*c*]pyrrole-2-one[36,37] (**4**) in neat $(EtO)_3P$ gave **5** in 71% yield after column chromatography.
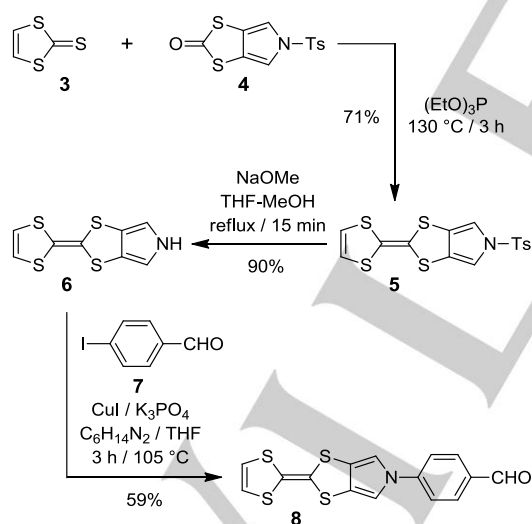
Scheme 2. Synthesis of the *N*-(4-formylphenyl)-MPPTF derivative **8**.

The tosyl protecting group on the MPTTF derivative **5** was removed by using NaOMe in a THF/MeOH mixture producing compound **6** in 90% yield, which subsequently was subjected to a modified Buchwald-Hartwig reaction.[38-40] Thus, by mixing compound **6**, 4-iodobenzaldehyde (**7**), an excess of cuprous iodide (CuI), and *trans*-1,2-diaminocyclohexane ($C_6H_{14}N_2$), the

N-(4-formylphenyl)-MPPTF derivative **8** was obtained (Scheme 2) in 59% yield after purification by column chromatography.

The three-step synthesis of the MPTTF-phenyl-PTM radical **2** is summarized in Scheme 3. Compound **10** was obtained in 69% yield through a Horner-Wadsworth-Emmons reaction of compound **8** and the protonated PTM derivative **9** functionalized with a phosphonate group, whose synthesis has been reported elsewhere.[41] A subsequent deprotonation of **10** with tetrabutylammonium hydroxide (TBAOH) followed by oxidation of the formed carbanion with silver nitrate ($AgNO_3$) afforded the radical dyad **2** (71%) as a black solid, which is stable under atmospheric conditions (Scheme 3).
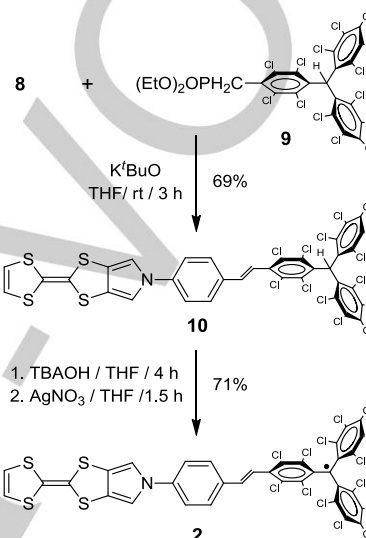
Scheme 3. Synthesis of the MPTTF-Phenyl-PTM radical **2**.

Electrochemical properties: The electrochemical properties were studied by means of CV. Cyclic voltammograms (CVs) of compounds **1**, **2** (Figure 1), and **10** (Figure S2) were recorded in CH_2Cl_2 at room temperature. Compound **10** exhibit two quasi reversible redox waves which can be assigned to the stepwise oxidation of the MPTTF moiety to MPTTF[+]· and MPTTF[2+] with redox potentials of +0.49 and +0.99 V (vs. Ag/AgCl), respectively. As expected, the CV of radical **2** exhibits three waves, related to the following redox pairs: PTM[−]/PTM·, MPTTF/MPTTF[+]·, and MPTTF[+]·/MPTTF[2+], at redox potentials of −0.19, +0.45, and +0.95 V (vs. Ag/AgCl), respectively (Scheme S7). Oxidation potentials of the MPTTF subunits of compounds **2** and **10** show positive shifts compared to the unsubstituted MPTTF **6** (+0.37 and +0.72 V)[35] obtained under the same conditions, consistent with the presence of electron withdrawing chlorinated aromatic fragments in compounds **2** and **10**. In addition, the oxidation potentials shift toward more positive values for **1** when compared to **2**, an observation which most likely can be accounted for by the lower interaction taking place between the D and A subunits in **2** because of the increased length of the bridge connecting the D and A subunits.
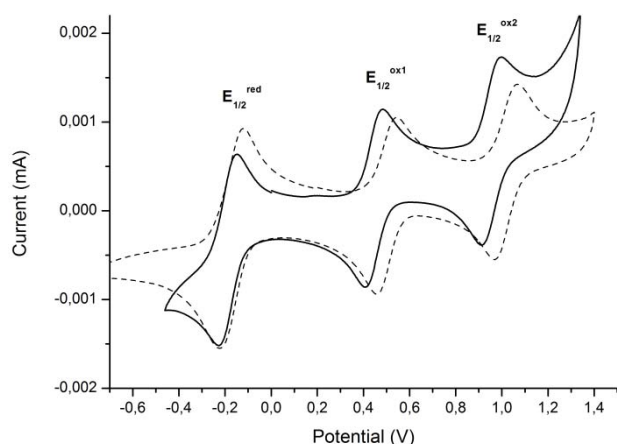
Figure 1. Cyclic voltammograms (CVs) of compounds **1** (dashed line) and **2** (solid line) (0.05 mM) in CH_2Cl_2 vs. Ag/AgCl using n-Bu_4PF_6 (0.1 M) as electrolyte at 300 K under argon at a scan rate of 0.1 V s^{-1}.

Optical properties: The UV-Vis-NIR spectrum (Figure 2) of dyad **2** recorded in THF at 300 K shows an intense absorption band at 385 nm, characteristic of PTM radical chromophores, with a shoulder at 376 nm which can be attributed to the MPTT fragment. The two unresolved peaks appearing at lower energies at 439 and 550 nm, respectively, can be assigned to the electronic conjugation of the unpaired electron into the π-framework. Interestingly, the radical dyad **2** also shows a weak and broad absorption band around 800 nm which can be ascribed to the IET taking place between the TTF donor and the PTM acceptor, whereas a similar IET band is observed in the region between 900-1000 nm for the shorter radical dyad **1**.[42] The hypsocromic shift observed in **2**, as compared to **1**, can be ascribed to the lower donor character of the MPTTF subunit.

When dyad **2** was oxidized with one equivalent of $Fe(ClO_4)_3$, the IET absorption band disappears and a new band appears around 600 nm, which most likely can be assigned to the formation of the radical-cation of the MPTTF subunit. (Figure S3).

In order to compare the bistability in solution of dyads **1** and **2**, the UV-Vis-NIR spectra of **2** were recorded in different solvents (see Figure S4).[31] Its was realized that the bistability of dyad **2** was only observed in the highest polar solvent assayed, e.g., DMF, as demonstrated by the appearance of a band at 512 nm with a small intensity attributed to the presence of a small percentage of dyad **2** in the zwitterionic state, coexisting with the neutral state in the polar DMF medium. This observation is in deep contrast with the behavior of dyad **1**. In DMF, **1** exists only in the zwitterionic state and even in medium polarity solvents, such as acetone and CH_2Cl_2/acetone mixtures **1** was found to exist in the zwitterionic state. This remarkable difference can in part be ascribed to the poorer electron donor character of the MPTTF unit in comparison with the TTF unit. We observe, however, that the formation of zwitterionic species of **1** dissolved in medium and high polarity solvents is actually triggered by the formation of $(TTF^+)_2$ and mixed-valence dimers. Possibly, attaching the pyrrole ring to the TTF moiety reduces the well-known tendency of TTF to form dimers, thus hindering the formation of zwitterionic species.
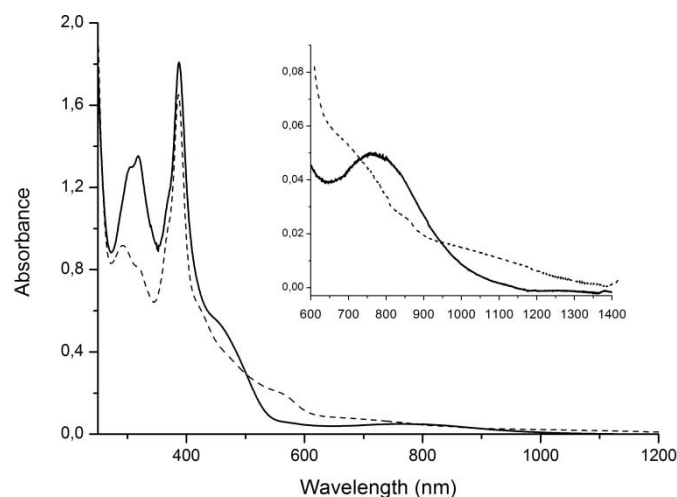

Figure 2. UV-Vis-NIR spectra recorded in THF at 300 K of a 0.05 mM solution of dyads **1** (dashed line) and **2** (solid line). The inset shows the low-energy range of the absorption spectra of **1** and **2**.

Magnetic properties: The ESR spectrum (Figure 3) of **2** recorded in CH_2Cl_2 (0.05 mM) at 300 K shows, centered at a g-value of 2.0029, two partially overlapped main lines corresponding to the coupling of the unpaired electron with one ^1H atom of the vinylene spacer along with a few weak satellite lines because of the coupling with naturally abundant ^{13}C isotopes at the α- and aromatic positions. The isotropic hyperfine coupling constants with such nuclei show the usual values for vinylene substituted PTM radicals; i.e., $a_1(H)=1.99$ G, $a_{13}(C_\alpha)=30.0$ G, $a_{13}(C_{o,p})=12.5$ G.
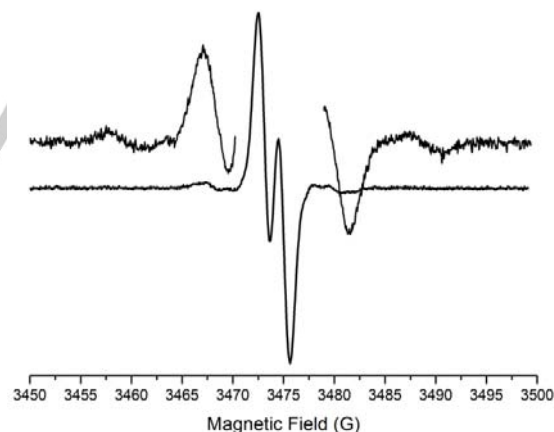

Figure 3. ESR spectrum of a 0.05 mM solution of dyad **2** recorded in CH_2Cl_2 at 300 K.

The ESR spectrum of **2** recorded in the crystalline state at 120 K consists on an asymmetric line indicative of an axial symmetry with $g_a = 2.0045$ and $g_b = g_c = 2.0027$ (Figure S5). Moreover, the ESR lineshape of **2** does not exhibit any significant change in the temperature range of 120-320 K, with its intensity following the Curie law; as for dyad **1** (Figures S6-S7). These results suggest there is no bistability in the solid state associated with an IET for either radical dyad **1** or **2**. Indeed, in the presence of bistability one would expect large changes in the position and shape of the EPR line, due to the large differences of the magnetic anisotropies of PTM radicals and TTF/MPTTF cation-radicals.

Crystal structure of compound 10: X-ray diffraction analysis at 300 K on red crystals of **10**, obtained by slow evaporation from a solution of Et$_2$O/CH$_2$Cl$_2$, indicates it crystallizes in the triclinic system with a P-1 space group (Figure S8 and Tables S1 and S2). The molecular structure of **10** (Figure 5) shows that the vinylene bridge is coplanar with the phenyl ring and it has a *trans*-configuration. The asymmetric unit is formed by two non-equivalent molecules (**10A** and **10B**) in a *head-to-tail* arrangement (Figure 4b). The phenyl and pyrrole rings are not coplanar, showing torsion angles C14-C9-N1-C4 of *ca.* 26 and 23° for **10A** and **10B**, respectively. Moreover, the MPTTF unit is somewhat distorted in the typical boat conformation with a torsion angle S3-C6-S4-C8 of *ca.* 14° and the average of MPTTF C=C bond lengths is 1.34 Å for **10A** and 1.43 Å for **10B**. The MPTTF moieties of neighboring molecules are forming alternated *face-to-face* dimers of **10A···10A** or **10B···10B** molecules on the *bc* plane forming 1-D chains along the *c*-axis with shortest S-S distances of 3.92 and 3.98Å, respectively (See Figure 6 and Table S3). On the other hand, the PTM units are also stacked forming monodimensional chains along the c-axis with short intermolecular Cl···Cl interactions that are in the range of 3.28-3.47 Å (Figure S10).
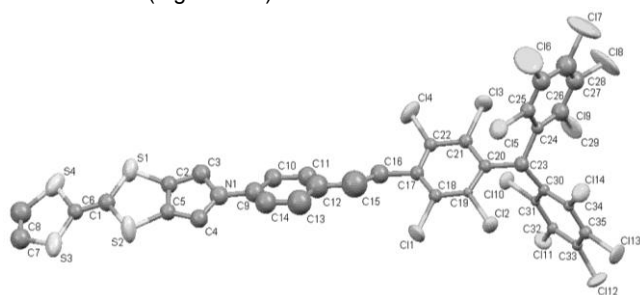
configuration and with the phenyl and pyrrole rings twisted with a torsion angle C14-C9-N1-C4 of *ca.* 31°. The MPTTF subunits are also distorted with a torsion angle S3-C6-S4-C8 of *ca.* 10° and with central C=C bond lengths of 1.36 Å, demonstrating that the TTF is still in the neutral state[43] (but with certain degree of charge delocalization over the conjugated skeleton). The main differences between the non-radical compound **10** and the radical dyad **2** are located on the vinylene bridge and the PTM region. In fact, the vinylene-bridge region of **2** exhibits a higher degree of electron delocalization than **10** as estimated by calculating the differences between the single C-C bonds and C=C double bonds lengths. These difference values pass from 0.33-0.35 Å for **10A** and **10B** to 0.17 Å for **2A** and **2B** at 300 K demonstrating that the PTM radical unit in dyad **2** induces a higher electron-withdrawing effect over the rest of the molecule in contrast with what is observed in compound **10**. On the other hand, the average of the distance between the central C23 atom of PTM and C20, C24 and C30 atoms is *ca.* 1.54 Å in **10** and 1.46 Å in **2**, showing a partial double-bond character in **2** that indicates a weak delocalization of the unpaired electron into the aromatic rings, as reported for other PTM derivatives.[44]

Figure 5. ORTEP views of compound **10** at 300 K. Hydrogen atoms have been omitted for clarity.
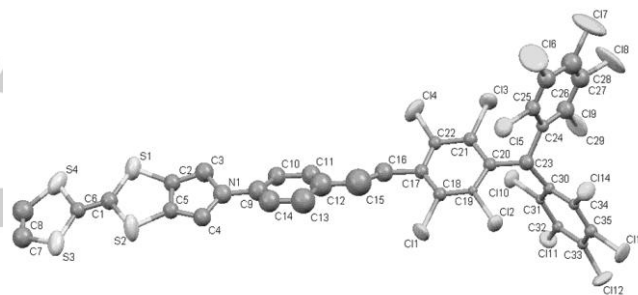
Figure 6. ORTEP views of radical dyad **2** at 300 K. Hydrogen atoms have been omitted for clarity.

Molecules of radical dyad **2** are arranged as shown in Figure 6 forming regular 1-D chains of equivalent molecules (**2A** or **2B**) where the MPTTF subunits form a *herringbone* structure along the *b*-axis with short Cl···Cl contacts in the range of 3.30-3.49 Å and S···S short contacts of 3.95 Å and 3.90 Å for **2A** and **2B**, respectively (See Table S3). However, this supramolecular assembly is different over the *a*-axis, where there is no overlap between the S atoms and the stacking is governed by S···Cl and S···C(pyrrole) interactions of 3.52 Å and 3.45 Å, respectively, alternating molecules of **2A** and **2B** (Figures 7 and S14).

Figure 6. Molecular packing of compound **10** at 300 K in the *bc* plane.

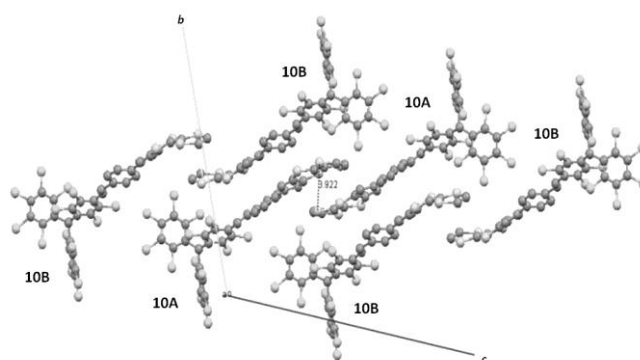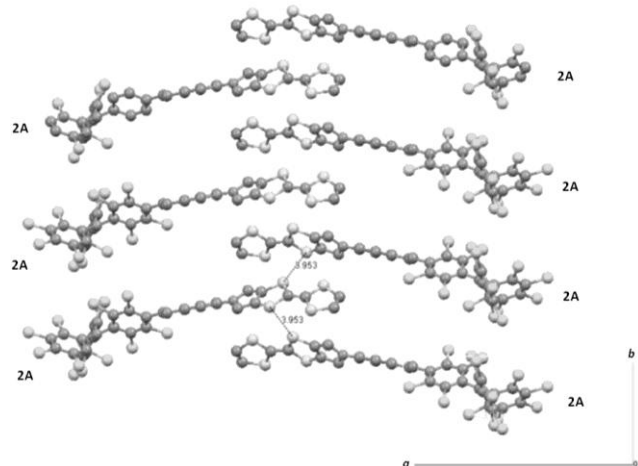**Figure 7.** Molecular packing of **2A** molecules at 300 K in the *ab* plane.

Crystal structure of compound 2: X-ray diffraction analysis at 150 and 300 K on small black crystals of radical dyad **2**, obtained by a slow evaporation from a *n*-hexane/CH$_2$Cl$_2$ solution, indicates it crystallizes in the monoclinic system with the space group P21 (Figure 7 and Tables S1 and S2). The asymmetric unit reveals two non-equivalent molecules (**2A** and **2B**) that are aligned in parallel along the *a*-axis as shown in Figure S12. The molecular structure of **2** is alike to that of **10** since it shows that the vinylene bridge is coplanar with the phenyl ring with a *trans*-
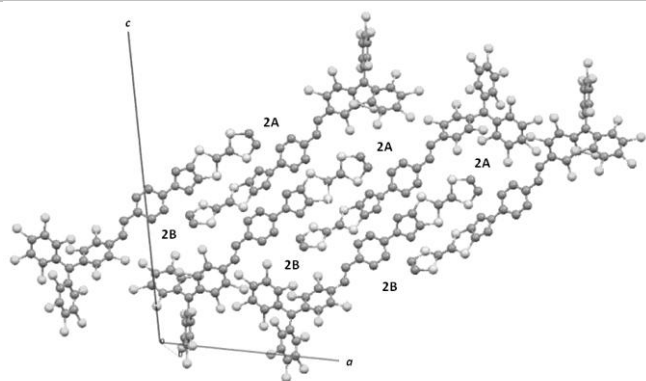
Figure 8. Molecular packing of radical dyad **2** at 300 K in the *ac* plane.

In order to study possible changes in the molecular structure at low temperatures, the X-ray crystal structure of radical dyad **2** was obtained at 150 K (See Tables S1 and S2). Interestingly, the degree of delocalization of the two non-equivalent molecules (**2A** and **2B**) of dyad **2**, that is very similar at room temperature, changes drastically for both molecules in opposite directions at 150 K since molecules **2B** become much more delocalized along their entire skeletons than molecules **2A** at 150 K. Indeed, molecule **2B** at 150 K exhibits a higher degree of delocalization as demonstrated by the shortness of the N1-C9 (1.39 Å for **2B** and 1.45 for **2A**), the difference between the single C-C bonds and C=C double bonds in the vinylene-bridge region which are 0.21 for **2A** and 0.09 for **2B**, as well as the difference C-S – C=C in the MPTTF region which are 0.45 for **2A** and 0.37 for **2B**. This interesting observation could be because of the different surrounding polar environment that involves the two different molecules (**2A** and **2B**) that possibly modifies the electrostatic interactions between molecules by the surrounding media. It is important to be note that molecule **2A** has three nearby Cl atoms surrounding the MPTTF unit, whereas molecule **2B** has only two Cl atoms near to the MPTTF unit as shown in Figure S13. On the other hand, decreasing the temperature to 150 K, the intermolecular S···S short distances between neighboring molecules inside the stacks formed by **2A** or **2B** molecules along the *b*-axis also decrease up to 3.89 and 3.85 Å, respectively (Figure S15).

The structural changes observed at low temperatures suggested that modifications in the electronic structures may occur. To evaluate these modifications, hopping integrals between the MPTTF units in neighboring MPTTF-PTM moieties were calculated on the basis of the ZINDO method.[45] The hopping integrals for the structure at 300 K along the *b*-axis (Figure 7) were found to be 12 meV and 20 meV between molecules **2A**···**2A** and **2B**···**2B**, respectively, and 10 meV for the dimer **2A**···**2B** along the *a*-axis (Figure 8). Interestingly, at a lower temperature (150 K) the hopping integral of **2A**···**2A** increases to 19 meV whereas the integral between **2B**···**2B** decreases down to 1 meV. Therefore, whereas the hopping integral of **2A**···**2A** increases by lowering *T*, as expected in consequence of lattice contraction, that between **2B**···**2B** essentially disappears making the **2B** units practically isolated within the stack.

Polarized IR-NIR-Visible and Raman Spectra in the Solid State: The polarized IR and NIR-visible absorption spectra (Figure 9) recorded of the dyad **2**, shows the low frequency electronic transitions. The spectrum, with electric vector parallel to the crystal *b* axis (red line), is limited to 11000 cm⁻¹ because beyond this frequency the spectrum is completely saturated. A band around 8900 cm⁻¹ (1120 nm) is clearly discernible. The origin of this band is unclear at present stage. It is unlikely that it is associated with intermolecular CT (ICT), since the MPTTF units are essentially neutral (*vide infra*). The spectrum with electric vector perpendicular to the *b* axis (black line), namely, approximately along the direction of ICT transition dipole moment, shows two bands before reaching saturation around 18000 cm⁻¹, one at about 10500 cm⁻¹ (950 nm) and the other at about 15200 cm⁻¹ (660 nm). The latter might be the solid state counterpart of the band observed in solution around 700 nm, and attributed to IET. Both the 10500 cm⁻¹ and the 15200 cm⁻¹ bands, which are very weak, have a polarization compatible with IET.
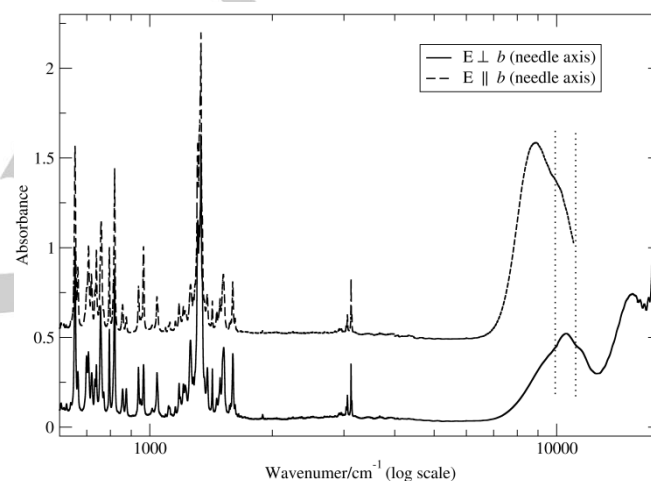

Figure 9. Extended polarized absorption spectra of a crystal of dyad **2** with logarithmic scale for the frequencies. For the sake of clarity, the spectra in the two polarizations are offset by 0.5 Absorbance units. The dotted vertical lines mark the points of beam splitter/detector changes.

The Raman spectrum of dyads **1** and **2** were recorded at 300 K using an excitation wavelength of 1064 nm in the near IR region (Figure S16). The Raman bands close to 1600 cm⁻¹ are attributed to the C=C stretching mode of the vinylene spacer whereas the bands around 1510 cm⁻¹ are characteristic for the stretching mode of the lateral polychlorinated benzene groups.[46] This Raman band shifts toward higher frequencies when there is an increment of effective π-electron delocalization into the PTM subunit. This Raman shift is well observed in the spectrum of the oxidized derivative **1⁺** where there is a downshift from 1515 to 1508 cm⁻¹,[33] due to the suppression of the IET process because of the lack of the donor character of the oxidized TTF subunit. Comparing the spectra of **1** and **2**, it can be stated that there is a higher electron (and spin) delocalization in compound **1** as demonstrated by its higher Raman shift. Moreover, it is well known that vibrational spectroscopy can provide a reliable estimate of the formal charge or degree of CT on the molecular sites.[47] In the case of TTF, the charge sensitive vibrations are associated with the C=C stretching, notably the Raman active ν_3 mode, which appears at 1516 in neutral TTF and at 1420 cm⁻¹ in the radical-cations, and the infrared active ν_{14} mode, respectively found at 1530 and 1478 cm⁻¹.[48-50] The Raman and

the IR polarized spectra of **2** (Figure S17) lead us to conclude that the MPTTF C=C stretching overlaps around 1518 cm^{-1} with the above mentioned C=C stretching mode associated with PTM. In this complex situation, it is difficult to obtain a precise estimate of the ionicity, but in any case it can be concluded that in the solid state the TTF/MPTTF subunits of both **1** and **2** dyads are in a practically neutral state.

In order to evaluate if any temperature effect on the CT from the MPTTF to the PTM in the crystals of dyad **2** is present, as was observed with the increase of delocalization in the **2B** unit, the Raman spectra of **2** was also recorded at 120 K, in this case, with 752 nm excitation. (Figure S17). In the relevant spectral region we do not observe any downshift on the Raman bands, indicating that there is no CT from the TTF or if present, it is so small that it cannot be detected by means of Raman spectroscopy.

Theoretical calculations: To deepen the understanding the electronic structures of TTF/MPTTF-PTM dyads, a series of quantum chemical calculations have been performed on dyads **1** and **2** in solution, using Gaussian 09 package.[51] Geometries were optimized at (U)CAM-B3LYP/6-31G* level for different oxidation states of **1** and **2** (see Figure S19), the neutral open-shell doublet states (neutral species), the closed-shell anions (anionic species), the cation-biradical (cationic species), where the bi-radicaloid character was enforced by considering the triplet state, and the dication-radical (dicationic species). In all cases, solvent was introduced based on the polarizable continuum model (PCM).[52]

The charge distribution for the neutral radical dyads **1** and **2** (Figure S18) supports a very small degree of CT in the molecule, in line with spectroscopic results. As described in the SI, we divided the molecule in D and A fragments. The charge on each fragment is of the order of 0.09 (for D) and 0.10 (for D) for **1** and **2** in CH$_2$Cl$_2$, respectively, and only marginal variations with solvent polarity were obtained. Charge distributions in the cationic, dicationic and anionic species (Figure S18) confirms the CV data, with an excess of electron residing on PTM fragment in the anionic species, and positive charges residing in the TTF/MPTTF fragments in the mono and dicationic species.

The spin distribution in Figure 10 shows that the spin is localized on the PTM moiety and on the vinylene group for the neutral **1** and **2** species, in line with the results obtained using EPR spectroscopy. In the cationic diradicaloid species, the two spin densities on the TTF/MPTTF and PTM units are fully disconnected. As for the ground state charge and spin distributions, the different bridges play a marginal role in affecting the molecular properties.
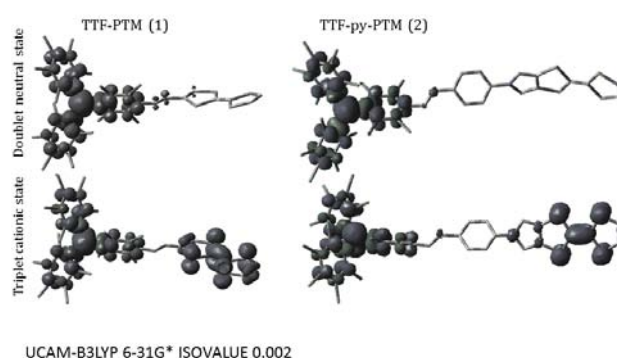

UCAM-B3LYP 6-31G* ISOVALUE 0.002

Figure 10. Spin density (light blue) of dyads **1** and **2** in CH$_2$Cl$_2$, calculated at UCAMB3LYP/6-31G* level with PCM. Top and bottom panel show results for the neutral and cationic species, respectively. Isovalue of the plot equal to 0.002.

Table 1. Lowest and most intense optical transitions calculated for dyads **1** and **2** in CH$_2$Cl$_2$ at TD-UCAM-B3LYP/6-31G* level.

	λ(nm)	oscillator strength	transition nature
1	365	0.10	HOMO-4(β) →SUMO (0.40)
			HOMO-α →LUMO-α (0.21)
	368	0.50	HOMO-4(β) →SUMO (0.18)
			HOMO-β →LUMO-β (0.15)
	375	0.02	HOMO-3(β) → SUMO(0.61)
	474	0.16	HOMO-β →SUMO (0.69)
			HOMO-β →SUMO (0.13)
	636	0.01	HOMO-β → LUMO-β (0.13)
			(HOMO-1)-β → SUMO (0.12)
			(HOMO-1)-β → LUMO-β (0.12)
2	364	0.47	HOMO-5(β) →SUMO (0.11)
			(HOMO-1)α→LUMO-α (0.10)
			(HOMO-3)β→ SUMO (0.11)
			(HOMO-1)β → SUMO (0.21)
	366	0.01	HOMO-6(β) →SUMO (0.81)
	372	0.03	HOMO-5(β) →SUMO (0.71)
	416	0.08	HOMO-β →SUMO (0.76)
	438	0.06	(HOMO-9)-β →SUMO (0.23)
	516	0.013	(HOMO-1)-β → LUMO-β (0.14)
			(HOMO-1)-β → SUMO (0.10)
			(HOMO-3)-β → SUMO (0.07)
			(HOMO-3)-β → LUMO-β (0.07)
			(HOMO-1)-α → LUMO-α (0.15)

In Table 1, the calculated results for the lowest energy transitions with oscillator strengths larger than the lowest energy transition (0.01) obtained for **1** and **2** at the TD-UCAMB3LYP/6-31G* at optimized ground state geometries are summarized. Results refer to CH$_2$Cl$_2$ solutions, but solvent effects are marginal (see SI). Relevant MOs are shown in Figure 11 and a more complete set of frontier MOs can be found in Figure S19.

Both radical dyads show in the 364-375 nm region three transitions mainly localized on the PTM unit with minor contributions from bridge states. These transitions are readily assigned to the strong and structured peak observed at ~385 nm. Several transitions are observed at lower energy for both compounds all showing some IET character, even if a large mixing is observed with excitations involving bridge-state, as expected on physical basis.[53] These transitions are assigned to the many broad features observed in experimental spectra in the low-frequency region. Indeed the relevant energy is overestimated by ~0.6 eV, large errors are expected due to the problems of TD-DFT with CT states and in radical species.[54-56] For comparison, analogous results at the B3LYP level (see SI) underestimate the transitions by a similar amount. The oscillator strength associated with this lowest energy transition is a small fraction (1/50-1/100) of the oscillator strength associated with the intense peak localized on PTM, in line with the experimental data.
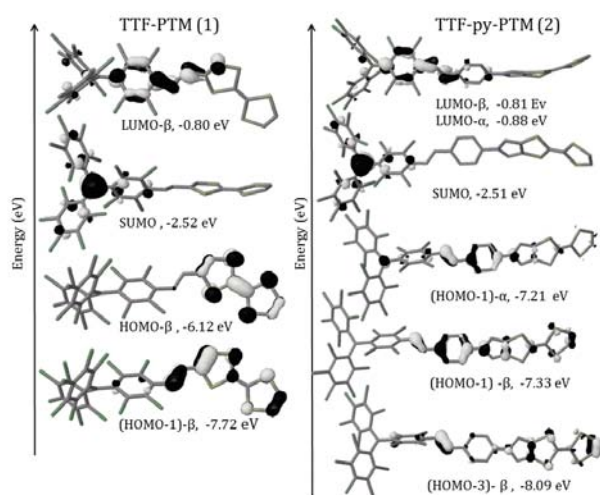

Figure 11. MOs involved in lowest energy transitions (see Table 1).

Calculations on the isolated dyad **2** at the crystallographic geometry support a largely neutral ground state both at room and at low temperature (Table S6), in agreement with experimental data. Quite interestingly the charge separation slightly decreases on molecule A upon decreasing temperature, while for molecule B a larger increase of ionicity is observed, in line with an improved delocalization.

Conclusions

In summary, we have reported the synthesis and characterization of the new donor-acceptor dyad **2**, a TTF-pyrrolo-annulated-PTM radical, with an extended structure that allowed single crystals of good quality to be obtained. Analysis of the Raman spectra and X-ray bond lengths of the radical dyad **2** and its non-radical counterpart **10** indicates that there is some π-conjugation between the MPTTF donor and the PTM radical acceptor although the dyad is maintained in the neutral state at room temperature. The X-ray structure of **2** revealed a segregation of the donor and acceptor subunits with a regular stacking of the MPTTF along one direction where such units tend to form a *herringbone* arrangement with short (3.85 Å at 150 K) interactions between the S atoms. Interestingly, when decreasing the temperature one of the two non-equivalent molecules (**2B**) becomes much more delocalized, as demonstrated by X-ray bond lengths, whereas the other non-equivalent molecule remains less delocalized (**2A**). In accordance with the original design strategy, the extension of the distance between the MPTTF and PTM moieties has enabled to growth crystals of MPTTF-PTM radical dyad, with a packing in which the donor and the acceptor subunits are segregated and the neighboring MPTTFs show a (modest) degree of interaction. This donor-acceptor radical dyad is the first example of promising molecular building-blocks for the development of novel spintronic molecular materials in view of its solid-state structure and electronic properties.

Experimental Section

General methods: ^{1}H NMR spectra were recorded using a Bruker Avance 250, 400, or 500 instruments and Me$_4$Si as an internal standard. Infrared spectra were recorded with Spectrum One FT-IR Spectroscopy instrument and UV/Vis/NIR spectra were measured using Cary 5000E Varian. ESR spectra were performed with a Bruker ESP 300 E equipped with a rectangular cavity T102 that works with an X-band (9.5 GHz). The solutions were degassed by argon bubbling before the measurements. LDI/TOF MS were recorded in a Bruker Ultraflex LDI-TOF spectrometer. Cyclic voltammetry measurements were obtained with a potentiostat 263a from EG&G Princeton Applied Research in a standard 3 electrodes cell. The Raman spectra of **1**, **1**[+·], and **2** are FT–Raman spectra obtained in a Bruker Equinox 55 FT–IR interferometer using a Raman accessory kit (FRA/106–S). A continuous–wave Nd–YAG laser working at 1064 nm was employed for excitation. A germanium detector operating at liquid nitrogen temperature was used. Raman scattering radiation was collected in a back–scattering configuration with a standard spectral resolution of 4 cm^{-1}. 1000-3000 scans were averaged for each spectrum. The Raman spectra of **2** at 120 K have been collected with the Renishaw 1000 microspectro-meter, with 752 nm excitation. The laser power has been kept to the minimum (less than 1 mW at the sample) to avoid sample degradation. The IR-NIR spectra have been collected with a Bruker FT-IR IFS-66 spectrometer equipped with a Hyperion microscope. The spectral resolution is about 2 cm^{-1} for both spectrometers. For the low-temperature spectra, it has been used a Linkam stage. All reagents and solvents employed for the syntheses were of high purity grade and were purchased from Sigma-Aldrich Co., Merck, and SDS. Dry solvents were used in the chemical reactions and in the cyclic voltammetries. The solvents used for optical spectroscopy and ESR measurements were of HPLC grade (ROMIL-SpS). In addition, for cyclic voltammetry experiments, CH$_2$Cl$_2$ was filtered over basic alumina to eliminate the acidic residues.

Compound 5: A degassed solution of 1,3-dithiol-2-thione (**3**)[S2] (0.49 g, 3.65 mmol) and 5-tosyl-(1,3)-dithiolo[4,5-*c*]pyrrol-2-one (0.75 g, 2.43 mmol) (**4**) dissolved in freshly distilled P(OEt)$_3$ (30 mL) was heated at 130 °C. After 10 min another portion of **4** (0.49 g, 3.65 mmol, 7.35 eq in total) was added. The reaction mixture was heated for 3 h before being cooled to room temperature. Addition of cold MeOH (50 mL) produced a yellow precipitate, which was filtered and washed with MeOH (3 × 15 mL). The resulting solid was dried and then dissolved in a small portion of CH$_2$Cl$_2$ and subjected to purification by flash chromatography (SiO$_2$, CH$_2$Cl$_2$: Petroleum Ether, 1:2, v/v, gradient elution). The yellow band (R_f = 0.6, CH$_2$Cl$_2$: Petroleum Ether, 1:1) was collected and the solvent evaporated affording **5** (0.68 g, 71%) as a yellow solid (mp = 250 °C). ^{1}H NMR (400 MHz, CD$_3$SOCD$_3$) δ (ppm) = 2.38 (s, 3H, Ts-CH$_3$), 6.74 (s, 2H, HC=CH), 7.36 (s, 2H, α-H pyrrole), 7.46 (d, 2H, J = 8.2 Hz, Ar-H), 7.83 (d, 2H, J = 8.2 Hz, Ar-H). ^{13}C NMR (100 MHz, CD$_3$SOCD$_3$) δ (ppm) = 21.1 (Ts-CH$_3$), 112.4 (pyrrole α-C), 112.7 (fulvalene C=C), 118.7 (fulvalene C=C), 119.6 (HC=CH), 126.7 (dithiol =C-C=), 126.9 (Ar-C-2), 130.4 (Ar-C-3), 134.5 (Ar-C-1), 145.8 (Ar-C-4). MS (EI): m/z (%) = 394.96 [M[+], 100].

IR (KBr) ν (cm^{-1}) = 3137, 1635, 1596, 1370 (SO$_2$), 1225, 1172 (SO$_2$), 1090, 1055, 680. CV (n-Bu$_4$NPF$_6$ 0.1 M in CH$_3$CN at 298 K vs Ag/AgCl): $E_{1/2}{}^1$ = +0.27 V; $E_{1/2}{}^2$ = +0.49 V. Elemental Analysis: Anal. Calcd. for C$_{15}$H$_{11}$NO$_2$S$_5$: C: 45.31; H: 2.79; N: 3.52. Found: C: 44.82; H: 2.86; N: 3.40.

Compound 6: Compound **5** (0.46 g, 1.15 mmol) was dissolved in a mixture of anhydrous THF - MeOH (1:1, v/v, 24 mL). The solution was degassed for 20 min under Argon atmosphere, whereupon a solution of NaOMe in MeOH (25%, ca 1.4 mL, 1.0 g, 25 mmol) was added in one portion. The mixture was refluxed at 78 °C for 15 min, then cooled to room temperature and concentrated to half volume. Water (50 mL) was added, producing a yellow precipitate, where after the suspension was extracted with CH$_2$Cl$_2$ (2 × 20 mL). The combined organic phases were washed with H$_2$O (2 × 20 mL) and brine (2 × 20 mL) and subsequently dried (MgSO$_4$). After evaporation of the solvent, the green crude product was purified by flash chromatography (SiO$_2$ deact, CH$_2$Cl$_2$). The yellow band (R_f = 0.6, CH$_2$Cl$_2$) was collected and the solvent evaporated to afford **6** (0.25 g, 90%) as a yellow powder (mp = 190-191 °C). ^{1}H NMR (500 MHz, CDCl$_3$) δ (ppm) = 6.72 (s, 2H, HC=CH), 6.78 (d, 2H, J = 2.71 Hz, pyrrole α-H), 11.08 (s, 1H, NH). ^{13}CNMR (125 MHz, CDCl$_3$) δ (ppm) = 109.7 (pyrrole α-C), 115.3 (fulvalene C=C), 116.2 (fulvalene C=C), 118.7 (dithiol =C-C=), 120.6 (HC=CH). MS (EI): m/z (%) = 243 [M$^+$, 100]. IR (KBr) ν (cm^{-1}) = 3410 (NH stretch), 3124, 1629 (NH), 1531, 1252 (C-N). CV (n-Bu$_4$NPF$_6$ 0.1 M in CH$_3$CN at 298 K vs Ag/AgCl): $E_{1/2}{}^1$ = +0.37 V; $E_{1/2}{}^2$ = +0.72 V. Elemental Analysis: Anal. Calcd. for C$_6$H$_5$NS$_4$: C: 39.48; H: 2.07; N: 5.75. Found: C: 40.18; H: 2.11; N: 5.44.

Compound 8: A Schlenk tube containing a mixture of compound **6** (71 mg, 0.291 mmol), 4-iodobenzaldehyde (**7**) (171 mg, 7.37 mmol), K$_3$PO$_4$ (230 mg, 10.8 mmol), and CuI (113 mg, 5.93 mmol) dissolved in freshly distilled THF (5 mL) was degassed under argon for 15 min, where after ±-trans-1,2-diaminocyclohexane (0.1 mL, 0.83 mmol) was added to the solution and the vial capped. The reaction mixture was heated for 3 h at 105 °C, cooled to room temperature and the solution was extracted with CH$_2$Cl$_2$ and washed with water (4 × 20 mL). The combined organic phases were combined, dried (MgSO$_4$) and concentrated to give an orange solid that was purified using flash chromatography (SiO$_2$, CH$_2$Cl$_2$:Toluene, 1:1, v/v). The yellow band (R_f = 0.3, CH$_2$Cl$_2$:Toluene, 1:1) was collected and concentrated to provide the desired compound **8** as a red solid (59.7 mg, 59 %). Shiny crystals of **8** were obtained from CH$_2$Cl$_2$:Et$_2$O (1:1). ^{1}H NMR (500 MHz, CD$_3$SOCD$_3$) δ (ppm) = 9.98 (s, 1 H, -CHO), 7.94 (d, 2H, J = 8.2 Hz, Ar-H), 7.45 (d, 2H, J = 8.2 Hz, Ar-H), 6.99 (s, 2H, pyrrole α-H), 6.34 (s, 2 H, HC=CH). ^{13}C NMR (125 MHz, CD$_3$SOCD$_3$) δ (ppm) = 190.8, 136.2, 131.7, 126.6, 119.7, 119.0, 118.6, 110.1.(2 lines are missing/overlapping). MALDI-MS (DCTB): m/z (%) = 347.6 [M$^+$, 100]. CV (n-Bu$_4$NPF$_6$ 0.1 M in CH$_3$CN at 298 K): $E_{1/2}{}^1$ = +0.28 V; $E_{1/2}{}^2$ = +0.64 V. Elemental Analysis: Anal. Calcd. for C$_{15}$H$_9$NOS$_4$: C: 51.85; H: 2.61; N: 4.03. Found: C: 51.33; H: 2.49; N: 3.65.

Compound 10: The phosphonated PTM derivative **9**^{S1} (344 mg, 0.39 mmol) was dissolved in anhydrous THF (60 mL) under strict inert conditions, whereupon the solution was cooled down to -78 °C. Potassium *tert*-butoxide (98 mg, 0.87 mmol) was added and the reaction mixture was stirred for 20 minutes to form the yellow-orange ylide. Susequently, the MPTTF compound **8** (150 mg, 0.43 mmol) was added and the reaction mixture was allowed to warm up to room temperature. After being stirred for 3 d at room temperature, the reaction mixture was extracted with CH$_2$Cl$_2$, washed with H$_2$O, and dried (MgSO$_4$). The solvents were evaporated and the crude product was purified by column chromatography (SiO$_2$, Et$_2$O:hexanes, 1:1, v/v) to provide the desired compound **10** as a light orange powder (290 mg, 69%). ^{1}H NMR (400 MHz, CD$_3$SOCD$_3$) δ (ppm) = 7.75 (d, 2H, J = 8.2 Hz, Ar-H), 7,59 (d, 2H, J = 8.2 Hz, Ar-H), 7.53 (s, 2H, pyrrole α-H), 7.22 (d, 1H, J = 16.8 Hz, Phenyl-CH=CH-PTM), 7.13 (d, 1H, J = 16.8 Hz, Phenyl-CH=CH-PTM), 6.95 (s, 1H, □H), 6.76 (s, 2H, HC=CH). FT-IR ν (cm^{-1}) = 2955 (w), 2922 (w), 2855 (w), 1728 (w), 1602 (m, CH=CH), 1517 (s), 1487 (m), 1461 (w), 1381 (m), 1370 (m), 1335 (m), 1309 (s), 1185 (m), 1138 (m), 1038 (m), 967 (m), 936 (m), 869 (w), 806 (s), 750 (m), 691 (m). UV-VIS-

NIR (CH$_2$Cl$_2$, λ_{max} (nm), ε in (M^{-1}·cm^{-1})) = 327 (15958); 377 (14848). LDI-TOF (positive mode): m/z (amu/e$^-$): 1069.721 CV (n-Bu$_4$NPF$_6$ 0.1 M in CH$_2$Cl$_2$ as electrolyte vs Ag/AgCl): $E_{1/2}{}^1$ = +0.49 V; $E_{1/2}{}^2$ = + 0.99 V.

Compound 2: Compound **10** (90 mg, 0.08 mmol) was dissolved in distilled CH$_2$Cl$_2$ (40 mL) and a solution of n-Bu$_4$NOH (1.0 M in MeOH, 120 μL, 0.12 mmol) was added. The purple reaction mixture was stirred for 4 h before AgNO$_3$ (24 mg, 0.14 mmol) dissolved in acetonitrile (10 mL) was added. The reaction mixture was then stirred for further 90 min and the solution changes color from purple to dark brown and a precipitate of silver (Ag^0) was formed. Subsequently, the reaction mixture solution was filtered and the filtrate concentrated. Finally, the crude product was purified by flash column chromatography (SiO$_2$, CH$_2$Cl$_2$:hexanes, 1:1, v/v) to produce the desired TTF-Pyrrole-Phenyl-PTM radical **2** as a dark reddish-brown powder (64 mg, 71%). FT-IR ν (cm^{-1}) = 2952 (m), 2922 (s), 2855 (m), 1727 (w), 1660 (w), 1626 (w), 1605 (m, CH=CH), 1519 (s), 1456 (w), 1427 (w), 1382 (m), 1335 (s), 1311 (s), 1257 (m), 1183 (m), 1155 (w), 1038 (m), 966 (m), 936 (m), 875 (w), 815 (s), 795 (m), 753 (m), 734 (m). UV-VIS-NIR (CH$_2$Cl$_2$, λ_{max} (nm), ε (M^{-1}·cm^{-1})) = 199 (13176), 321 (12730), 375 (13207), 386 (16220), 439 (4950). LDI-TOF (positive mode): m/z (amu/e$^-$): 1069.643 [M]$^{+\cdot}$, 997.698 [M – 70]$^+$, (negative mode): 1069.653 [M]$^{-\cdot}$. CV (n-Bu$_4$NPF$_6$ 0.1 M in CH$_2$Cl$_2$ as electrolyte vs Ag/AgCl): $E_{1/2}{}^1$ = –0.19 V, $E_{1/2}{}^2$ = +0.45 V, $E_{1/2}{}^3$ = +0.95. ESR (CH$_2$Cl$_2$) g = 2.0025.

Acknowledgements

Keywords: Donor-acceptor • tetrathiafulvalene • polycholotriohenylmethyl radical • intramolecular charge transfer • self-assembled architecture

[1] F. M. Raymo, *Adv. Mater.* **2002**, *14*, 401-414.
[2] P. Gutlich, A. Hauser, H. Spiering, *Angew. Chem. Int. Ed.* **1994**, *33*, 2024-2054.
[3] O. Sato, J. Tao, Y. Z. Zhang, *Angew. Chem. Int. Ed.* **2007**, *46*, 2152-2187.
[4] I. Ratera, D. Ruiz-Molina, J. Vidal-Gancedo,K. Wurst, N. Daro, J-D. Letard, C. Rovira, J. Veciana, *Angew. Chem. Int. Ed.* **2001**, *40*, 919-922.
[5] I. Ratera, J. Veciana, *Chem. Soc. Rev.* **2012**, *41*, 303.
[6] J. M. Tour, M. Kozaki, J. M. Seminario, *J. Am. Chem. Soc.* **1998**, *120*, 8486.
[7] J.-M. Lehn, *Science* **2002**, *295*, 2400.
[8] Y. Yamamoto, T. Fukushima, Y. Suna, N. Ishii, A. Saeki, S. Seki, S. Tagawa, M. Taniguchi, T. Kawai, T. Aida, *Science* **2006**, *314*, 1761-1764.

[9] E. H. Beckers, S. C. Meskers, A. P. Schenning, Z. Chen, F. Würthner, P. Marsal, D. Beljonne, J. Cornil, R.A. Janssen, *J. Am. Chem. Soc.* **2006**, *128*, 649-657.

[10] N. Kondo, M. Uchikawa, S. Kume, H. Nishihara, *Chem. Commun.* **2009**, 1993-1995.

[11] A. Scott, A. B. Ricks, M. T. Colvin, M. R. Wasielewski, *Angew. Chem. Int. Ed.* **2010**, *49*, 2904-2908.

[12] O. Elsner, D. Ruiz-Molina, J. Vidal-Gancedo, C. Rovira, J. Veciana, *Chem. Commun.* **1999**, 579-580.

[13] O. Elsner, D. Ruiz-Molina, I. Ratera, J. Vidal-Gancedo, C. Rovira, J. Veciana, *J. Organomet. Chem.* **2001**, *251*, 637–639.

[14] I..Ratera, D. Ruiz-Molina, F. Renz, J. Ensling, K. Wurst, C. Rovira, P. Gütlich, J. Veciana, *J. Am. Chem. Soc.* **2003**, *125*, 1462-1463.

[15] C. Sporer, I. Ratera, D. Ruiz-Molina, Y. Zhao, J. Vidal-Gancedo, K. Wurst, P. Jaitner, K. Clays, A. Persoons, C. Rovira, J. Veciana, *Angew. Chem. Int. Ed.* **2004**, *43*, 5266-5268.

[16] I..Ratera, C. Sporer, D. Ruiz-Molina, N. Ventosa, J. Baggerman, A. M. Brouwer, C. Rovira, J. Veciana, *J. Am. Chem. Soc.* **2007**, *129*, 6117-6129.

[17] G. D'Avino, L. Grisanti, J. Guasch, I. Ratera, J. Veciana, A. Painelli, *J. Am. Chem. Soc.* **2008**, *130*, 12064-12072.

[18] J. .Guasch, L. Grisanti, S. Jung, D. Morales, G. D'Avino, M. Souto, X. Fontrodona, A. Painelli, F. Renz, I. Ratera, J. Veciana, *Chem. Mater.* **2013**, *25*, 808–81.

[19] M. Gonz lez, J. L. Segura, C. Seoane, N. Martín, J. Garín, J. Orduna, R. Alcal , . Villaca pa, V. Hern ndez, J. T. L pez Navarrete, *J. Org. Chem.* **2001**, *66*, 8872-8882.

[20] D. F. Perepichka, M. R. Bryce, E. J. McInnes, J. P. Zhao, *Org. Lett.* **2001**, *3*, 1431-1434.

[21] S. Nishida, Y. Morita, K. Fukui, K. Sato, D. Shiomi, T. Takui, K. Nakasuji, *Angew. Chem. Int. Ed.* **2005**, *44*, 7277-7280.

[22] C. Jia, S. Liu, C. Tanner, C. Leiggener, A. Neels, L. Sanguinet, E. Levillain, S. Leutwyler, A. Hauser, S. Decurtins, *Chem. Eur. J.* **2007**, *13*, 3804-3812.

[23] S. Kato, M. Kivala, W. B. Schweizer, C. Boudon, J. P. Gisselbrecht, F. Diederich, *Chem. Eur. J.* **2009**, *15*, 8687-8691.

[24] F. Otón, V. Lloveras, M. Mas-Torrent, J. Vidal-Gancedo, J. Veciana, C. Rovira, C. *Angew. Chem. Int. Ed.* **2011**, *50*, 10902-10906.

[25] F. Otón, R. Pfattner, E. Pavlica, Y. Olivier, G. Bratina, J. Cornil, J. Puigdollers, R. Alcubilla, X. Fontrodona, M. Mas-Torrent, J. Veciana, C. Rovira, *Cryst. Eng. Comm.* **2011**, *13*, 6597-6600.

[26] F. G. Brunetti, J. L. López, C. Atienza, N. Martín, *J. Mater. Chem.* **2012**, *22*, 4188-4205.

[27] F. Riobé, P. Grosshans, H. Sidorenkova, M. Geoffroy, N. Avarvari, *Chem. Eur. J.* **2009**, *15*, 380-387.

[28] F. Pop, A. Amacher, N. Avarvari, J. Ding, L. M. Daku, A. Hauser, M. Koch, J. Hauser, S. Liu, S. Decurtins, *Chem. Eur. J.* **2013**, *19*, 2504.

[29] Y. Geng, C. Fiolka, K. Krämer, J. Hauser, V. Laukhin, S. Decurtins, S. Liu, *New J. Chem.* **2014**, *38*, 2052-2057.

[30] F. Pop, S. Seifert, J. Hankache, J. Ding, A. Hauser, N. Avarvari. *Org. Biomol. Chem.* **2015**, *13*, 1040-1047.

[31] J. Guasch, L. Grisanti, V. Lloveras, J. Vidal-Gancedo, M. Souto, D. C. Morales, M. Vilaseca, A. Sissa, A. Painelli, I. Ratera, C. Rovira, J. Veciana, *Angew. Chem. Int. Ed.* **2012**, *51*, 11024-11028.

[32] J. Guasch, L. Grisanti, M. Souto, V. Lloveras, J. Vidal-Gancedo, I. Ratera, A. Painelli, C. Rovira, J. Veciana, *J. Am. Chem. Soc.* **2013**, *135*, 6958-6967.

[33] M. Souto, J. Guasch, V. Lloveras, P. Mayorga, J. T. L pez Navarrete, J. Casado, I. Ratera, C. Rovira, A. Painelli, J. Veciana, *J. Phys. Chem. Lett.* **2013**, *4*, 2721-2726.

[34] M. Souto, D. C. Morales, J. Guasch, I. Ratera, C. Rovira, A. Painelli, J. Veciana, *J. Phys. Org. Chem.* **2014**, *27*, 465-469.

[35] S. Nygaard, C. N. Hansen, J. O. Jeppesen, *J. Org. Chem.* **2007**, *72*, 1617-1626.

[36] J. O. Jeppesen, K. Takimiya, F. Jensen, J. Becher, *Org. Lett.* **1999**, *1*, 1291-1294.

[37] J. O. Jeppesen, K. Takimiya, F. Jensen, T. Brimert, K. Nielsen, N. Thorup, J. Becher, *J. Org. Chem.* **2000**, *65*, 5794-5805.

[38] H. Li, C. Lambert, *Chem. Eur. J.* **2006**, *12*, 1144-1155.

[39] Y. Salinas, M. V. Solano, R. E. Sørensen, K. R. Larsen, J. Lycoops, J. O. Jeppesen, R. Martínez-Máñez, F. Sancenón, M. D. Marcos, P. Amorós, C. Guillem, *Chem. Eur. J.* **2014**, *20*, 855.

[40] M. V. Solano, E. A. D. Pia, M. Jevric, C. Schubert, X. Wang, C. Van der Pol, K. Nørgaard, D. M. Guldi, M. B. Nielsen, J. O. Jeppesen, *Chem. Eur. J.* **2014**, *20,* 9918-9929.

[41] C. Rovira, D. Ruiz-Molina, O. Elsner, J. Vidal-Gancedo, J. Bonvoisin, J.-P. Launay, J. Veciana, *Chem. Eur. J.* **2001**, 7, 240-250.

[42] In previous work, see Refs. [30,31], we were not able to observe the IET transition of **1**, since we used slightly acidic solvents such as CH₂Cl₂. Such an IET transition appears as a very weak and broad band if properly treated solvents (fresh distilled and filtered through basic alumina) are used.

[43] V. Mukherjee, N. P. Singh, *Spectrochim. Acta A*, **2014**, *117*, 315-322.

[44] J. Guasch, X. Fontrodona, I. Ratera, C. Rovira, J. Veciana, *Acta. Cryst.*, **2013**, *69*, 255.

[45] A. Girlando, L. Grisanti, M. Masino, I. Bilotti, A. Brillante, R. G. Della Valle, E. Venuti, *Phys. Rev. B* **2010**, *82*, 035208.

[46] S. R. González, B. Nieto-Ortega, R. C. González Cano, V. Lloveras, J. J. Novoa, F. Mota, J. Vidal-Gancedo, C. Rovira, J. Veciana, E. Del Corro, M. Taravillo, V. G. Baonza, J. T. López Navarrete, J. Casado, *J. Chem. Phys.* **2014**, 164903, 1-9.

[47] C. Pecile, A. Painelli, A. Girlando, *Mol. Cryst. Liq. Cryst.* **1989**, *171*, 69-73.

[48] R. Bozio, I. Zanon, A. Girlando, C. Pecile, *J. Chem. Phys.* **1979**, *71*, 1979-1985.

[49] S. Matsuzaki, T. Moriyama, K. Toyoda, **1980**, *34*, 857-859.

[50] S. Matsuzaki, M. Onomichi, H. Tomura, S. Yoshida, K. Toyoda, *Mol. Cryst. Liq. Cryst.* **1985**, *120*, 93-96.

[51] M. J. Frisch, G. W. Trucks, H. B. Schlegel, G. E. Scuseria, M. A. Robb, J. R. Cheeseman, G. Scalmani, V. Barone, B. Mennucci, G. A. Petersson, H. Nakatsuji, M. Caricato, X. Li, H. P. Hratchian, A. F. Izmaylov, J. Bloino, G. Zheng, J. L. Sonnenberg, M. Hada, M. Ehara, K. Toyota, R. Fukuda, J. Hasegawa, M. Ishida,T. Nakajima, Y. Honda, O. Kitao, H. Nakai, T. Vreven, J. A. Montgomery, Jr., J. E. Peralta, F. Ogliaro, M. Bearpark, J. J. Heyd, E.Brothers, K. N. Kudin, V. N. Staroverov, T. Keith, R. Kobayashi,Normand, K. Raghavachari, A. Rendell, J. C. Burant, S. S. Iyengar, J. Tomasi, M. Cossi, N. Rega, J. M. Millam, M. Klene, J. E. Knox, J. B. Cross, V. Bakken, C. Adamo, J. Jaramillo, R. Gomperts, R. E. Stratmann, O. Yazyev, A. J. Austin, R. Cammi, C. Pomelli, J. W. Ochterski, R. L. Martin, K. Morokuma, V. G. Zakrzewski, G. A. Voth, P. Salvador, J. J. Dannenberg, S. Dapprich, A. D. Daniels, O. Farkas, J. B. Foresman, J. V. Ortiz, J. Cioslowski, and D. J. Fox, Gaussian, Inc., Wallingford CT, 2010.

[52] R. Cammi, J. Tomasi, *J. Comput. Chem.* **1995**, *16*, 1449-15458.

[53] L. Grisanti, G. F'Avino, A. Painelli, J. Guasch, I. Ratera, J. Veciana, *J. Phys. Chem. B.* **2009**, *113*, 4718-4725.

[54] A. Ipatov, F. Cordova, L. J. Doriol, M. Casida, *J. Molec. Struct., TEOCHEM* **2009**, *914*, 60-73

[55] A. Dreuw, M. Head-Gordon, *Chem. Rev.* **2005**, *105*, 4009-4039, and references cited therein.

[56] C. Adamo, D. Jacquemin, *Chem. Soc. Rev.* **2013**, *42*, 845-856.

Entry for the Table of Contents

FULL PAPER
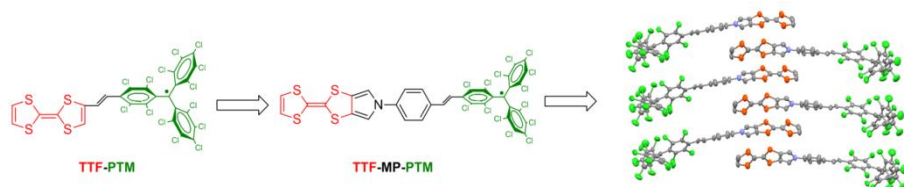
Manuel Souto, Marta V. Solano, Imma Ratera, Morten Jensen, Dan Bendixen, Francesca Delchiaro, Alberto Girlando, Anna Painelli, Jan O. Jeppesen, Concepció Rovira,Jaume Veciana*

An electron donor-acceptor dyad based on a polychlorotriphenylmethyl (PTM) radical subunit linked to a tetrathiafulvalene (TTF) unit through a π-conjugated *N*-phenyl-pyrrole-vinylene bridge has been synthesized and characterized. The intramolecular electron transfer (IET) process and magnetic properties of the radical dyad have been evaluated by cyclic voltammetry, UV-Vis, vibrational, and ESR spectroscopies both in solution and in the solid state. The self-assembling ability of the radical dyad and of its protonated non-radical analogue has been investigated by X-ray crystallographic analysis which reveals that the radical dyad produces a supramolecular architecture with segregated donor and acceptor units where the TTF subunits are arranged in 1-D herringbone type stacks. Analysis of the X-ray data at different temperatures suggests that the two non-equivalent molecules that form the asymmetric unit of the crystal of the radical dyad evolve into an opposite degree of electronic delocalization as the temperature decrease.

Supporting Information

Contents

General methods for synthesis and characterization

Synthesis and characterization of **8**

Synthesis and characterization of **10**

Synthesis and characterization of **2**

^{1}H NMR spectrum of **10**

Cyclic Voltammetry of compounds **5** and **2**

UV/Vis-NIR spectra of compound **2**

ESR spectra of compound **2**

Temperature dependent ESR spectra of compounds **1** and **2**

Crystallographic data of compounds **10** and **2**

Single crystal structure of compound **10**

Raman spectra of compounds **1** and **2**

Mulliken charge distributions and spin density for **1** and **2**

Calculated reduction and potential energies for **1** and **2**

Mulliken charge and spin density distributions for **2A** and **2B** at 150K and 300K

Molecular orbitals **1** and **2**

References for Supporting Information

General methods for synthesis and characterization

^{1}H NMR spectra were recorded using a Bruker Avance 250, 400, or 500 instruments and Me$_4$Si as an internal standard. Infrared spectra were recorded with Spectrum One FT-IR Spectroscopy instrument and UV/Vis/NIR spectra were measured using Cary 5000E Varian. ESR spectra were performed with a Bruker ESP 300 E equipped with a rectangular cavity T102 that works with an X-band (9.5 GHz). The solutions were degassed by argon bubbling before the measurements. LDI/TOF MS were recorded in a Bruker Ultraflex LDI-TOF spectrometer. Cyclic voltammetry measurements were obtained with a potentiostat 263a from EG&G Princeton Applied Research in a standard 3 electrodes cell. The Raman spectra of **1**, **1**[+.], and **2** are FT–Raman spectra obtained in a Bruker Equinox 55 FT–IR interferometer using a Raman accessory kit (FRA/106–S). A continuous–wave Nd–YAG laser working at 1064 nm was employed for excitation. A germanium detector operating at liquid nitrogen temperature was used. Raman scattering radiation was collected in a back–scattering configuration with a standard spectral resolution of 4 cm^{-1}. 1000-3000 scans were averaged for each spectrum. The Raman spectra of **2** at 120 K have been collected with the Renishaw 1000 microspectro-meter, with 752 nm excitation. The laser power has been kept to the minimum (less than 1 mW at the sample) to avoid sample degradation. The IR-NIR spectra have been collected with a Bruker FT-IR IFS-66 spectrometer equipped with a Hyperion microscope. The spectral resolution is about 2 cm^{-1} for both spectrometers. For the low-temperature spectra, it has been used a Linkam stage. All reagents and solvents employed for the syntheses were of high purity grade and were purchased from Sigma-Aldrich Co., Merck, and SDS. Dry solvents were used in the chemical reactions and in the cyclic voltammetries. The solvents used for optical spectroscopy and ESR measurements were of HPLC grade (ROMIL-SpS). In addition, for cyclic voltammetry experiments, CH$_2$Cl$_2$ was filtered over basic alumina to eliminate the acidic residues.
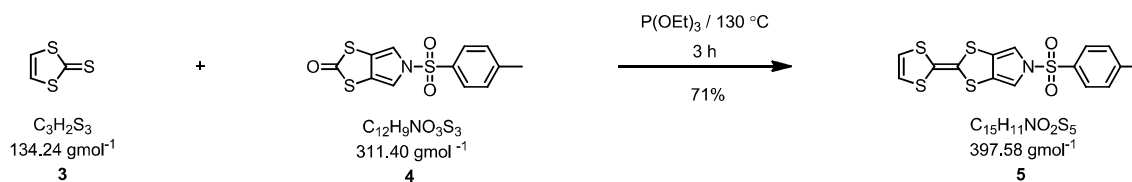
Synthesis and characterization:

Synthesis of Compound 8
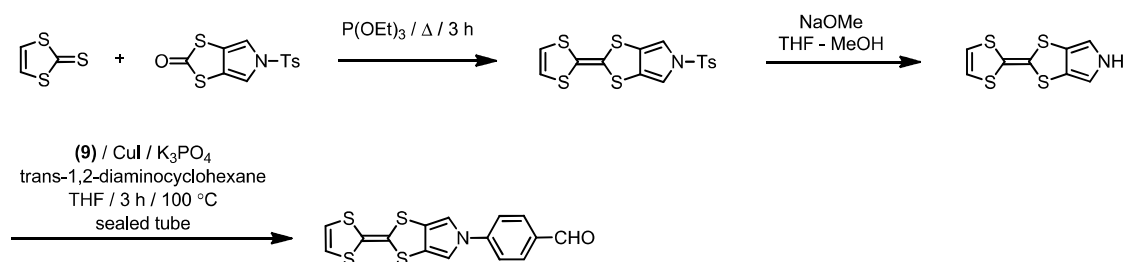
Scheme S1. Global synthesis of compound **8**.

2-(1,3-Dithiol-2-yliden)-5-tosyl-(1,3)-dithiolo[4,5-*c*]pyrrole (5):[S2,S3]
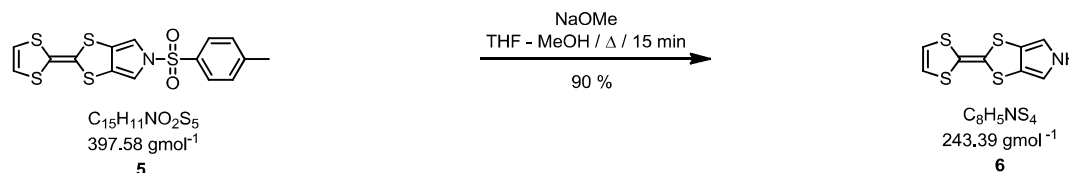

Scheme S2. Synthesis of compound **10**.

A degassed solution of 1,3-dithiol-2-thione (**3**)[S2] (0.49 g, 3.65 mmol) and 5-tosyl-(1,3)-dithiolo[4,5-*c*]pyrrol-2-one (0.75 g, 2.43 mmol) (**4**) dissolved in freshly distilled P(OEt)$_3$ (30 mL) was heated at 130 °C. After 10 min another portion of **4** (0.49 g, 3.65 mmol, 7.35 eq in total) was added. The reaction mixture was heated for 3 h before being cooled to room temperature. Addition of cold MeOH (50 mL) produced a yellow precipitate, which was filtered and washed with MeOH (3 × 15 mL). The resulting solid was dried and then dissolved in a small portion of CH$_2$Cl$_2$ and subjected to purification by flash chromatography (SiO$_2$, CH$_2$Cl$_2$: Petroleum Ether, 1:2, v/v, gradient elution). The yellow band (R_f = 0.6, CH$_2$Cl$_2$: Petroleum Ether, 1:1) was collected and the solvent evaporated affording **5** (0.68 g, 71%) as a yellow solid (mp = 250 °C). **Characterization**: [1]**H NMR** (400 MHz, CD$_3$SOCD$_3$) δ (ppm) = 2.38 (s, 3H,

Ts-CH$_3$), 6.74 (s, 2H, HC=CH), 7.36 (s, 2H, α-H pyrrole), 7.46 (d, 2H, J = 8.2 Hz, Ar-H), 7.83 (d, 2H, J = 8.2 Hz, Ar-H). ^{13}C NMR (100 MHz, CD$_3$SOCD$_3$) δ (ppm) = 21.1 (Ts-CH$_3$), 112.4 (pyrrole α-C), 112.7 (fulvalene C=C), 118.7 (fulvalene C=C), 119.6 (HC=CH), 126.7 (dithiol =C-C=), 126.9 (Ar-C-2), 130.4 (Ar-C-3), 134.5 (Ar-C-1), 145.8 (Ar-C-4). **MS (EI)**: m/z (%) = 394.96 [M$^+$, 100]. **IR** (KBr) ν(cm^{-1}) = 3137, 1635, 1596, 1370 (SO$_2$), 1225, 1172 (SO$_2$), 1090, 1055, 680. **CV** (n-Bu$_4$NPF$_6$ 0.1 M in CH$_3$CN at 298 K vs Ag/AgCl): $E_{1/2}{}^1$ = +0.27 V; $E_{1/2}{}^2$ = +0.49 V. **Elemental Analysis**: Anal. Calcd. for C$_{15}$H$_{11}$NO$_2$S$_5$: C: 45.31; H: 2.79; N: 3.52. Found: C: 44.82; H: 2.86; N: 3.40.

2-{1,3-Dithiol-2-ylidene}-(1,3)-dithiolo[4,5-c] pyrrole (6):^{S3}

$C_{15}H_{11}NO_2S_5$
397.58 gmol^{-1}
5

NaOMe
THF - MeOH / Δ / 15 min
90 %

$C_8H_5NS_4$
243.39 gmol^{-1}
6

Scheme S3. Synthesis of compound **6**.

Compound **5** (0.46 g, 1.15 mmol) was dissolved in a mixture of anhydrous THF - MeOH (1:1, v/v, 24 mL). The solution was degassed for 20 min under Argon atmosphere, whereupon a solution of NaOMe in MeOH (25%, ca 1.4 mL, 1.0 g, 25 mmol) was added in one portion. The mixture was refluxed at 78 °C for 15 min, then cooled to room temperature and concentrated to half volume. Water (50 mL) was added, producing a yellow precipitate, where after the suspension was extracted with CH$_2$Cl$_2$ (2 × 20 mL). The combined organic phases were washed with H$_2$O (2 × 20 mL) and brine (2 × 20 mL) and subsequently dried (MgSO$_4$). After evaporation of the solvent, the green crude product was purified by flash chromatography (SiO$_2$ deact, CH$_2$Cl$_2$). The yellow band (R_f = 0.6, CH$_2$Cl$_2$) was collected and the solvent evaporated to afford **6** (0.25 g, 90%) as a yellow powder (mp = 190-191 °C). **Characterization**: ^{1}**H NMR** (500 MHz, CDCl$_3$) δ (ppm) = 6.72 (s, 2H, HC=CH), 6.78 (d, 2H, J = 2.71 Hz, pyrrole α-H), 11.08 (s, 1H, NH). ^{13}**CNMR** (125 MHz, CDCl$_3$) δ (ppm) = 109.7 (pyrrole α-C), 115.3 (fulvalene C=C), 116.2 (fulvalene C=C), 118.7 (dithiol =C-C=), 120.6 (HC=CH). **MS (EI)**: m/z (%) = 243 [M$^+$, 100]. **IR** (KBr) ν(cm^{-1}) = 3410 (NH stretch), 3124, 1629 (NH), 1531, 1252 (C-N). **CV** (n-Bu$_4$NPF$_6$ 0.1 M in CH$_3$CN at 298 K vs Ag/AgCl): $E_{1/2}{}^1$ = +0.37 V; $E_{1/2}{}^2$ = +0.72 V. **Elemental Analysis**: Anal. Calcd. for C$_6$H$_5$NS$_4$: C: 39.48; H: 2.07; N: 5.75. Found: C: 40.18; H: 2.11; N: 5.44.

N'-Formylphenyl-2-{1,3-dithiol-2-ylidene}-(1,3)-dithiolo[4,5-c]pyrrole (8):

$C_8H_5NS_4$
243.39 g mol^{-1}
6

+

C_7H_5IO
232.02 g mol^{-1}
7

CuI / K$_3$PO$_4$ / C$_6$H$_{14}$N$_2$
THF / 3 h / 105 °C / sealed tube
59 %
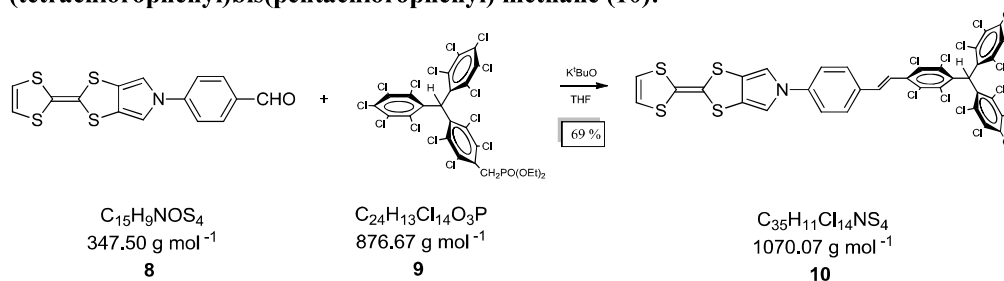
$C_{15}H_9NOS_4$
347.50 g mol^{-1}
8
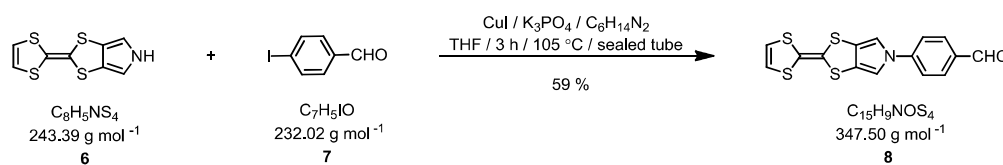
Scheme S4. Synthesis of compound **8**.

A Schlenk tube containing a mixture of compound **6** (71 mg, 0.291 mmol), 4-iodobenzaldehyde (**7**) (171 mg, 7.37 mmol), K$_3$PO$_4$ (230 mg, 10.8 mmol), and CuI (113 mg, 5.93 mmol) dissolved in freshly distilled THF (5 mL) was degassed under argon for 15 min, where after ±-trans-1,2-diaminocyclohexane (0.1 mL, 0.83 mmol) was added to the solution and the vial capped. The reaction mixture was heated for 3 h at 105 °C, cooled to room temperature and the solution was extracted with CH$_2$Cl$_2$ and washed with water (4 × 20 mL). The combined organic phases were combined, dried (MgSO$_4$) and concentrated to give an orange solid that was purified using flash chromatography (SiO$_2$, CH$_2$Cl$_2$:Toluene, 1:1, v/v). The yellow band (R_f = 0.3, CH$_2$Cl$_2$:Toluene, 1:1) was collected and concentrated to provide the desired compound **8** as a red solid (59.7 mg, 59 %). Shiny crystals of **8** were obtained from CH$_2$Cl$_2$:Et$_2$O (1:1). **Characterization**: ^{1}**H NMR** (500 MHz, CD$_3$SOCD$_3$) δ (ppm) = 9.98 (s, 1 H, -CHO), 7.94 (d, 2H, J = 8.2 Hz, Ar-H), 7.45 (d, 2H, J = 8.2 Hz, Ar-H), 6.99 (s, 2H, pyrrole α-H), 6.34 (s, 2 H, HC=CH). ^{13}**C NMR** (125 MHz, CD$_3$SOCD$_3$) δ (ppm) = 190.8, 136.2, 131.7, 126.6, 119.7, 119.0, 118.6, 110.1.(2 lines are missing/overlapping). **MALDI-MS** (DCTB): m/z (%) = 347.6 [M$^+$, 100]. **CV** (n-Bu$_4$NPF$_6$ 0.1 M in

CH₃CN at 298 K): $E_{1/2}^1$ = +0.28 V; $E_{1/2}^2$ = +0.64 V. **Elemental Analysis**: Anal. Calcd. for $C_{15}H_9NOS_4$: C: 51.85; H: 2.61; N: 4.03. Found: C: 51.33; H: 2.49; N: 3.65.

Synthesis of Compound 10

N'-Vinylenephenyl-2-{1,3-dithiol-2-ylidene}-(1,3)-dithiolo[4,5-c]pyrrole-2,3,5,6-(tetrachlorophenyl)bis(pentachlorophenyl) methane (10):


$C_{15}H_9NOS_4$	$C_{24}H_{13}Cl_{14}O_3P$	$C_{35}H_{11}Cl_{14}NS_4$
347.50 g mol⁻¹	876.67 g mol⁻¹	1070.07 g mol⁻¹
8	**9**	**10**

Scheme S5. Synthesis of compound **10**.

The phosphonated PTM derivative **9**[S1] (344 mg, 0.39 mmol) was dissolved in anhydrous THF (60 mL) under strict inert conditions, whereupon the solution was cooled down to -78 °C. Potassium *tert*-butoxide (98 mg, 0.87 mmol) was added and the reaction mixture was stirred for 20 minutes to form the yellow-orange ylide. Susequently, the MPTTF compound **8** (150 mg, 0.43 mmol) was added and the reaction mixture was allowed to warm up to room temperature. After being stirred for 3 d at room temperature, the reaction mixture was extracted with CH₂Cl₂, washed with H₂O, and dried (MgSO₄). The solvents were evaporated and the crude product was purified by column chromatography (SiO₂, Et₂O:hexanes, 1:1, v/v) to provide the desired compound **10** as a light orange powder (290 mg, 69%). **Characterization**: **¹H NMR** (400 MHz, CD₃SOCD₃) δ (ppm) = 7.75 (d, 2H, J = 8.2 Hz, Ar-**H**), 7,59 (d, 2H, J = 8.2 Hz, Ar-**H**), 7.53 (s, 2H, pyrrole α-**H**), 7.22 (d, 1H, J = 16.8 Hz, Phenyl-C**H**=CH-PTM), 7.13 (d, 1H, J = 16.8 Hz, Phenyl-CH=C**H**-PTM), 6.95 (s, 1H, α**H**), 6.76 (s, 2H, **H**C=C**H**). **FT-IR** ν(cm⁻¹) = 2955 (w), 2922 (w), 2855 (w), 1728 (w), 1602 (m, CH=CH), 1517 (s), 1487 (m), 1461 (w), 1381 (m), 1370 (m), 1335 (m), 1309 (s), 1185 (m), 1138 (m), 1038 (m), 967 (m), 936 (m), 869 (w), 806 (s), 750 (m), 691 (m). **UV-VIS-NIR** (CH₂Cl₂, λ_{max} (nm), ε in (M⁻¹·cm⁻¹)) = 327 (15958); 377 (14848). **LDI-TOF** (positive mode): m/z (amu/e⁻): 1069.721 **CV** (n-Bu₄NPF₆ 0.1 M in CH₂Cl₂ as electrolyte vs Ag/AgCl): $E_{1/2}^1$ = +0.49 V; $E_{1/2}^2$ = + 0.99 V.

Synthesis of Compound 2

N'-Vinylenephenyl-2-{1,3-dithiol-2-ylidene}-(1,3)-dithiolo[4,5-c]pyrrole-2,3,5,6-(tetrachlorophenyl)bis(pentachlorophenyl) methyl radical (2):

$C_{35}H_{11}Cl_{14}NS_4$	$C_{35}H_{10}Cl_{14}NS_4$
1070.07 g mol⁻¹	1069.06 g mol⁻¹
10	**2**
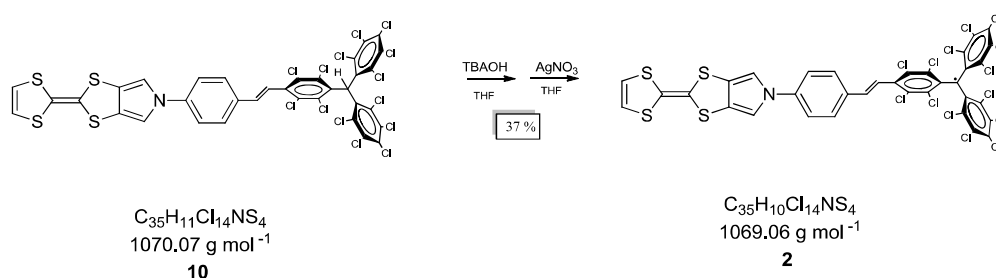
Scheme S6. Synthesis of compound **2**.

Compound **10** (90 mg, 0.08 mmol) was dissolved in distilled CH₂Cl₂ (40 mL) and a solution of n-Bu₄NOH (1.0 M in MeOH, 120 µL, 0.12 mmol) was added. The purple reaction mixture was stirred for 4 h before AgNO₃ (24 mg, 0.14 mmol) dissolved in acetonitrile (10 mL) was added. The reaction mixture was then stirred for further 90 min and the solution changes color from purple to dark brown and a precipitate of silver (Ag⁰) was formed. Subsequently, the reaction mixture solution was filtered and the filtrate concentrated. Finally, the crude product was purified by flash column chromatography (SiO₂, CH₂Cl₂:hexanes, 1:1, v/v) to produce the desired TTF-Pyrrole-Phenyl-PTM radical **2** as a dark reddish-brown powder (64 mg, 71%). **Characterization: FT-IR** ν(cm⁻¹) = 2952 (m), 2922 (s), 2855 (m), 1727 (w), 1660 (w), 1626 (w), 1605 (m, CH=CH), 1519 (s), 1456 (w), 1427 (w), 1382 (m), 1335 (s), 1311 (s),

1257 (m), 1183 (m), 1155 (w), 1038 (m), 966 (m), 936 (m), 875 (w), 815 (s), 795 (m), 753 (m), 734 (m). **UV-VIS-NIR** (CH_2Cl_2, λ_{max} (nm), ε ($M^{-1} \cdot cm^{-1}$)) = 199 (13176), 321 (12730), 375 (13207), 386 (16220), 439 (4950). **LDI-TOF** (positive mode): m/z (amu/e$^-$): 1069.643 [M]$^+$·, 997.698 [M − 70]$^+$, (negative mode): 1069.653 [M]$^-$·. **CV** (n-Bu$_4$NPF$_6$ 0.1 M in CH_2Cl_2 as electrolyte vs Ag/AgCl): $E_{1/2}^1$ = −0.19 V, $E_{1/2}^2$ = +0.45 V, $E_{1/2}^3$ = +0.95. **ESR** (CH_2Cl_2) g = 2.0025.

^{1}H NMR spectrum of 10
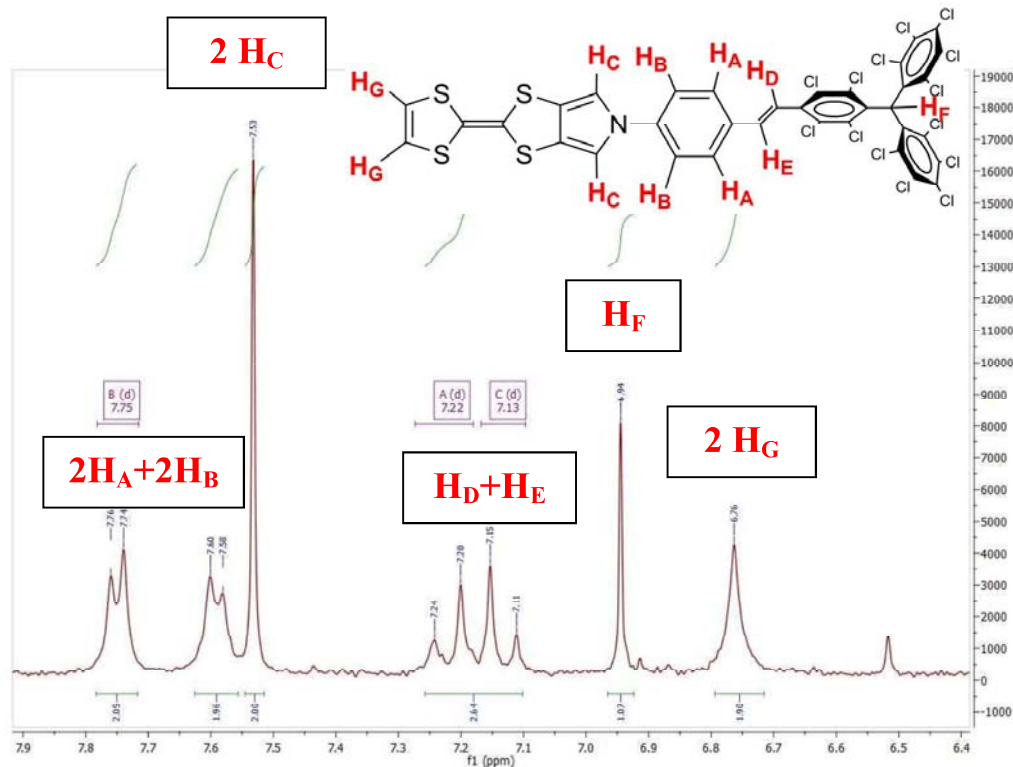
Figure S1. ^{1}H NMR spectrum (400 MHz) of dyad **10** recorded in CD$_3$SOCD$_3$ at 300 K and assignments of the protons observed in the ^{1}H NMR spectrum.

Cylic Voltametry of 10 and 2
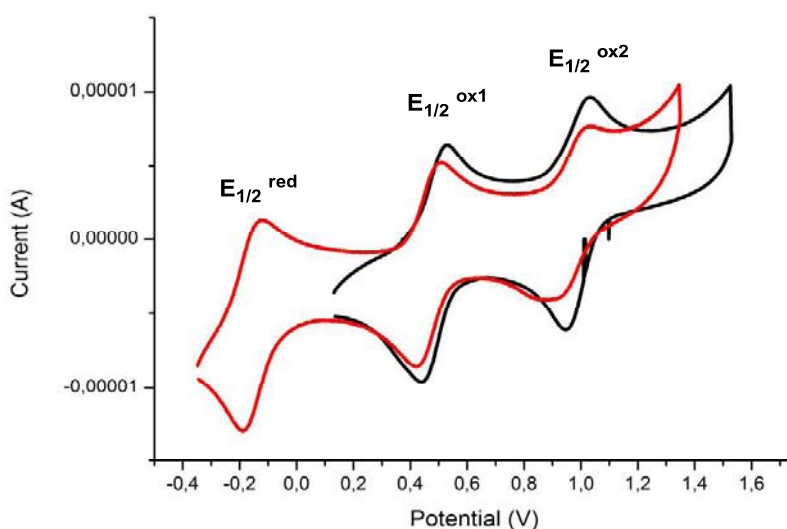
Figure S2. Cyclic voltammograms (vs. Ag/AgCl) recorded of solutions of compounds **10** (black line) and **2** (red line) (0.5 mM) in CH_2Cl_2 using n-Bu$_4$PF$_6$ (0.1 M) as electrolyte at 300 K under argon at a scan rate of 0.1 V s^{-1}.

S5
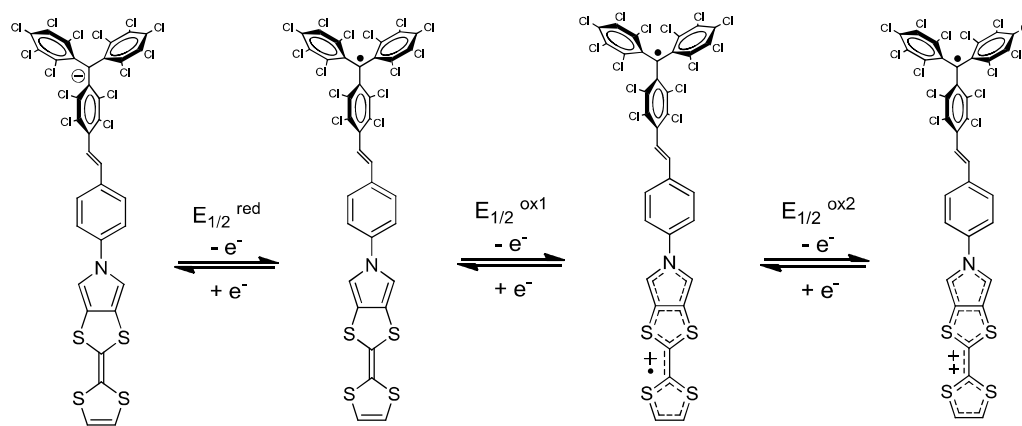
Scheme S7. Possible oxidation states of dyad **2.**

UV-Vis-NIR spectra of compound 2
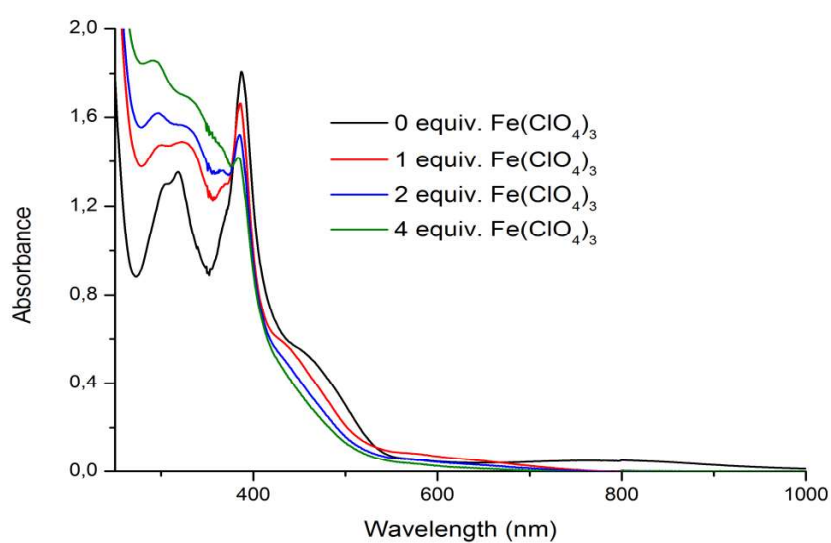
Figure S3. Absorption spectra of dyad **2** (0.05 mM) recorded in THF at 300 K and those of the oxidized species arising from the stepwise addition of Fe(ClO$_4$)$_3$.
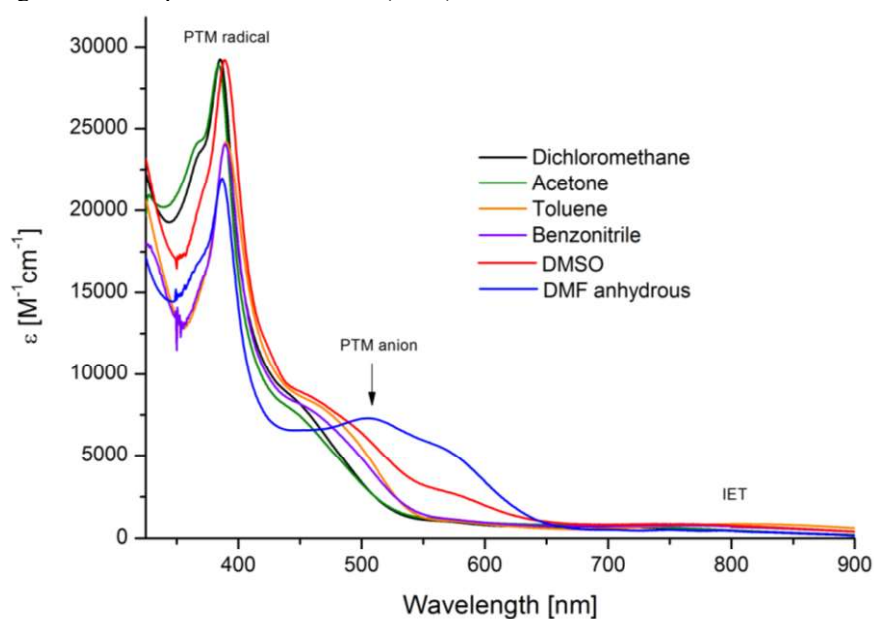
Figure S4. UV/Vis-NIR spectra of dyad **2** recorded at 300 K in different solvents.

ESR spectra of compound 2
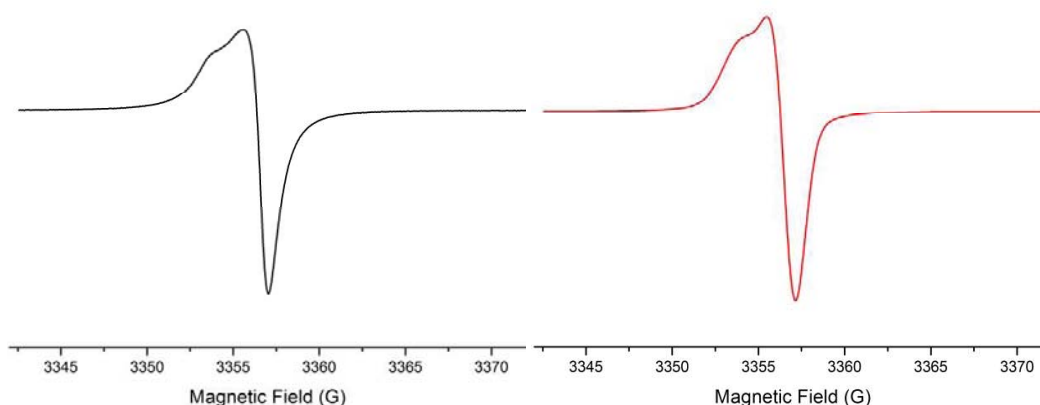
Figure S5. Experimental (black lines) and simulated (red lines) ESR spectra of neutral crystals of dyad **2** at 120 K.

Temperature dependent ESR spectra of compound 1 and TTF-PTM radical
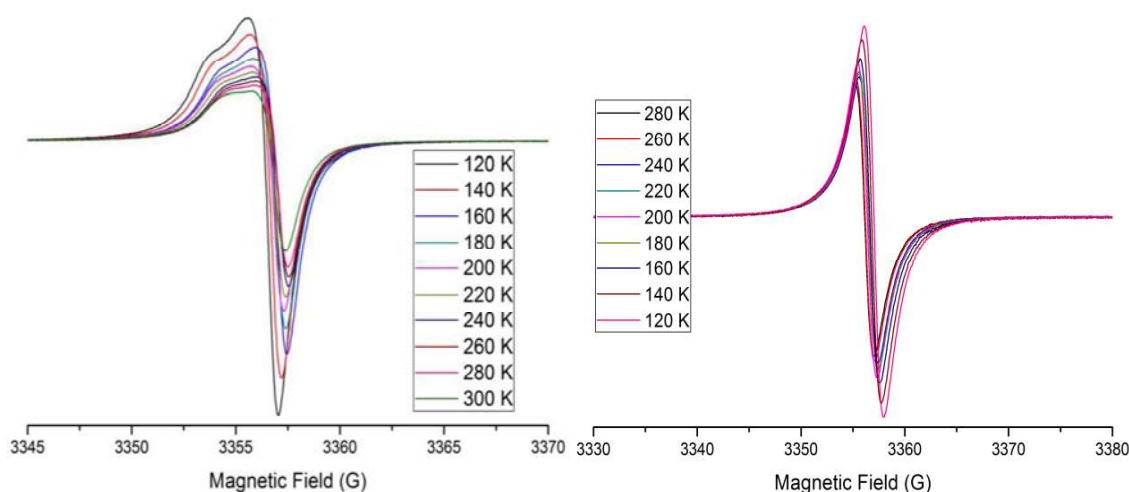
Figure S6. ESR spectra of neutral crystals of dyad **2** (left) and microcrystalline powder of **1** (right) at different temperatures.
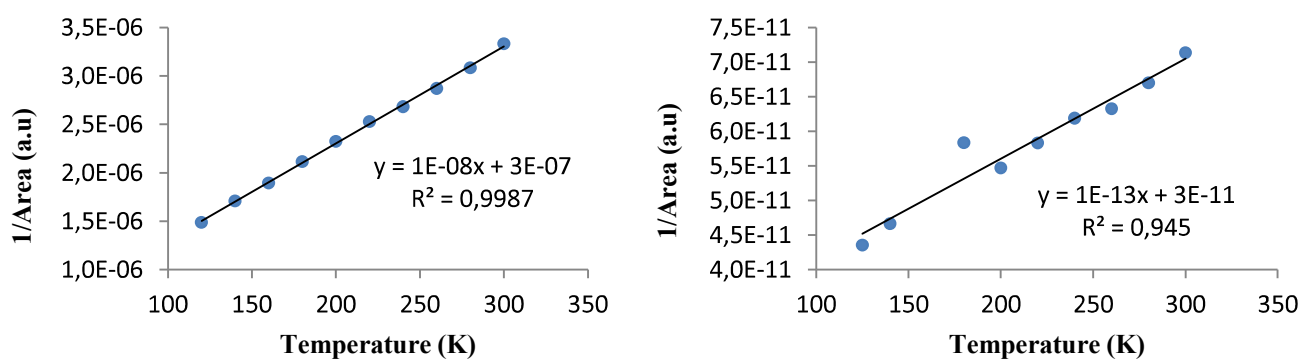
Figure S7. Temperature dependence on double integral intensity of ESR spectra of neutral crystals of dyad **2** (left) and microcrystalline powder of **1** (right).

Crystallographic data for 10 and 2

Table S1. Summary of the crystallographic data of **5** and **2** (150 and 300 K).

	10	2 (300 K)	2 (150 K)
Molecular formula	$C_{35} H_{11} Cl_{14} N S_4$	$C_{35} H_{10} Cl_{14} N S_4$	$C_{35} H_{10} Cl_{14} N S_4$
Formula weigth	1069.99	1068.98	1068.98
Temperature (K)	300	300	150
Crystal System	Triclinic	Monoclinic	Monoclinic
Space group	P-1	P21	P21
Crystal size	0.23 x 0.12 x 0.08 mm	0.24 x 0.24 x 0.08 mm	0.24 x 0.24 x 0.08 mm
a **(Å)**	8.788(5)	17.411(3)	17.374(12)
b **(Å)**	22.273(13)	7.9517(16)	7.711(5)
c **(Å)**	25.440(16)	30.177(6)	29.88(2)
α **(º)**	112.223(13)	90	90
β **(º)**	94.714(16)	103.588(4)	103.363(12)
γ **(º)**	95.984(14)	90	90
$V(\text{Å}^3)$	4636(5)	4061.0(14)	3895(5)
Z	4	4	4
Final R indices [I>2sigma(I)]	$R_1 = 0.1671$, w$R_2 = 0.4027$	$R_1 = 0.0614$, w$R_2 = 0.1036$	$R_1 = 0.0677$, w$R_2 = 0.1005$
R indices (all data)	$R_1 = 0.4058$, w$R_2 = 0.5154$	$R^1 = 0.2193$, w$R_2 = 0.1457$	$R_1 = 0.2429$, w$R_2 = 0.1454$
Goodness-of-fit on F^2	0.925	0.917	0.909

Single crystal structure of compound 10

X-ray diffraction analysis on small dark-red crystals of **10** at 300 K, crystallized by slow evaporation from an $Et_2O:CH_2Cl_2$ (3:2) mixture supports a triclinic system with the P-1 space group.
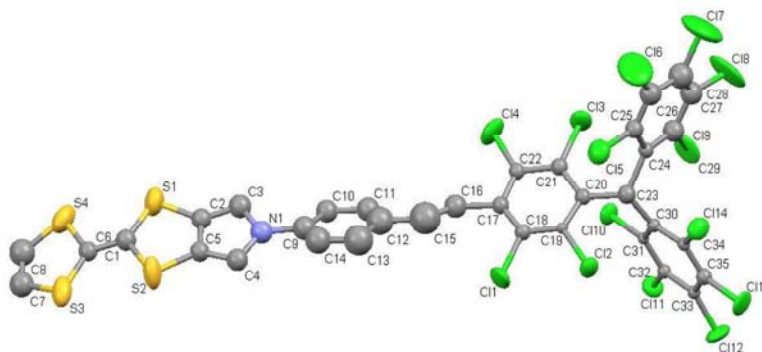
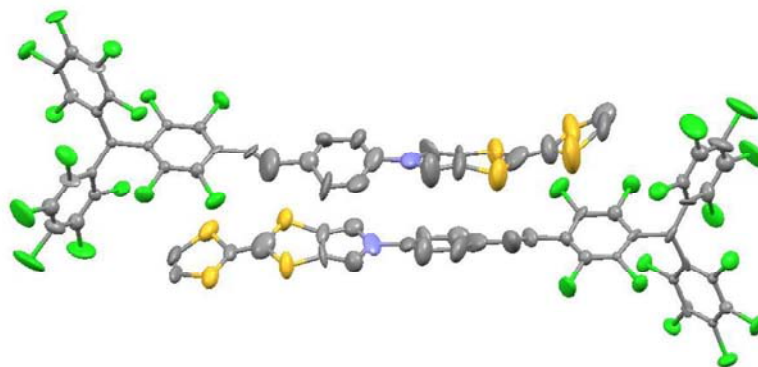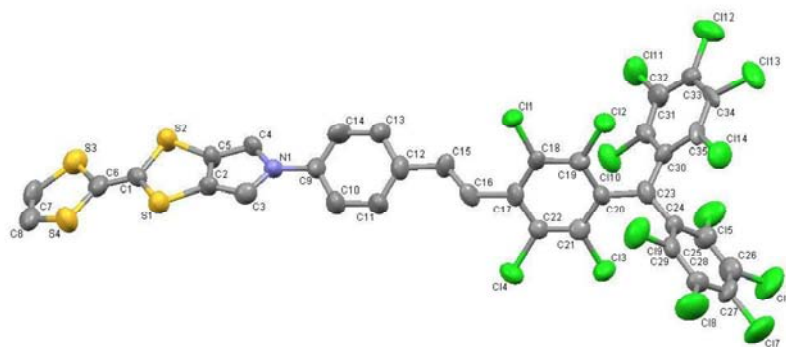**Figure S8**. An ORTEP view of **10** at 300 K. Hydrogen atoms have been omitted for clarity.

Figure S9. Asymmetric unit of **10**.

Table S2. Selected bond lengths, angles, and torsion angles of **10** and **2** (300 and 150 K).

Atoms	10A	10B	2A (300 K)	2B (300 K)	2A (150 K)	2B (150 K)
TTF (C=C)	(Å)	(Å)	(Å)	(Å)	(Å)	(Å)
C7-C8	1.206	1.410	1.315	1.281	1.275	1.330
C6-C1	1.411	1.440	1.372	1.363	1.289	1.328
C2-C5	1.391	1.448	1.387	1.455	1.400	1.414
Average	**1.336**	**1.430**	**1.358**	**1.366**	**1.321**	**1.357**
TTF (C-S)						
C7-S3	1.751	1.904	1.718	1.733	1.806	1.703
C8-S4	1.778	1.641	1.726	1.738	1.729	1.655
S3-C6	1.698	1.776	1.777	1.744	1.777	1.756
S4-C6	1.718	1.746	1.727	1.725	1.750	1.720
C1-S1	1.741	1.703	1.755	1.780	1.782	1.784
C1-S2	1.807	1.687	1.758	1.760	1.777	1.759
S1-C2	1.780	1.779	1.761	1.725	1.760	1.731
S2-C5	1.737	1.707	1.758	1.755	1.773	1.739
Average	**1.751**	**1.743**	**1.748**	**1.745**	**1,769**	**1.731**
Conjugation $\Delta\,(\overline{C-S}) - (\overline{C=C})$	**0.409**	**0.313**	**0.390**	**0.379**	**0.448**	**0.374**
Pyrrole-Phenyl						
N1-C9	1.457	1.534	1.423	1.423	1.447	1.395
Phenyl Region						
C9-C10	1.370	1.430	1.383	1.356	1.390	1.341
C10-C11	1.449	1.349	1.402	1.413	1.407	1.409
C11-C12	1.332	1.514	1.408	1.391	1.336	1.406
C12-C13	1.354	1.360	1.378	1.361	1.335	1.433
C13-C14	1.474	1.419	1.352	1.369	1.364	1.365
C14-C9	1.388	1.341	1.380	1.371	1.380	1.403
Conjugation $\Delta\,(\overline{C-C}) - (\overline{C=C})$	**0.085**	**0.104**	**0.027**	**0.029**	**0.045**	**0.039**
Vinylene Region						
C12-C15	1.540	1.659	1.492	1.462	1.515	1.434
C15-C16	1.210	1.212	1.323	1.286	1.290	1.355
C16-C17	1.530	1.458	1.497	1.441	1.478	1.456
Conjugation $\Delta\,(\overline{C-C}) - (\overline{C=C})$	**0.325**	**0.346**	**0.172**	**0.166**	**0.207**	**0.09**
PTM *ipso*-Carbon						
C20-C23	1.526	1.540	1.481	1.441	1.455	1.436
C23-C24	1.496	1.557	1.462	1.477	1.434	1.452
C23-C30	1.554	1.534	1.446	1.490	1.474	1.505
Average	**1.525**	**1.544**	**1.463**	**1.469**	**1.454**	**1.464**
Average C-Cl (*o*-position PTM)	**1.730**	**1.752**	**1.721**	**1.721**	**1.709**	**1.723**

Angle(º)						
C12-C15-C16	123.37	122.58	126.59	128.20	128.76	123.22
Torsion Angle(º)						
S3-C6-S4-C8	14.16	11.19	9.93	9.89	10.72	8.83
C7-C8-S4-C6	8.11	11.06	6.61	8.84	7.20	6.27
S4-C8-C7-S3	0.12	- 5.98	0.66	- 4.52	0.87	1.05
S1-C2-C5-S2	- 2.84	4.43	0.72	- 0.99	-2.92	0.09
C14-C9-N1-C4	26.14	23.45	31.08	32.15	37.72	35.10

Table S3. Selected intermolecular distances of **10** and **2** at 150 and 300 K.

Atoms	10	2 (150 K)	2 (300 K)
S···S (closest)	3.922 Å	3.846 Å	3.901 Å
Cl···Cl (closest)	3.288 Å	3.375 Å	3.330 Å
S···C (pyrrole)	3.754 Å	3.432 Å	3.449 Å
S···Cl (PTM)	-	3.493 Å	3.524 Å
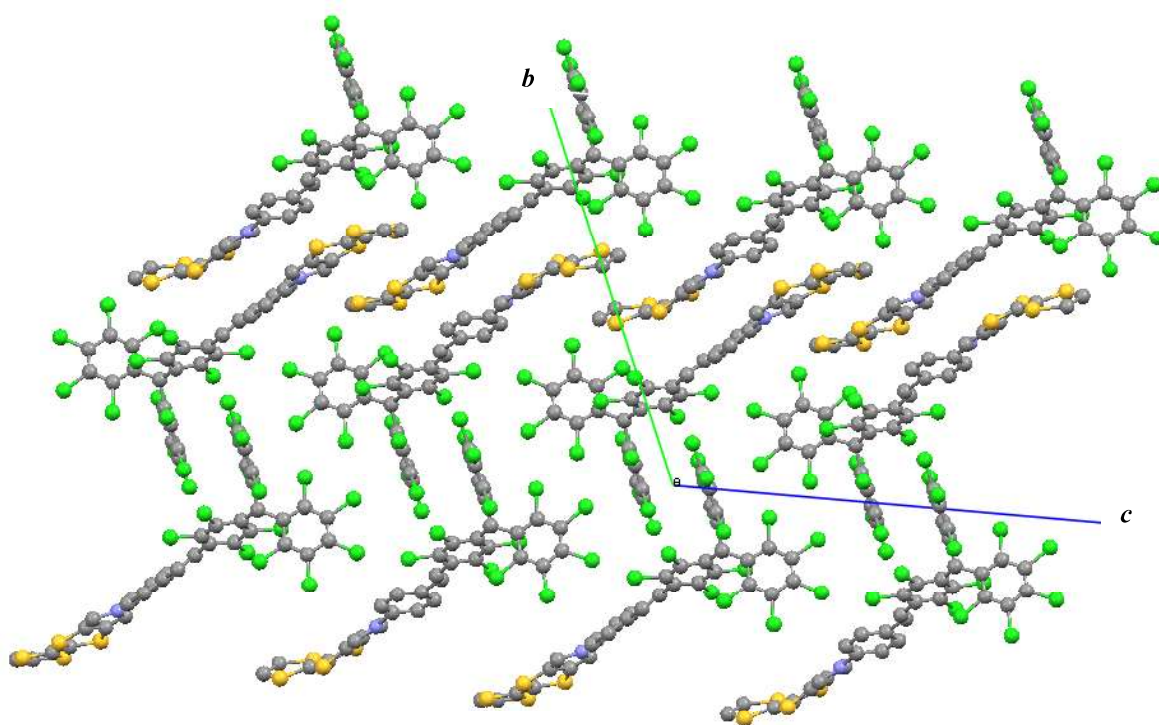
Figure S10. Molecular packing of **10** at 300 K in the *bc* plane.

Figure S11. An ORTEP view of **2** at 300 K. Hydrogen atoms have been omitted for clarity.
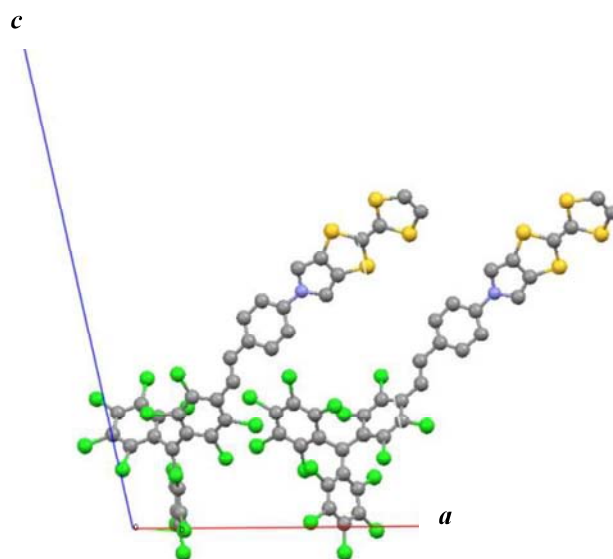
Figure S12. Asymmetric unit of **2** at 300 K in the *ac* plane.
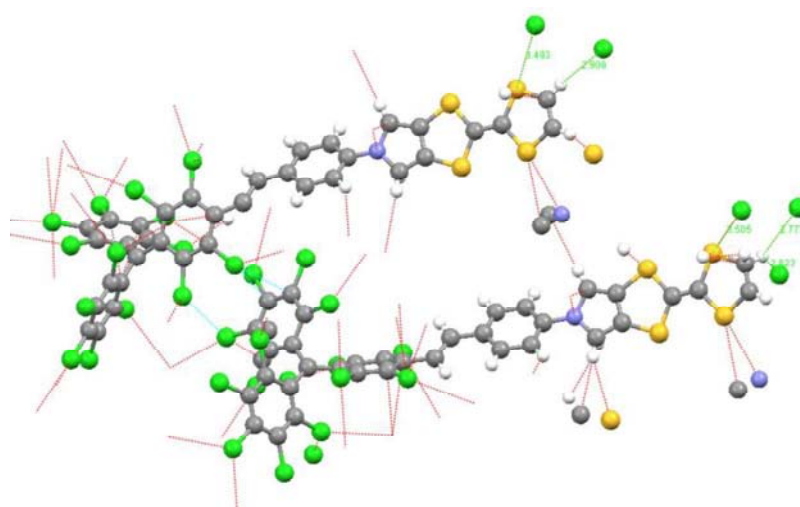
Figure S13. Shorter atomic contacts between molecules **2A** (bottom) and **2B** (top) at 150 K.
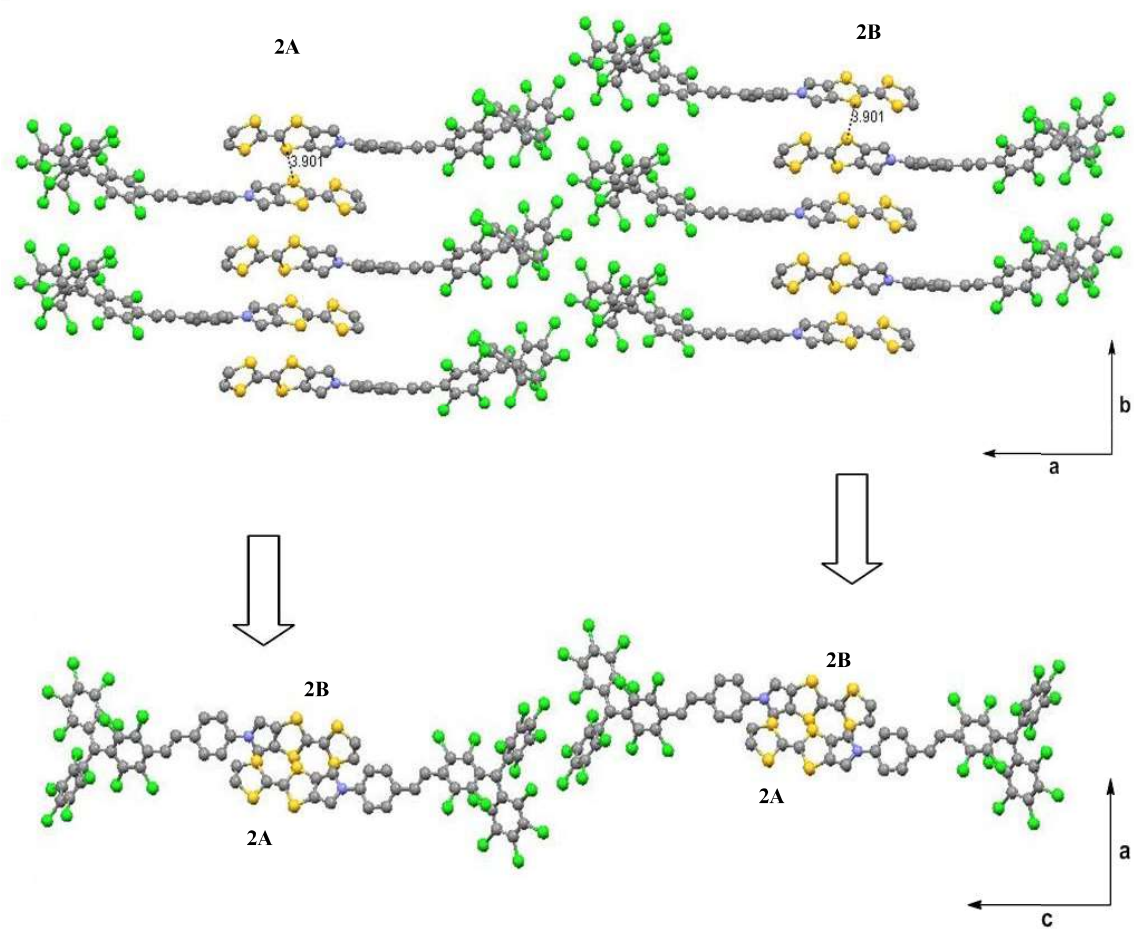
Figure S14. Overview of the molecular packing of **2** at 300 K in the *ab* plane and in the *ac* plane.
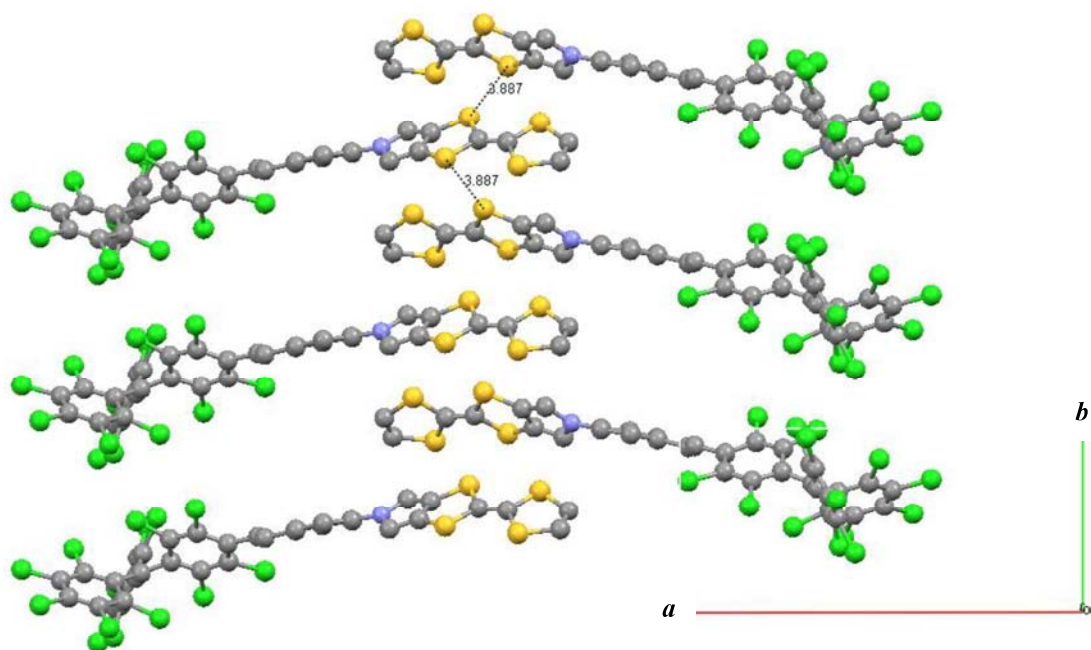
Figure S15. Molecular packing of **2B** at 150 K in the *ab* plane.
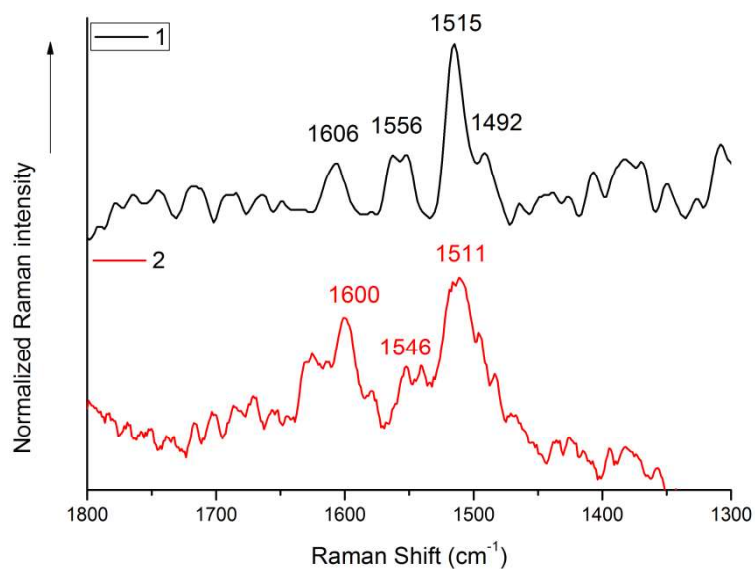
Figure S16. Raman spectra of compounds **1** (black line) and **2** (red line) in the 1800-1300 cm^{-1} shift region recorded at 300 K (Raman laser of 1064 nm).
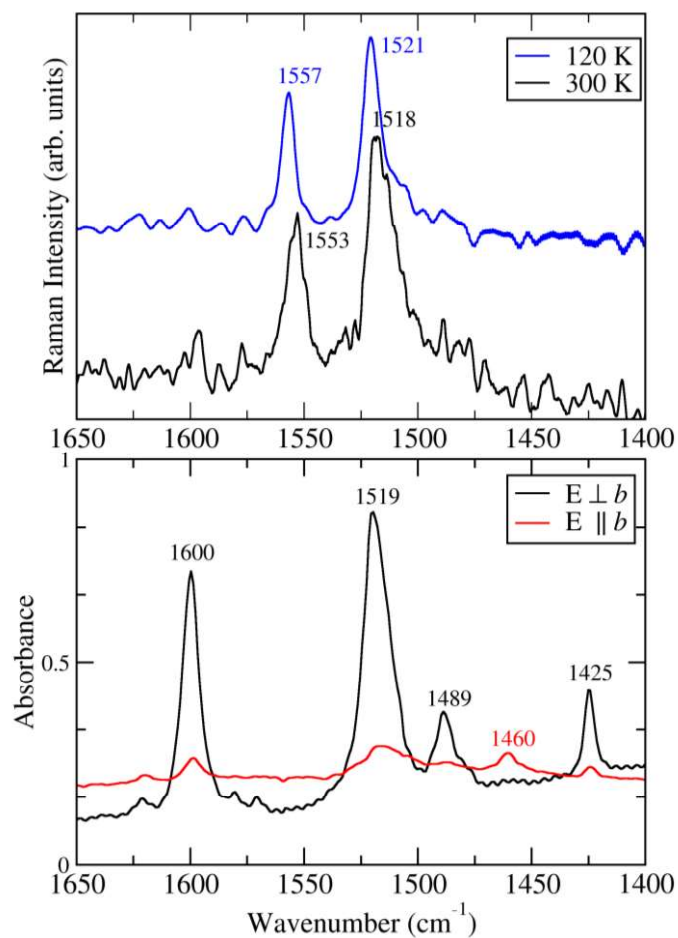
Figure S17. Upper panel: Raman spectra of compound **2** recorded at 300 K (black line) and 120 K (blue line) in the 1600-1450 cm^{-1} spectra region (excting line: 752 nm). Lower panel: polarized IR spectra of **2** at 300 K.

S13
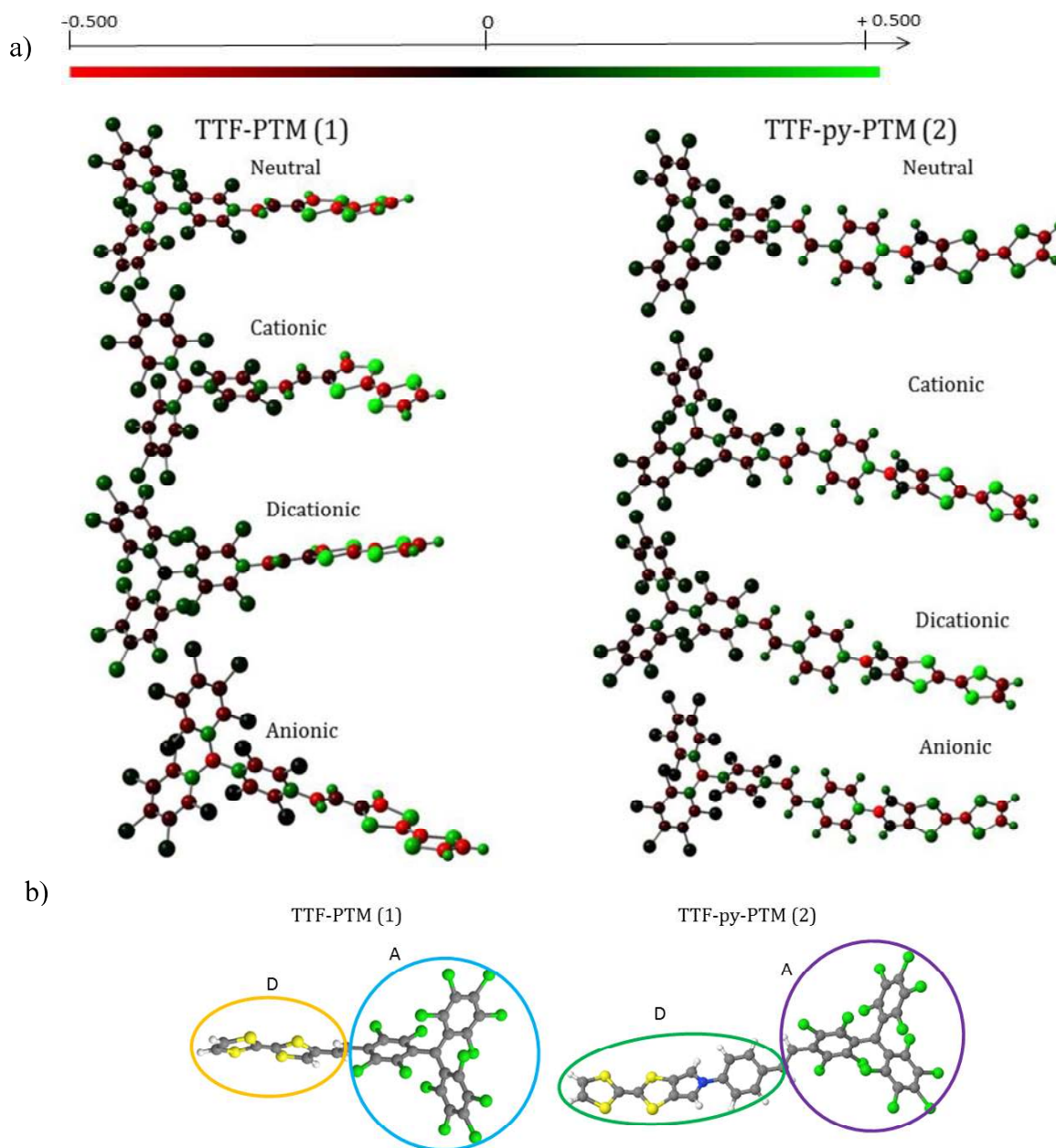
Mulliken charge distribution at UCAMB3LYP/6-31G* with PCM									
Compound	Solvent	Neutral		Cationic		Dicationic		Anionic	
		Donor	Acceptor	Donor	Acceptor	Donor	Acceptor	Donor	Acceptor
(1)	CH_2Cl_2	0.09	-0.09	1.02	-0.02	1.93	0.07	0.04	-1.04
	AcCN	0.09	-0.09	1.03	-0.03	1.93	0.07	0.04	-1.04
(2)	CH_2Cl_2	0.10	-0.10	1.08	-0.08	2.06	-0.06	0.05	-1.05

Figure S18. Mulliken atomic charge distribution referred to neutral, cationic, dicationic and anionic species for both **1** and **2** at UCAMB3LYP/6-31G* with PCM level performed with (Pop=MBS) keyword[S5]. The table shows the charges on the D and A fragments, defined in panel *b*.

(U)CAMB3LYP/6-31+G* with PCM model			
Compound	1Red (V)	1Ox (V)	2Ox (V)
TTF-PTM (1)	−0.61	+0.27	+1.84
TTF-py-PTM (2)	−0.62	+0.23	+1.46

Table S4. Calculated oxidation and reduction energies for **1** and **2** at (U)CAM-B3LYP/6-31+G* level with PCM model at (U)CAM-B3LYP/6-31G* optimized geometry. Energies of the optimized structures are reevaluated by additional single-point calculations using a basis set including polarization functions, crucial to describe anionic species.[S6] The calculated first oxidation (1Ox) and reduction (1Red) energies are determined as difference between optimized ground state energy and, respectively, optimized cation and anion energy; 2Ox is the difference between optimized dication and cation energy. Calculated potentials are reported vs Ag/AgCl electrode; to this aim, we subtracted to absolute red/ ox energies, relative potential of Ag/AgCl respect to NHE electrode (0.198 V) and absolute value of NHE (4.5 V).

TTF-PTM (1)

LUMO-β , -0.80 eV
LUMO-α , -0.88 eV

SUMO , -2.52 eV

HOMO.α, HOMO-β , -6.12 eV

SOMO, -7.44 eV

(HOMO-1)-β, -7.72 eV

(HOMO-2)-α -7.86 eV

(HOMO-1)-β, -8.43 eV
(HOMO-3)-α, -8.49 eV

(HOMO-3)-β, -8.53 eV

TTF-py-PTM (2)

LUMO-β, -0.81 eV
LUMO-α, -0.88 eV

SUMO, -2.51 eV

HOMO-α, HOMO-β, -6.11 eV

(HOMO-1)-α, -7.21 eV

(HOMO-1) -β, -7.33 eV

(HOMO-2)-α, (HOMO-2)-β, -7.35 eV

SOMO, -7.62 eV

(HOMO-3)- β , -8.09 eV

Energy (eV)

Energy (eV)
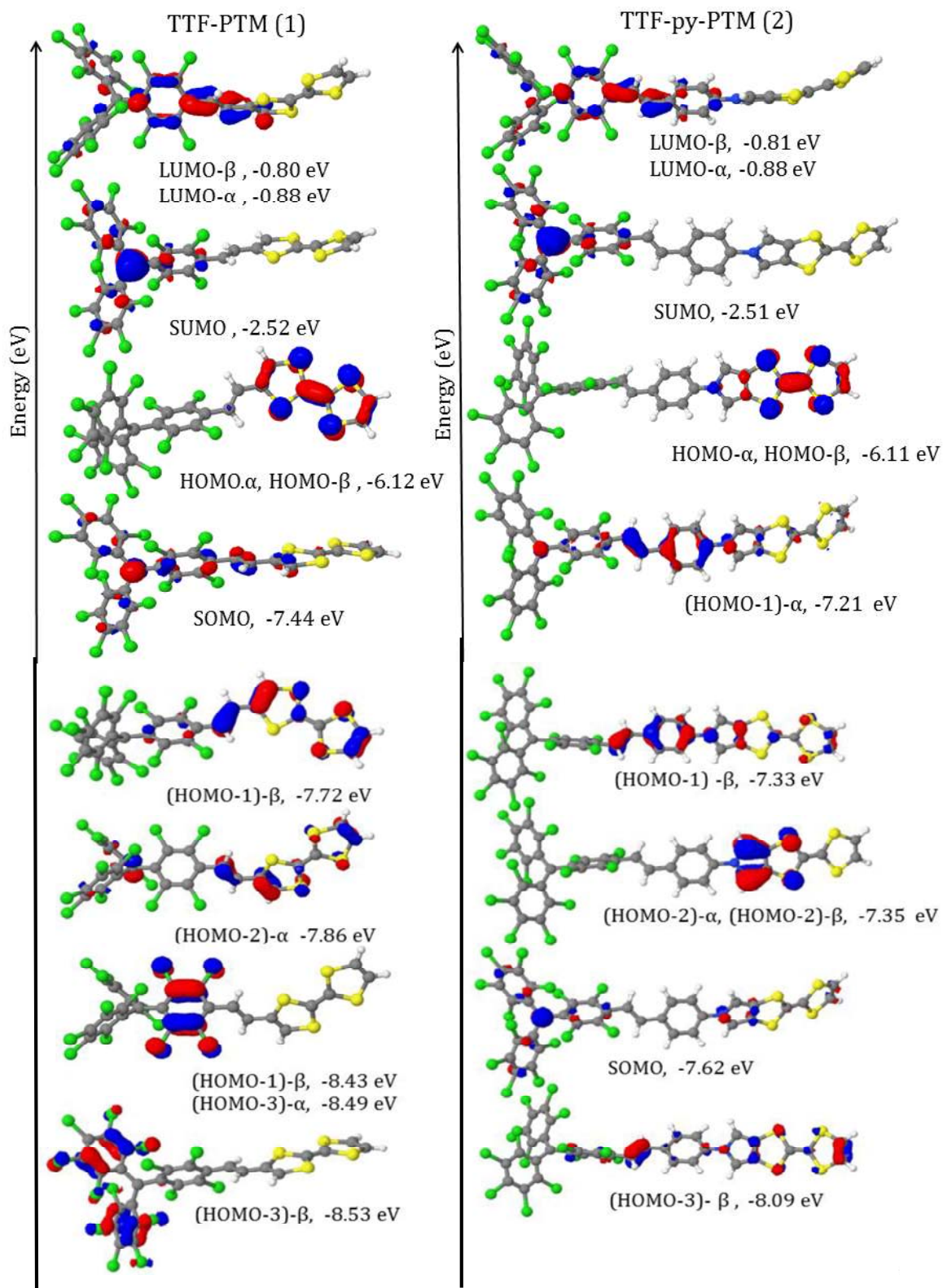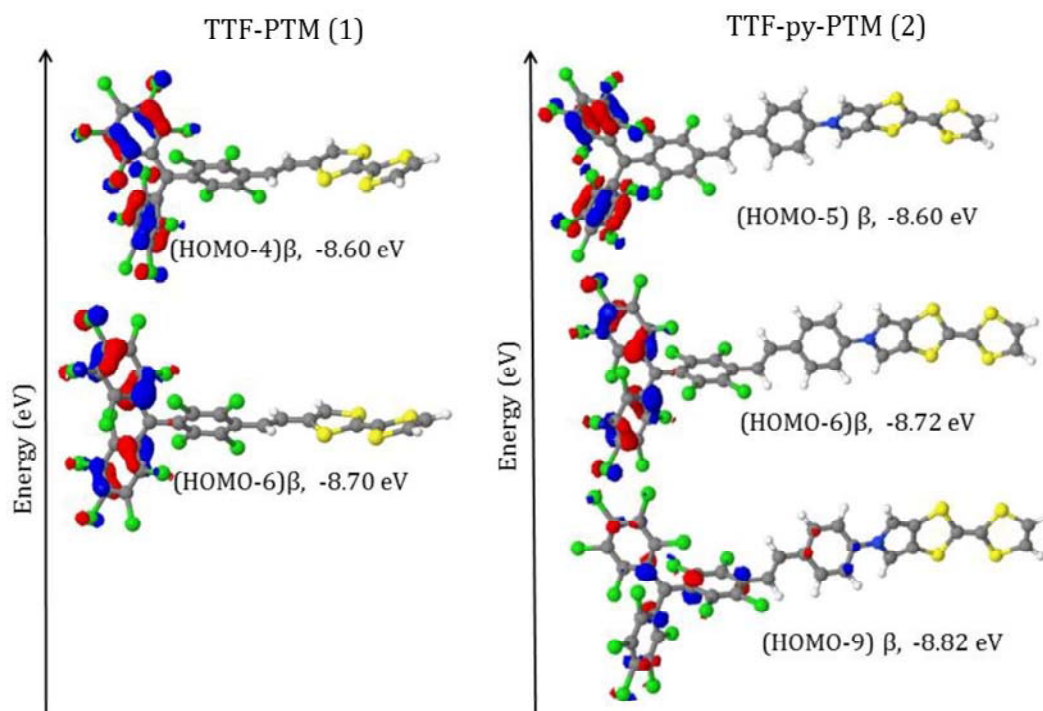
Figure S19. Selected frontier orbitals of **1** and **2** calculated at UCAM-B3LYP/6-31G* in CH_2Cl_2 (PCM model) at optimized ground state.

TD-UB3LYP/6-31G* with PCM model			
	λ(nm)	oscillator strength	transition nature
1	380	0.151	SOMO→(LUMO+1)α (0.50) (HOMO-6)β → SUMO (0.10)
	403	0.123	SOMO →LUMO-β (0.25) (HOMO-6)-β→ SUMO (0.08) HOMO-α→(LUMO+5)α (0.10) HOMO-α→(LUMO+4)α (0.08)
	529	0.166	HOMO-α→LUMO-α (0.42) HOMO-β→LUMO-β (0.56)
	582	0.106	(HOMO-1)β → SUMO (0.69) HOMO-α→LUMO-α (0.12)
	652	0.002	HOMOα→LUMOα (0.33) HOMOα→LUMOα (0.21) (HOMO-1)β → SUMO (0.18)
	1468	0.061	HOMO-β →SUMO (0.98)
2	379	0.274	SOMO→LUMO-α (0.38) (HOMO-2)β→LUMO-β (0.10) (HOMO-1)α→LUMO-α (0.10) HOMO-α→(LUMO+3)-α (0.20)
	381	0.157	(HOMO-1)α→(LUMO+3)α (0.29) SOMO→(LUMO+3)α (0.24) (HOMO-7)-β→SUMO (0.20)
	382	0.069	HOMO-β→(LUMO+3)β (0.50) HOMO-α→(LUMO+4)α (0.38)
	386	0.117	HOMO-α→(LUMO+3)α (0.67) HOMO-β→ (LUMO+3)β (0.09) HOMO-β→ (LUMO+4)β (0.08) (HOMO-1)α→LUMO-α (0.08)
	391	0.035	HOMO-α→(LUMO+3)α (0.14) HOMO-α→(LUMO+4)α (0.18)
	449	0.067	(HOMO-1)α→LUMO-α (0.20) HOMO-α→LUMO-α (0.12) (HOMO-2)β→ LUMO-β (0.12) HOMO-β→ LUMO-β (0.12)
	474	0.028	(HOMO-7)β→SUMO (0.52) (HOMO-6)β→ SUMO (0.26)
	486	0.184	HOMO-β→LUMO-β (0.66) HOMO-α→LUMO-α (0.30)
	497	0.04	(HOMO-9)β→SUMO (0.14) HOMO-α→LUMO-α (0.14) (HOMO-3)β→SUMO (0.50)
	518	0.031	HOMO-β→LUMO-β (0.18) HOMO-α→LUMO-α (0.42) (HOMO-1)α→LUMO-α (0.10)
	646	0.116	(HOMO-2)-β→SUMO (0.88)
	1350	0.027	HOMO-β →SUMO (0.98)

Table S5. Lowest and most intense optical transitions calculated for dyads **1** and **2** in CH_2Cl_2 at TD-UB3LYP/6-31G* level.
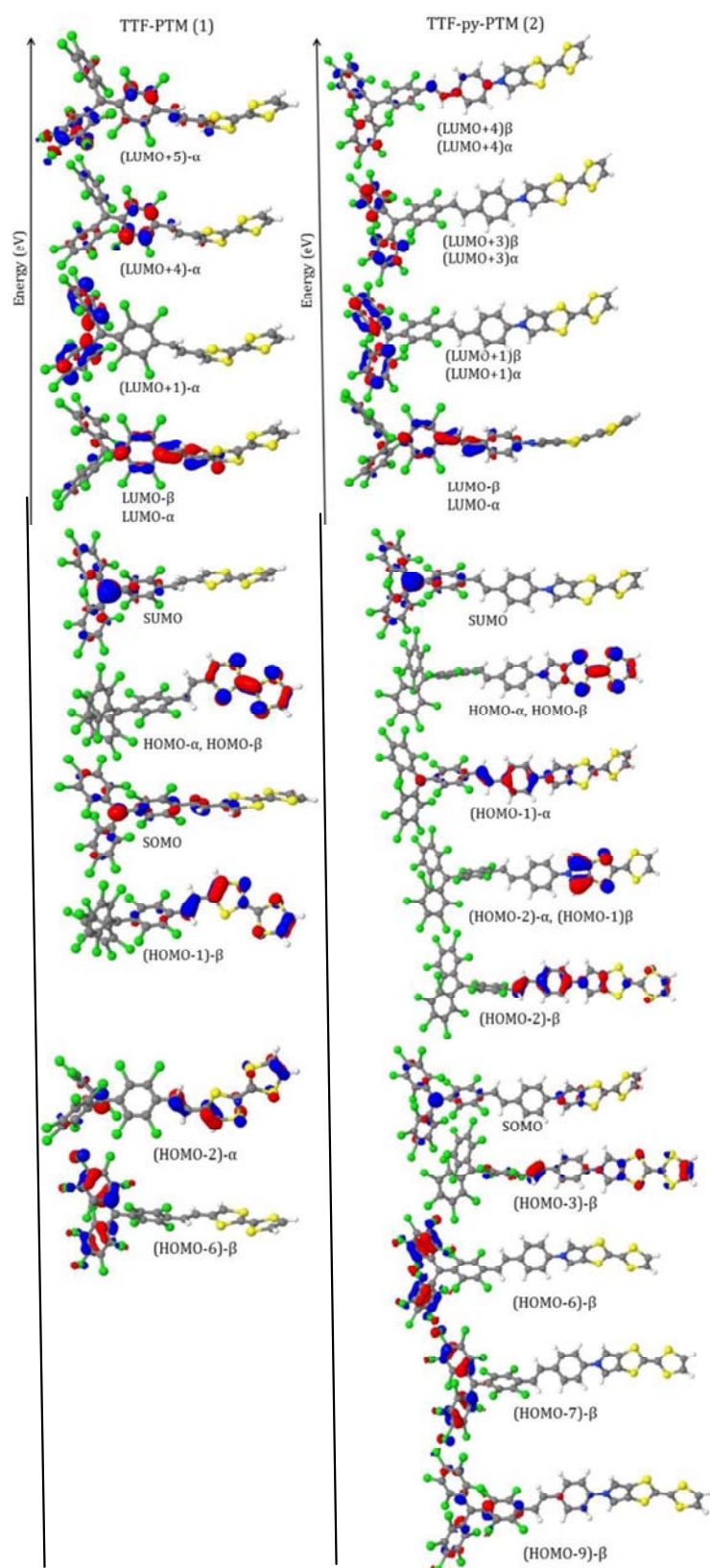
Figure S20. Selected frontier orbitals of **1** and **2** involved in excited state (Table S5) at UB3LYP/6-31G* in CH$_2$Cl$_2$ (PCM model).

Mulliken charge distribution		
Compound	Donor	Acceptor
2A_300K	0.093	-0.093
2A_150K	0.079	-0.079
2B_300K	0.085	-0.085
2B_150K	0.110	-0.110

Spin density distribution		
Compound	Donor	Acceptor
2A_300K	0.0531	0.9469
2A_150K	0.0622	0.9378
2B_300K	0.0549	0.9451
2B_150K	0.0899	0.9101

Table S6. Mulliken atomic charge and spin density distributions calculated at the UCAMB3LYP/6-31G* level for isolated **2** molecule at the crystallographic geometries A and B, at 300 and 150 K with (Pop=MBS) keyword.[S5].

References and footnotes of Supplementary Information

Compound 9 was prepared and purified by the same procedures described in the literature.[S1] All reactions requiring anhydrous conditions were conducted under argon atmosphere.

Compound 3 was purchased by Sigma-Aldrich and used without any further purification. Otherwise synthesis of this compound was described by Takimiya and co-workers.[S2]

Compound 1 was prepared and purified by the same procedures described in the literature.[S4]

For the synthesis of compounds 5 and **6** improved yields in both cases from 60 and 71% stated in the article to 71% for the triethylphosphite coupling and 90 % in the detosylation step were obtained.

S1 Rovira, C.; Ruiz-Molina, D.; Elsner, O.; Vidal-Gancedo, J.;Bonvoisin, J.; J.-P. Launay, J.-P.; Veciana, J. *Chem. Eur. J.* **2001**, *7*, 240-250.

S2 Takimiya, K.; Morikami, A.; Otsubo, T. *Synlett.* **1997**, *3*, 319-321.

S3 Nygaard, S.; Hansen, C. N.; Jeppesen, J. O. *J. Org. Chem.* **2007**, *72*, 1617-1626.

S4 Guasch, J.; Grisanti, L.; Lloveras, V.; Vidal-Gancedo, J.; Souto, M.; Morales, D. C.; Vilaseca, M.; Sissa, A.; Painelli, A.; Ratera, I.; Rovira, C.; Veciana, J *Angew. Chem. Int. Ed.* **2012**, *51*, 11024-11028.

S5 Montgomery J. A.; Frish M. J.; Ochtersky J. W; Petersson, G. A. *J. Chem. Phys*. **1999**, *110*, 2822-2827

S6 Mu-Hyun, B.; Friesner, R.A. *J. Phys. Chem. A*, **2002**, 106, 7407-7412.

Publication #5

Title: Pressure-Induced Conductivity in a Neutral Non-Planar Spin-
Localized Radical

Authors: Manuel Souto, HengBo Cui, Miriam Peña-Álvarez, Valentín G.
Baonza, Harald O. Jeschke, Milan Tomic, Roser Valentí, Davide
Blasi, Imma Ratera, Concepció Rovira, Jaume Veciana

Publication: *J. Am. Chem. Soc.,* 2016, *Just Accepted*

Pressure-Induced Conductivity in a Neutral Non-Planar Spin-Localized Radical

Manuel Souto,[†] HengBo Cui,[‡] Miriam Peña-Álvarez,[¶] Valentín G. Baonza,[¶] Harald O. Jeschke,[§] Milan Tomic,[§] Roser Valentí,[§] Davide Blasi,[†] Imma Ratera,[†] Concepció Rovira,[†] and Jaume Veciana*,[†]

[†]Institut de Ciència de Materials de Barcelona (ICMAB-CSIC)/CIBER-BBN, Campus Universitari de Bellaterra, 08193 Cerdanyola del Vallès (Barcelona), Spain

[‡]Condensed Molecular Materials Laboratory, RIKEN, Wako-shi, Saitama 351-0198, Japan

[¶]MALTA CONSOLIDER Team, Departamento de Química Física I, Facultad de Ciencias Químicas, Universidad Complutense de Madrid, 28040-Madrid, Madrid, Spain

[§]Institut für Theoretische Physik, Goethe-Universität Frankfurt, Max-von-Laue-Straße 1, 60438 Frankfurt am Main

ABSTRACT: There is a growing interest in the development of single-component molecular conductors based on neutral organic radicals that are mainly formed by delocalized planar radicals, such as phenalenyl or thiazolyl radicals. However, there are no examples of systems based on non-planar and spin-localized C-centered radicals exhibiting electrical conductivity due to their large Coulomb energy (U) repulsion and narrow electronic bandwidth (W) that give rise to a Mott insulator behavior. Here we present a new type of non-planar neutral radical conductor attained by linking a tetrathiafulvalene (TTF) donor unit to a neutral polychlorotriphenylmethyl radical (PTM) with the important feature that the TTF unit enhances the overlap between the radical molecules as a consequence of short intermolecular S···S interactions. This system becomes semiconducting upon the application of high pressure thanks to increased electronic bandwidth and charge reorganization opening the way to develop a new family of neutral radical conductors.

Introduction

In the last decades, there has been a huge development of molecular conducting materials based on two components, one of which is a π-extended organic acceptor (or donor) molecule. Such a compositional characteristic is motivated by the need to generate charge carriers in the solid material which is achieved either by a charge transfer (CT) between the donor and acceptor components, if both are present, or by a partial doping of such π-extended molecules with an extrinsic redox agent. These systems should have an additional prerequisite for exhibiting electrical conductivity, namely an appropriate packing of the doped molecules that permits the overlap between the frontier orbitals of neighboring molecules along one, two, or even three dimensions of the material.[1-3] More recently, single-component molecular conductors have been developed based on planar metal bis-dithiolene complexes which exhibit structural and electronic characteristics that combine the presence of charge carriers and a proper molecular packing.[4,5] The soft nature of all these molecular crystals permits to tune their electronic properties by applying pressure which allows to switch from a semiconductor material to a metal or even a superconductor.[6-7]

In view of the importance of obtaining crystals of single-component molecular conductors, the use of neutral organic radicals as building blocks for molecular conductors has appeared as alternative due to the possibility that the unpaired electrons can serve as charge carriers without the need of a previous doping process.[8] Phenalenyl-based radicals, developed by Haddon,[9–17] and thiazolyl-based radicals, by Oakley,[18-22] are good examples of such materials. The solid state electronic structure of this kind of crystals is best described in terms of the half-filled band (f = 1/2) Mott-Hubbard model, with one electron associated with each radical site. One of the keys to attain conductivity in these single-component radical-based materials and overcome the charge repulsion problem is to maximize the electronic bandwidth W ($= 4\beta$) and minimize the intra-site Coulomb repulsion energy U. When the electronic bandwidth is sufficient to offset charge repulsion ($W > U$), conductivity would take place.[20] Synthetic strategies to produce conductive radical-based materials have focused on the use of highly delocalized planar organic systems, which have the benefit of a low value of U, and the incorporation of heavy (soft) heteroatoms in these structures, which can lead to an enhanced bandwidth W.[21] However, there are no reported examples of single-component molecular conductors based on non-planar and spin-localized carbon-centered organic radicals due to their weak electronic intermolecular interactions leading to narrow electronic bandwidth and their large intra-site electronic repulsion. Finding new ways to overcome this shortage could expand the possibilities to generate novel single-component molecular conductors.

Organic molecules containing electron donor (D) and electron acceptor (A) units linked by π-conjugated bridging groups are worthy of attention for the investigation of intramolecular electron transfer phenomena and its associated bistability event.[23] Recently, we have reported a D-A dyad based on a tetrathiafulvalene (TTF), an electron π-donor, connected to a polychlorotriphenylmethyl (PTM) radical, a good electron acceptor, which exhibits bistability in solution through the application of external stimuli such as the polarity of the solvent or temperature.[24-26] Indeed, molecules of this D-A dyad coexist in two electronic structures, one neutral and another zwitterionic, due to the intramolecular charge transfer process between the D and A subunits. Therefore, such a kind of radical D-A dyads are promising candidates to show novel physics when moving from solution to solid state if one takes advantage of the intramolecular CT to generate a doping in the subunits. In order to exploit the physical properties in solid state such as conductivity and magnetism of this kind of species, we have recently obtained the radical donor-acceptor dyad 1 (MPTTF-PTM), based on a PTM radical unit linked to a monopyrrolotetrathiafulvalene (MPTTF) unit through a π-conjugated phenyl-vinylene bridge (Figure 1). The bridge was added in order to decrease the steric repulsion between the PTM radical units and to take advantage of the TTF subunit to pack forming chains. Indeed, this system shows a supramolecular architecture with segregated donor and acceptor units where the TTF units are arranged forming herringbone-type 1-D chains and a close packing of the PTM units.[27]
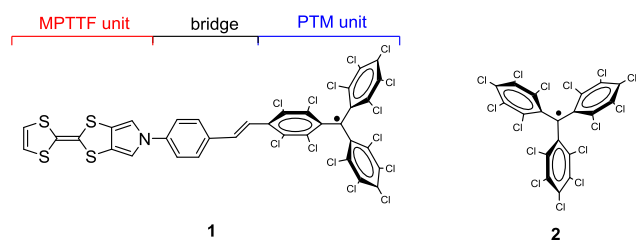
Figure 1. Chemical structures of the neutral radical dyad MPTTF-PTM (**1**) and perchlorotriphenylmethyl (PTM) radical (**2**).

In this work and in accordance with the intrinsic softness of molecular crystals we report the appearance of conductivity in single crystals of radical dyad **1** induced by pressure in contrast to the Mott insulator behavior of the unsubstituted perchlorotriphenylmethyl radical **2** under all applied pressures. Thus, the conductivity in **1** with pressure is related to the enhancement of the intermolecular overlap between the MPTTF-PTM molecules due to incorporation of TTF units. This forces the formation of closed packed stacks of molecules and, thus, the increase of W. Band structure calculations based on density functional theory (DFT) on ab initio-predicted MPTTF-PTM crystal structures under pressure confirm the significant increase of W in radical dyad **1** as a function of pressure. These calculations suggest important modifications on the electronic structure at pressures above 6-8 GPa with an increase in charge delocalization and of the W/U ratio. These effects are clearly observed in our combined analysis of Raman and DFT calculations under pressure. Moreover, high-pressure Raman and photoluminescence spectroscopy show important conformational changes that could indicate a change of the crystalline phase when the system is compressed at very high pressures. Up to our knowledge, this is the first example of a single-component molecular conductor based on a non-planar and C-centered neutral radical with highly localized spins that exhibits a semiconductor behavior with high conductivity and low activation energy.

Results

Crystallography. X-ray diffraction analysis on red crystals of radical **2**, obtained by a slow diffusion in a mixture of dichloromethane/hexane (1:1) at room temperature, reveals a new polymorph of PTM that crystallizes in the triclinic system with a $P\bar{1}$ space group and the asymmetric unit is formed by two equivalent molecules (Table S1 and Figure S1 in the Supporting Information). Molecules of **2** are arranged on the *ab* plane as shown in Figure 2 forming regular chains of radicals connected by short Cl···Cl contacts. The distance between the central *ipso*-C (C_1) atoms of two adjacent molecules of PTM radical is 13 Å along the *b*-axis. Moreover, molecules are disposed on the *bc* plane as shown in Figure S2 showing the formation of dimers with a short contact between the phenyl rings (4.3 Å) that are oriented in a parallel position showing a distance between their central *ipso*-carbon (C_1) atoms of 10 Å.
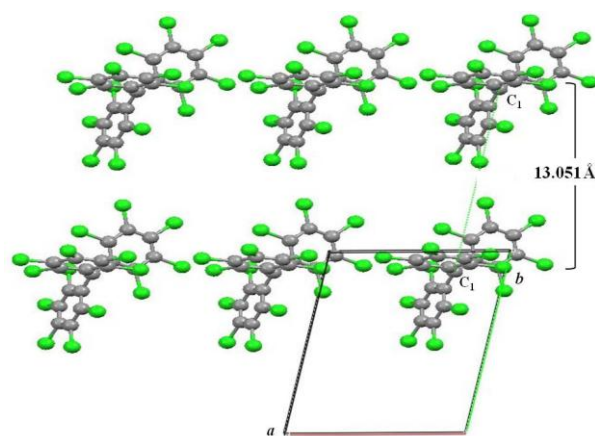
Figure 2. Crystal packing of radical **2** on the *ab* plane. The grey and green ellipsoids represent the carbon and chlorine atoms, respectively. Atoms are shown at the 50% probability level. Intermolecular distance between the central *ipso*-carbons of two adjacent molecules in the *ab* plane (C1···C1 ') is 13 Å.

On the other hand, dark crystals of radical dyad **1** were also obtained by a slow evaporation in dichloromethane/hexane at room temperature and their X-ray diffraction analysis shows a $P2_1$ space group with Z = 4 (Table S1 and Figure S3).[27] The asymmetric unit shows two inequivalent molecules that are chemically equivalent and exhibit a very similar geometry. Regarding the molecular arrangement, molecules of radical dyad **1** are stacked forming regular 1D chains on the *ab* plane in which MPTTF units are forming a herringbone structure along the *b*-axis with short S···S and Cl···Cl distances of 3.9 and 3.3 Å, respectively (Figure 3). Along this axis direction, the distance between the central *ipso*-carbon (C_1) atoms of the PTM subunit of two adjacent molecules is 7.9 Å and the planes formed by the phenyl rings of the PTM units of adjacent molecules are also oriented in a parallel fashion indicating the formation of π-type interactions between the neighboring radicals units (Figure S4). Thus, the decrease of intermolecular distances between the molecular units clearly denotes a higher overlap of PTM radical units in dyad **1** in comparison with radical **2** thanks to the supramolecular self-assembly of the TTF units.
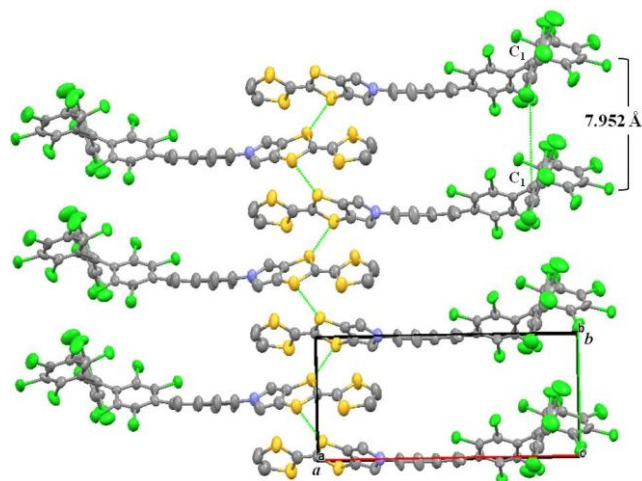
Figure 3. Crystal packing of radical dyad **1** on the *ab* plane showing the intermolecular distance between the central $C(1)\cdots C(1)'$ atoms (7.9 Å) of adjacent PTM molecules and short $S\cdots S$ interactions. The grey, green, blue and yellow ellipsoids represent the carbon, chlorine, nitrogen and sulfur atoms, respectively. Atoms are shown at the 50% probability level. Hydrogen atoms have been omitted for clarity.

High-pressure conductivity. Resistivity measurements on crystals of **1** and **2** were performed under high pressure conditions. Three independent crystals of radical **2** were measured up to 21.2 GPa and they were found always insulating under all assayed conditions. Pressure and temperature dependence measurements of the resistivity of radical dyad **1** were also performed with three independent crystals along the *b*-axis (Figures 4, S7 and S8). Crystals of **1** showed insulating behavior at ambient pressure while increasing the pressure the room-temperature resistivity rapidly decreased exhibiting a semiconducting behavior throughout the studied temperature range. From 6.5 GPa the room-temperature resistivity linearly decreased with a negative slope of *ca.* $10^{0.38}$ Ω cm / GPa and the conductivity at 15.2 GPa and 298 K was found to be as high as 0.76 S cm^{-1} with a low activation energy (E_a) of 0.067 eV (E_a = 0.21 eV at P = 6.5 GPa). At higher pressures the room temperature conductivity slightly decreased on increasing the pressure (see Figures S7 and S8) and the conductivity at 21.2 GPa (298 K) was 0.43 S cm^{-1} with and activation energy E_a of 0.073 eV. Reproducibility of measurements was confirmed using three different samples as shown in Figure S8.
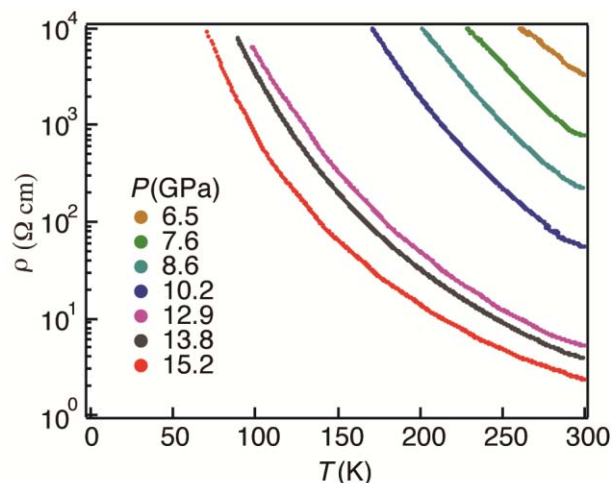
Figure 4. Electrical resistivity of radical dyad **1**. Temperature dependence of the resistivity of radical dyad **1** along the *b*-axis at different pressures.

Magnetic susceptibility. The temperature dependence of the magnetic susceptibility (χ) for a polycrystalline sample at ambient pressure of radical dyad **1** was measured over the temperature range of 2-300 K (Figure S10). The compound shows a Curie-Weiss behavior and the experimental data was fitted to obtain a Curie constant C = 0.394 cm^3 K mol^{-1} with a $\chi_m T$ at room temperature that fully agrees with the theoretical value of 0.375 expected for non-interacting S = ½ systems. Upon cooling, $\chi_m T$ decreases according with the presence of weak antiferromagnetic interactions among the radical units (Weiss constant of θ = -1.06 K).

Electrochemical properties. The electrochemistry of radicals **1** and **2** were examined by cyclic voltammetry (Figure S11) in order to have an estimation of the disproportionation potential (E_{disp}) in solution. This value can be determined from the difference between the first oxidation and reduction potentials in solution $\Delta E_{2-1} = (E_2^{1/2} - E_1^{1/2})$ and provide indirect measurements of the intra-site Coulomb repulsion energy, U, which are usually low in highly delocalized spin systems.[17] E_1 electrochemical potential corresponds to the reduction of the radical to the anion and E_2 is attributed to the first oxidation process of the molecule. In the case of radical dyad **1**, the first oxidation process is attributed to the oxidation of the electroactive TTF unit. Thus, the estimated disproportionation potentials for **1** and **2** are 0.64 and 1.80 V, respectively, confirming that the Coulomb repulsion energy is much lower for radical dyad **1** that is indicative of a higher charge delocalization.

Table 1. **Electrochemical data of radicals 1 and 2.**

Compound	$E^{red}_{1/2}$	$E^{ox1}_{1/2}$	$E^{ox2}_{1/2}$	$E^{ox3}_{1/2}$	E_{disp}^{b}
1	-0.19	0.45	0.95	1.52	0.64
	(PTM)	(TTF)	(TTF)	(PTM)	
2	-0.19	1.61	-	-	1.80
	(PTM)	(PTM)			

[a]In Volts vs Ag/AgCl; CH$_2$Cl$_2$ as solvent and TBAPF$_6$ as electrolyte and scan rate of 0.1 V/s. [b]E_{disp} estimated as $E^{ox1}_{1/2}$- $E^{red}_{1/2}$.

Crystal structures, band structure and charge transfer calculations as a function of pressure. In order to elucidate the microscopic origin of electrical conductivity pressure dependence in radical dyad **1** and due to the absence of good quality powder X-ray diffraction data for crystal structure determination at finite pressures we decided to calculate by *ab initio* optimization routines the crystalline and electronic band structures at the studied pressures.

Thus, we relaxed a set of crystal structures at different pressures within density functional theory (DFT) using the projector augmented wave basis as implemented in the Vienna *ab* initio simulation package (VASP)[28-29] and the generalized gradient approximation (GGA)[30] (see Methods section and Supplementary Information for details). The electronic structure and charge transfer of this series of predicted crystal structures were determined with the full potential local orbital (FPLO) basis set.[31] Figure 5 shows the evolution of lattice parameters, monoclinic angle and volume of the predicted structures as a function of pressure. While along the *a* and *b* directions the structures experience a monotonic contraction, this is not the case along the *c* direction (perpendicular to the molecular stacking) where a slight expansion at low pressures followed by a contraction at higher pressures is observed. The decrease of the monoclinic angle indicates a reduction of the structural anisotropy and we observe an enhanced planarity of the molecules at high pressures. Further below we show that our Raman analysis at high pressures is consistent with the predicted structures.
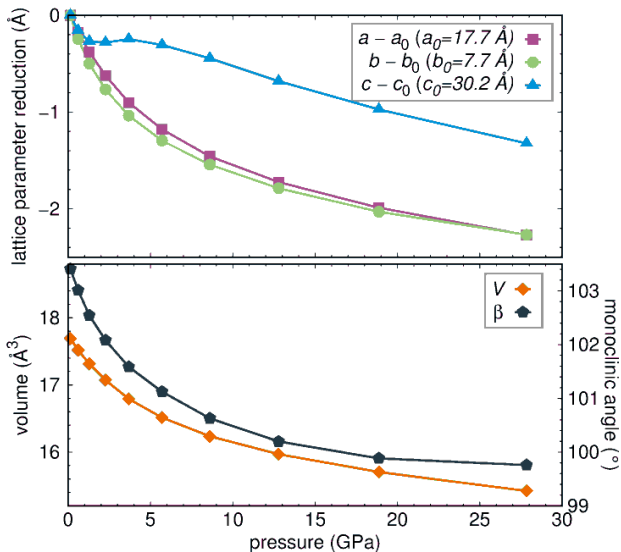
Figure 5. Crystal structure parameters at high pressure. Evolution of lattice parameters, monoclinic angle and volume of the predicted structures of radical dyad **1** as a function of pressure.

We analyze in what follows the electronic structure of radical dyad **1** under pressure. Figure 6 shows the GGA electronic bandstructure of the ambient pressure (P=0) and the P=8.6 GPa structures. At P=0 the system is a Mott insulator, however as it is well known[32] DFT in the GGA approximation is not able to reproduce this insulating state (Figure 6a) due to the insufficient treatment of electronic correlations in GGA. Albeit the absence of a gap at P=0, we can still extract valuable information out of the GGA calculations. There are four half-filled narrow bands at the Fermi level arising from the four molecules per unit cell of **1** (Figure 6a). PTM+bridge is con-

tributing the majority of the carriers in the valence band with some participation of MPTTF. At higher binding energies the bands are mostly of MPTTF character with some hybridization to the PTM+bridge. The lack of dispersion along kz indicates that this system is electronically dominantly two-dimensional at ambient pressure. Upon increasing pressure (Figure 6b and S14) the bandwidth W significantly increases due to enhanced intermolecular overlap and hybridizations and the system becomes more three dimensional. This increase in W and molecular hybridizations contributes to the increase of the ratio W/U and the appearance of enhanced conductivity at high pressures as observed in our measurements. At 0 GPa the bandwidth of all four bands at the Fermi level is very narrow (<0.04 eV). However, with pressurization at 8.6 GPa, we observe that the gap in the valence states at -0.05 eV between the bands dominated by TTF orbitals and the bands dominated by PTM orbitals disappears and a wide band manifold of about 0.4 eV forms which is of the same magnitude as the Coulomb barrier estimated from the electrochemical data in solution. Further compression to 18.9 GPa gives rise to a higher broadening of the bands with bandwidth near 0.8 eV.

Wannier functions at ambient pressure and P = 12.8 GPa are shown in Figures S15 and S16 for visualizing the orbitals corresponding to the bands with dominant PTM character at the Fermi level (EF) and the bands with dominant MPTTF character right below EF. Under high pressure (Fig. S15), the Wannier functions acquire tails on neighboring molecules; i.e. tails on PTM in the case of the SUMO, and on neighboring MPTTF and the bridge in the case of the HOMO (dark blue patches result from cuts due to unit cell boundaries).
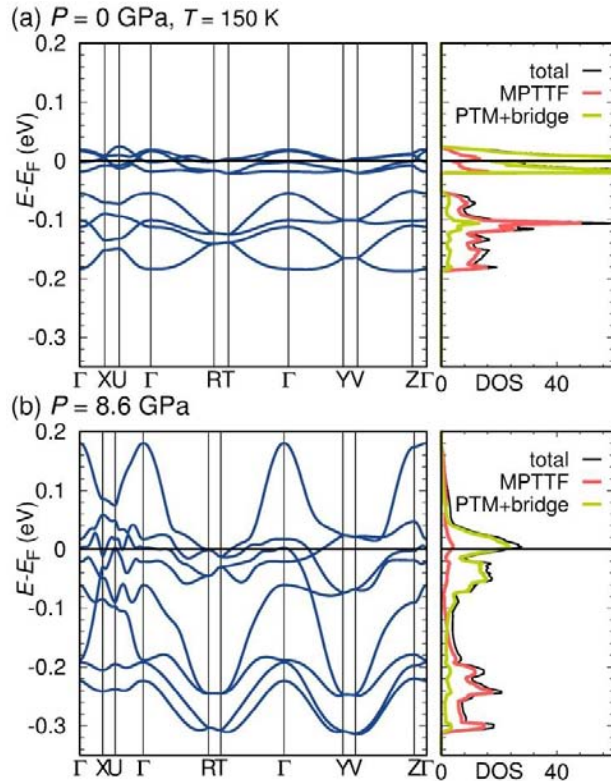

Figure 6. Electronic band structures and density of states of radical dyad **1.** The two-dimensional energy dispersion near the Fermi level at (a) ambient pressure (P=0) and (b) P=8.6 GPa. Path in the Brillouin Zone: X=(1/2,0,0), U=(1/2,0,1/2), R=(1/2,1/2,1/2), T=(1/2,1/2,0), Y=(0,1/2,0), V=(0,1/2,1/2) and Z=(0,0,1/2).

To better understand this magnetic system, we have also performed spin-polarized GGA calculations. Figure 7a shows the spin distribution in the radical dyad **1** at P=0 GPa. We observe a strong spin localization on the central C atom of the PTM units and a less pronounced spin occupation on the MPTTF units. Pressure only slightly influences the spin density distribution between the two components of the molecule as it can be seen from the evolution of the magnetic moment and spin density with pressure (Figures S28 and S29). The spin polarized bands show a gap at P=0 GPa (Figure 7b) that diminishes and closes at P > 6 GPa (Figure 7c). Even though we don't have an advanced description of correlations as mentioned above, with the incorporation of magnetism we can track the evolution under pressure of the insulating to semiconducting/metallic behavior associated to magnetism. We observe a closing of the gap between the (spin-polarized) occupied bands with dominant MPTTF character and the empty bands with dominant PTM character. An improved description of correlations -which is beyond the scope of the present study- would shift the closing of the gap to higher pressures as observed experimentally.

The pressure evolution of the charge transfer in the radical dyad **1** is displayed in Figure 8. We chose to distinguish the PTM together with the phenyl-vinylene bridge as the acceptor unit and the MPTTF as donor unit (Figure 8a). We observe (Figure 8b) that increasing the pressure, the charge transfer between the two units increases from $0.09e-$ at ambient pressure to $0.32e-$ at P = 18 GPa. In order to analyze the pressure dependence of the charge distribution in the PTM+bridge region, we plot in Figure 8c the excess charge on PTM and bridge units. We find that increasing the pressure, the PTM unit decreases in excess of charge indicating a possible electron delocalization through the bridge that is in agreement with the enhanced planarity of the system observed in the simulated crystal structures at high pressures. The charge on the donor MPTTF unit increases from $0.09e-$ at ambient pressure to $0.25e-$ at P = 10 Gpa (Figure 8b). Meanwhile, the bridge which is only donating $0.03e-$ at ambient pressure turns into an acceptor with $0.32e-$ extra electrons at P = 10 GPa. This indicates that there is a charge reorganization happening at P = 6-8 GPa between PTM and the bridge. Grey lines show the very small excess charge evolution under pressure for the two inequivalent molecules in the unit cell. These latter results indicate a slight tendency towards molecular charge order in the crystal.
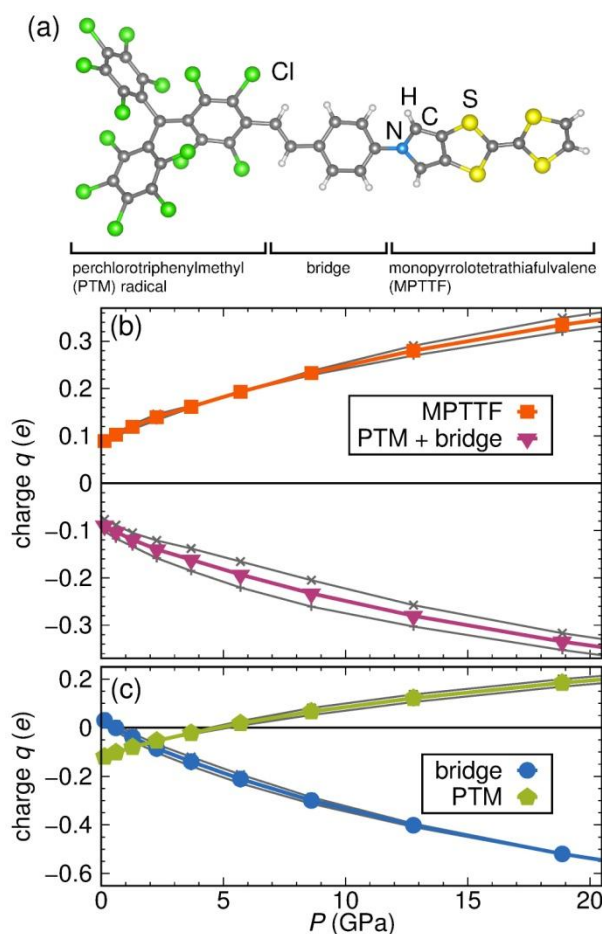

Figure 7. a) Spin distribution in radical dyad **1** at 0 GPa. Spin polarized electronic band structures and density of states of radical dyad **1** at b) 0 GPa and c) 8.6 GPa.

Figure 8. Calculated evolution of excess charge within the units of radical dyad **1** with hydrostatic pressure. (a) The different selected parts of the radical dyad **1**. (b) Excess of charge on the different units under high pressure. (c) Excess of charge on the PTM and bridge units under high pressure. The grey lines denote the excess charge corresponding to the two non-equivalent molecules of **1** under pressure.

In order to further verify that the here predicted crystal structures provide a realistic account of the radical dyad **1** under pressure, we compare high pressure Raman spectroscopy with spectra obtained from density functional theory calculations on these structures. The predicted crystalline structures, obtained with the above described calculations, that show an increase of electronic bandwidths and the charge reorganization of dyad **1** under pressure provides a plausible explanation of the semiconducting behavior under the application of high pressure. However a definitive confirmation of such crystalline structures by high-pressure XRD data is still pending.

High-pressure Raman spectroscopy. The Raman spectra of radical dyad **1** at different pressures were obtained using an excitation wavelength of 532 nm. This study has been complemented by calculation of the spectrum at different pressures based on the density functional theory (DFT) using a Gaussian basis set at the UM06/6-31G(d,p) level.[33,34] The spectra have been calculated for a single molecule whose structure has been extracted from the VASP optimized crystal structures at various pressures in the previous section. This facilitates the Raman analysis by a detailed computational study on the assignment of the bands (See Figures S17-S19). In the 1700-1450 cm^{-1} region, the bands at 1619 and 1597 cm^{-1} are attributed to the C=C stretching modes of the benzene and vinylene units of the bridge whereas the bands in the 1515-1480 cm^{-1} region are mainly due to the C=C stretching of TTF and PTM moieties. The Raman spectra at selected pressures were recorded and their intensity was normalized with the band at 1515 cm^{-1} (C=C stretching of TTF) (Figure S20a). On increasing the pressure, we observed that the Raman bands related to the bridge around 1600 cm^{-1} progressively decreased in intensity. On the contrary, the bands assigned to the TTF and PTM units increased in intensity and overlapped when a high-pressure was applied (Figure S20a). This tendency was also observed for the simulated Raman spectra obtained for the VASP predicted crystal structures at each applied pressure, confirming herewith the same behavior (Figure S20b). Moreover, the overlapping of the bands related to the TTF and PTM units suggests a change of the electronic delocalization on the molecule that could be related to the enhanced planarity of the molecules observed in the simulated crystal structures at high-pressures. On the other hand, in the region around 800 cm^{-1}, the bands attributed to the *out-of-plane* C-H bending broadened and decreased in intensity when increasing the pressure due to the fact that these vibrations were hindered because of the molecular packing.

We have performed a detailed analysis of the relative intensity variation of the measured Raman bands attributed to the vinylene bridge and those related to the PTM and TTF moieties along the entire pressure range to analyze possible phase transitions (Figure 9). We refer to the intensities as the areas of Raman bands, calculating the sum of the areas of the bands at 1619 and 1597 cm^{-1} for the vinylene bridge, the bands at 1570 and 1515 cm^{-1} for the TTF and the bands at 1500 and 1486 cm^{-1} for the PTM unit. We have calculated and plotted the intensity ratio for (*a*) the TTF stretching bands/vinylene bands, (*b*) the PTM stretching bands/vinylene bands, and (*c*) TTF+PTM bands/vinylene bands. A linear fit of the data shows two regions at pressures below and above 8 GPa with different slopes, being the slope steeper at P > 8 GPa. These results suggest that while the system is reorganizing and readjusting the intermolecular spaces up to pressures of 8 GPa, the abrupt change of slope at 8 GPa indicates the presence of important intra- and intermolecular conformational changes that may originate from a crystalline phase transition. Please note that our theoretical structure prediction doesn't show a true crystalline phase transition but rather a redistribution of electronic charge at about this pressure which is an indication that some structural changes happened. The theoretical calculation may, for example, miss a structural phase transition because of the consideration of too small supercells for the relaxations. On the other hand, the evolution of these Raman bands is different from other PTM derivatives previously studied in our group[35] indicating a different electronic behavior for this system.
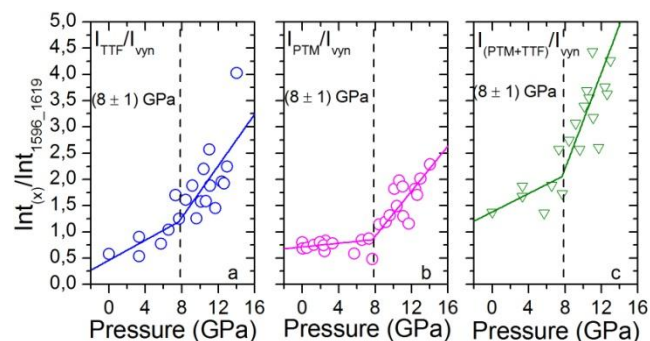

Figure 9. Intensity ratio of Raman bands of radical dyad **1** assigned to (a) C=C stretching of TTF/vinylene, (b) C=C stretching of PTM/vinylene bridge, and (c) C=C stretching of TTF+PTM/vinylene.

Apart from the changes in the relative intensities of the Raman bands, the most apparent effects of pressure on the Raman spectra are the upshifts of the spectral features with increasing pressure. This effect is analyzed in Figure S21 and Figure S22, where the frequencies of the most intense bands of PTM, vinylene bridge and TTF•PTM are plotted as a function of pressure. The observed shifts with pressure show a three regime stage where the different Raman bands shift with different slopes with increasing pressure. The three regimes would range from 0 to 2-5 GPa, from 2.5 to 8 GPa and, from 8 to 14 GPa (which is the highest pressure experimentally reached). The first regime is assigned to intermolecular rearrangements, since pressure barely induces any shifting of the bands. In the second one the bands show an important upshift with increasing pressure, indicating that pressure affects bonds and angles, which can be explained by conformational changes to readjust the electronic density. In the third regime, in general all analyzed bands show less steep slopes than in the intermediate regime but steeper than in the first regime. This indicates that pressures larger than 8 GPa must cause both intra- and intermolecular effects. These inter- and intramolecular pressure effects are confirmed by the reversibility observed in high pressure Raman experiments (Figure S23). Up to 1.6 GPa these changes are fully reversible whereas from 6 GPa there are slight deviations between the relative intensities even though the spectral pattern remains. Finally, the recovered sample after compression of about 14.5 GPa is totally different from the pristine one.

High-pressure photoluminescence measurements. In order to further investigate the intra- and intermolecular pressure effect observed by Raman spectroscopy, photoluminescence measurements of crystals of radical dyad **1** when the sample was monochromatically excited with λ = 532 nm at different pressures were performed (Figure 10). High pressure experiments were conducted in a sapphire anvil cell and spectra were recorded at selected pressures up to 12 GPa. Whereas the pristine sample at 0 GPa does not show well defined bands in the visible region, by increasing the pressure it is possible to observe the growth of a broad band in the 600-700 nm region (see Fig. 9 and S24). This band that appears centered at 680 nm (1.8 eV) is much more intense when increasing the pressure above 7 GPa as shown in Figure 10. The photophysical processes observed can be explained by the excitation of dyad **1** with light λ = 532 nm that induces 264α→266α (SOMO→LUMO) electronic transition (See Supporting Information) as it has been already observed in similar systems.[36] At ambient pressure this electronic transition is practically forbidden whereas by increasing the pressure the transition becomes more favored probably due to the enhanced electron delocalization and planarity of the system. Moreover, by increasing the pressure the intermolecular interactions become more important that could lead to an enhancement of the photoluminescence as it has been recently reported.[37,38] In order to analyze the reversibility of the photoluminescence properties at high pressure, we have measured the photoluminescence spectrum of the recovered sample at 6 and 12 GPa (Figure S26). In both cases the intensity of the band remains the same indicating that conformational changes are not reversible and could be originated from a crystalline transition phase.
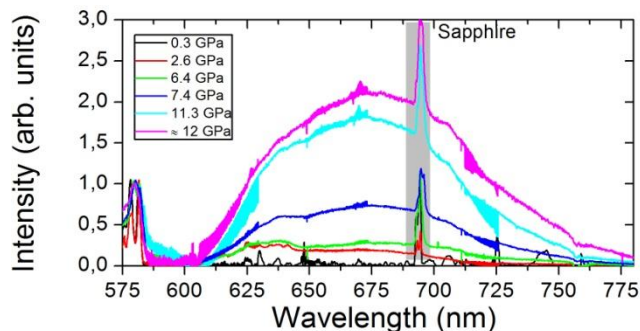
Figure 10. High resolution phtoluminescence spectra of crystals of radical dyad **1** at selected pressures when the sample was excited at 532 nm. The sample was supported on a non-drilled gold gasket and compressed using sapphire anvils with a 380 μm culet.

Discussion

Analyzing all the experimental and theoretical studies, we can assume that the conductivity in radical dyad **1** between neighboring molecules take place through the enhanced overlap between MPTTF and PTM under pressure. This overlap is absent in radical **2** which remains insulator at all considered pressures. When increasing the pressure, the electronic bandwidth W in radical dyad **1** increases until is able to offset the Coulomb repulsion U. In addition, simultaneous charge reorganization is happening that changes the charge on the radical subunits of dyad **1** molecule which are the units that contribute more to the electronic band (Fig. 8c). In fact, band structure calculations above 8 GPa show that the gap between the bands

dominated by TTF orbitals and the bands dominated by PTM orbitals disappear forming a wide band. Moreover, calculations of the evolution of charge transfer indicate that charge reorganization is taking place above the same applied pressures. On the other hand, high-pressure Raman spectroscopy supports this charge reorganization in a similar pressure regime and identical behavior was observed in the simulated spectra obtained for the VASP predicted crystal structures at each applied pressure. Reversibility studies on pressure-dependent Raman and photoluminescence measurements indicate that there is a change in the electronic conformation of the system in agreement with the enhanced planarity of the molecules and the intermolecular reorganization that could hint to a possible structural phase transition.

Summary and conclusions

In summary, we have reported the observation of induced-pressure conductivity in the non-planar and spin localized neutral radical dyad **1** that exhibits a semiconductor behavior with high conductivity and low activation energy upon application of high pressure. In contrast, the model radical **2** remains as a Mott insulator under all applied pressures. This different behavior is due by one hand to the supramolecular arrangement of molecules of **1** that permits to increase the bandwidth W and as a consequence the W/U ratio. Moreover, the reduction of the effective Coulomb interaction in **1** in comparison to **2** could be attributed to the enhanced electron delocalization in the system due to incorporation of a substituent donor unit, as confirmed by Raman experiments and theoretical calculations. Overall we believe that the results described here are a proof of concept of a novel strategy providing an important insight into the design of new radical-based conductors. Thus, it may be possible to engineer radicals which can be conducting even without the need for applied pressure.

Experimental section

Synthesis and characterization of radicals 1 and 2. The reagents and solvents used for synthesis and crystallization were of high purity grade (Sigma- Aldrich and SDS SA). Compounds **1** and compound **2** were prepared as previously reported in ref. 27 and 39, respectively. The electrochemical experiments were performed with a potentiostat- galvanostast 263a (EG&G Princeton Applied Research) using platinum wires as counterelectrode and working electrode, a silver wire as reference electrode and as electrolyte a 0.1 M solution of tetrabutylammonium hexafluorophosphate (TBAHFP) in acetonitrile.

Conductivity measurements. The four-probe resistivity measurements were performed with a Cryocooler helium compressor system (Sumitomo Heavy Industries, Ltd.). The KEITHLEY 224 Programmable current source and 182 Sensitive digital voltmeter were used for all measurements.

Raman and photoluminescence measurements. High pressure experiments were conducted in a sapphire anvil cell (SAC)[40,41] with a diameter culet of 360 μm and a gold gasket, specified in each section. No pressure transmitting medium was used and diamond chips were placed as the pressure calibrant. Raman and photoluminescence measurements were performed using an air-cooled argon ion laser, a Spectra-Physics solid state laser, operating at 532.0, nm. The device is

equipped with a 10x Mitutoyo long working distance objective coupled to a 10x Navitar zoom system and focused onto the slit of an ISA HR460 monochromator with a grating of 600 grooves mm^{-1} and a liquid nitrogen cooled CCD detector (ISA CCD3000, 1024−256 pixels). Spectra were measured with a spectral resolution of about 2−3 cm^{-1} and calibrated with a standard neon emission lamp. The SAC is mounted on a xyz stage, which allows us to move the sample with an accuracy of 1 μm. The typical sampling area was about 1−2 μm in diameter. The simulated Raman spectra were calculated using the UM06 density functional theory [33] in conjunction with the 6-31G** basis set.[34]

Theoretical calculations. Crystal structures at different pressures were simulated within density functional theory calculations[30] by performing relaxations of lattice parameters, monoclinic angle and internal atom positions at constant volume with the VASP code.[28-29] A plane wave cutoff of 400 eV was used as well as a 4x4x2 k-mesh in the Brillouin zone. We checked, by performing enthalpy calculations that constant volume relaxations were of higher quality than constant pressure relaxations (not shown). All presented bulk electronic structure calculations were performed with the FPLO code[31] where a k-mesh of 6x6x6 points was considered to converge the computations.

ASSOCIATED CONTENT

Supporting Information. Experimental details of X-ray crystallographic data and structure refinement. Simulated crystal structures of **1** at different pressures. Supplemental spectra of high-pressure conductivity, magnetic susceptibility, cyclic voltammetry, Raman and photoluminescence experiments. Simulated Raman spectra and details of theoretical calculations. This material is available free of charge via the Internet at http://pubs.acs.org.

AUTHOR INFORMATION

Corresponding Author

* E-mail: vecianaj@icmab.es

Notes

The authors declare no competing financial interests.

ACKNOWLEDGMENT

ABBREVIATIONS

IET, intramolecular electron transfer; D, electron donor; A, electron acceptor; PTM, perchlorotriphenylmethyl radical; TTF, tetrathiafulvalene.

REFERENCES

(1) Rovira, C. *Chem. Rev.* **2004**, *104*, 5289.

(2) Farges, J. P. *Organic Conductors: Fundamentals and Applications*. Marcel Dekker, New York, USA **1994**.

(3) Bndikov, M.; Wudl, F.; Perepichka, D. F. *Chem. Rev.* **2004**, *104*, 4891.

(4) Nunes, J. P. M.; Figueira, M. J.; Belo, D.; Santos, I. C.; Ribeiro, B.; Lopes, E. B.; Henriques, R. T.; Vidal-Gancedo, J.; Veciana, J.; Rovira, C.; Almeida, M. *Chem. Eur. J.* **2007**, *13*, 9841.

(5) Tanaka, H.; Okano, Y.; Kobayashi, H.; Suzuki, W.; Kobayashi, A. *Science* **2001**, *291*, 285.

(6) Cui, H.; Kobayashi, H.; Ishibashi, S.; Sasa, M.; Iwase, F.; Kato, R.; Kobayashi, A. *J. Am. Chem. Soc.* **2014**, *136*, 7619.

(7) Jerome, D.; Mazaud, A.; Ribault, M.; Bechgaard, K. *J. Physique. Lett.* **1980**, *31*, 95.

(8) Haddon, R. C. *Nature* **1975**, *256*, 394.

(9) Chi, X.; Itkis, M. E.; Reed, R. W.; Oakley, R. T.; Cordes, A. W.; Haddon, R. C. *J. Phys. Chem. B.* **2002**, *106*, 8278.

(10) Pal, S. K.; Itkis, M. E.; Tham, F. S.; Reed, R. W.; Oakley, R. T.; Haddon, R. C. *Science* **2005**, *309*, 281.

(11) Pal, S. K.; Itkis, M. E.; Tham, F. S.; Reed, R. W.; Oakley, R. T.; Donnadieu, B.; Haddon, R. C. *J. Am. Chem. Soc.* **2007**, *129*, 7163.

(12) Haddon, R. C.; Sarkar, A.; Pal, S. K.; Chi, X.; Itkis, M. E.; Tham, F. S. *J. Am. Chem. Soc.* **2008**, *130*, 13683.

(13) Pal, S. K.; Itkis, M. E.; Tham, F. S.; Reed, R. W.; Oakley, R. T.; Haddon, R. C. *J. Am. Chem. Soc.* 2008, *130*, 3942.

(14) Pal, S. K.; Bag, P.; Sarkar, A.; Chi, X.; Itkis, M. E.; Tham, F. S.; Donnadieu, B.; Haddon, R. C. *J. Am. Chem. Soc.* **2010**, *132*, 17258.

(15) Sarkar, A.; Itkis, M. E.; Tham, F. S.; Haddon, R. C. *Chem. Eur. J.* **2011**, *17*, 11576.

(16) Bag, P.; Itkis, M. E.; Pal, S. K.; Bekyarova, E.; Donnadieu, B.; Haddon, R. C. *J. Phys. Org. Chem.* **2012**, *25*, 566.

(17) Pal, S. K.; Bag, P.; Itkis, M. E.; Tham, F. S.; Haddon, R. C. *J. Am. Chem. Soc.* **2014**, *136*, 14738.

(18) Brusso, J. L.; Cvrkalj, K.; Leitch, A.; Oakley, R. T.; Reed, R. W.; Robertson, C. M. *J. Am. Chem. Soc.* **2006**, *128*, 15080.

(19) Mailman, A.; Winter, S. M.; Yu, X.; Robertson, C. M.; Yong, W.; Tse, J. S.; Secco, R. A.; Liu, X.; Dube, P. A.; Howard, J. A. K.; Oakley, R. T. *J. Am. Chem. Soc.* **2012** *134*, 9886.

(20) Yu, X.; Mailman, A.; Lekin, K.; Assoud, A.; Robertson, C. M.; Noll, B. C.; Campana, C. F.; Howard, J. A. K.; Dube, P. A.; Oakley, R. T. *J. Am. Chem. Soc.* **2012**, *134*, 2264.

(21) Leitch, A. A.; Lekin, K.; Winter, S. M.; Downie, L. E.; Tsuruda, H.; Tsell, J. S.; Mito, M.; Desgreniers, S.; Dube, P. A.; Zhang, S.; Liu, Q.; Jin, C.; Ohishi, Y.; Oakley, R. T. *J. Am. Chem. Soc*. **2011**, *133*, 6051.

(22) Wong, J. W. L.; Mailman, A.; Lekin, K.; Winter, S. M.; Yong, W.; Zhao, J.; Garimella, S. V.; Tse, J. S.; Secco, R. A.; Desgreniers, S.; Ohishi, Y.; Borondics, F.; Oakley, R. T. *J. Am. Chem. Soc*. **2014**, *136*, 1070.

(23) Ratera, I.; Veciana, J. *Chem. Soc. Rev*. **2012**, *41*, 303.

(24) Guasch, J.; Grisanti, L.; Lloveras, V.; Vidal-Gancedo, J.; Souto, M.; Morales, D. C.; Vilaseca, M.; Sissa, C.; Painelli, A.; Ratera, I.; Rovira, C.; Veciana, J. *Angew. Chem. Int. Ed*. **2012**, *51*, 11024.

(25) Guasch, J.; Grisanti, L.; Souto, M.; Lloveras, V.; Vidal-Gancedo, J.; Ratera, I.; Painelli, A.; Rovira, C.; Veciana, J. *J. Am. Chem. Soc*. **2013**, *135*, 6958.

(26) Souto, M.; Guasch, J.; Lloveras, V.; Mayorga, P.; López-Navarrete, J. T.; Casado, J.; Ratera, I.; Rovira, C.; Painelli, A.; Veciana, J. *J. Phys. Chem. Lett*. **2013**, *4*, 2721.

(27) Souto, M.; Solano, M. V.; Jensen, M.; Bendixen, D.; Delchiaro, F.; Girlando, A.; Painelli, A.; Jeppesen, J. O.; Rovira, C.; Ratera, I.; Veciana, J. *Chem. Eur. J.* **2015**, *21*, 8816.

(28) Kresse, G.; Hafner, J. *Phys. Rev. B* **1993**, *47*, 558.

(29) Kresse, G.; Furthmüller, J. *Phys. Rev. B* **1996**, *54*, 11169.

(30) Perdew, J. P.; Burke, K.; Ernzerhof, M. *Phys. Rev. Lett.* **1996**, *77*, 3865.

(31) Koepernik, K.; Eschrig, H. *Phys. Rev. B* **1999**, *59*, 1743.

(32) Kotliar, G.; Vollhardt, D. *Physics Today* **2004**, *57*, 53.

(33) Zhao, Y.; Truhlar, D. G. *Theor Chem Account* **2006**, *120*, 215.

(34) Gaussian 09, Revision A.02, M. J. Frisch, G. W. Trucks, H. B. Schlegel, G. E. Scuseria, M. A. Robb, J. R. Cheeseman, G. Scalmani, V. Barone, B. Mennucci, G. A. Petersson, H. Nakatsuji, M. Caricato, X. Li, H. P. Hratchian, A. F. Izmaylov, J. Bloino, G. Zheng, J. L. Sonnenberg, M. Hada, M. Ehara, K. Toyota, R. Fukuda, J. Hasegawa, M. Ishida, T. Nakajima, Y. Honda, O. Kitao, H. Nakai, T. Vreven, J. A. Montgomery, Jr., J. E. Peralta, F. Ogliaro, M. Bearpark, J. J. Heyd, E. Brothers, K. N. Kudin, V. N. Staroverov, R. Kobayashi, J. Normand, K. Raghavachari, A. Rendell, J. C. Burant, S. S. Iyengar, J. Tomasi, M. Cossi, N. Rega, J. M. Millam, M. Klene, J. E. Knox, J. B. Cross, V. Bakken, C. Adamo, J. Jaramillo, R. Gomperts, R. E. Stratmann, O. Yazyev, A. J. Austin, R. Cammi, C. Pomelli, J. W. Ochterski, R. L. Martin, K. Morokuma, V. G. Zakrzewski, G. A. Voth, P. Salvador, J. J. Dannenberg, S. Dapprich, A. D. Daniels, O. Farkas, J. B. Foresman, J. V. Ortiz, J. Cioslowski, and D. J. Fox, Gaussian, Inc., Wallingford CT, 2009.

(35) Rodríguez, S.; Nieto-Ortega, B.; González-Cano, R. C.; Lloveras, V.; Novoa, J. J.; Mota, F.; Vidal-Gancedo, J.; Rovira, C.; Veciana, J.; Del Corro, E.; Taravillo, M.; Baonza, V. G.; López-Navarrete, J. T.; Casado, J. *J. Chem. Phys.* 2014, *140*, 164903/1-164903/9.

(36) Hattori, Y.; Kusamoto, T.; Nishihara, H. *Angew. Chem. Int. Ed.* **2014**, *53*, 11845.

(37) Yuan, H.; Wang, K.; Yang, K.; Liu, B.; Zou, B. *J. Phys. Chem. Lett.* **2014**, *5*, 2968.

(38) Schmidtke, J. P.; Kim, J.-S.; Gierschner, J.; Silva, C.; Friend, R. H. *Phys. Rev. Lett.* **2007**, *99*, 167401.

(39) Armet, O.; Veciana, J.; Rovira, C.; Riera, J.; Castañer, J.; Molins, E.; Rius, J.; Miravitlles, C.; Olivella, S.; Brichfeus, J. *J. Phys. Chem.* **1987**, *91*, 5608.

(40) Baonza, V. G.; Taravillo, M.; Arencibia, A.; Cáceres, M.; Núñez, J. *J. Raman Spectrosc.* **2003**, *34*, 264.

(41) Del Corro, E.; González, J.; Taravillo, M.; Flahaut, E.; Baonza, V. G. *Nano Lett.* **2008**, *8*, 2215.

Pressure-induced Conductivity in a Neutral Non-Planar Spin-Localized Radical

Manuel Souto, HengBo Cui, Miriam Peñá-Álvarez, Valentín G. Baoza, Harald O. Jeschke, Milan Tomic, Roser Valentí, Davide Blasi, Imma Ratera, Concepció Rovira, and Jaume Veciana
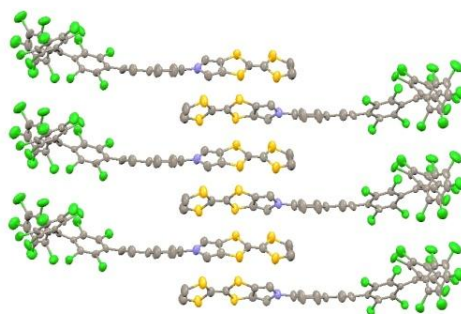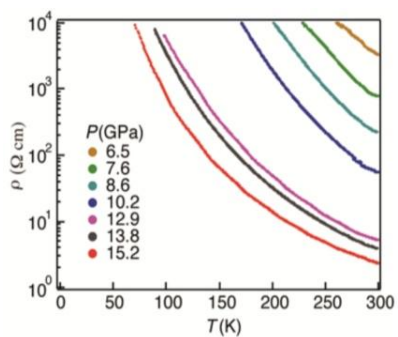
Supporting Information

Pressure-Induced Conductivity in a Neutral Non-planar Spin-localized Radical

Manuel Souto,[†] HengBo Cui,[‡] Miriam Peña-Álvarez,[¶] Valentín G. Baonza,[¶] Harald O. Jeschke,[§] Milan Tomic,[§] Roser Valentí,[§] Davide Blasi,[†] Imma Ratera,[†] Concepció Rovira,[†] and Jaume Veciana*[,†]

[†]Institut de Ciència de Materials de Barcelona (ICMAB-CSIC)/CIBER-BBN, Campus Universitari de Bellaterra, 08193 Cerdanyola del Vallès (Barcelona), Spain

[‡]Condensed Molecular Materials Laboratory, RIKEN, Wako-shi, Saitama 351-0198, Japan

[¶]MALTA CONSOLIDER Team, Departamento de Química Física I, Facultad de Ciencias Químicas, Universidad Complutense de Madrid, 28040-Madrid, Madrid, Spain

[§]Institut für Theoretische Physik, Goethe-Universität Frankfurt, Max-von-Laue-Straße 1, 60438 Frankfurt am Main

Contents

1. Crystal data of radicals 1 and 2

Crystallographic measurements were carried out on a *BRUKER SMART APEX CCD* diffractometer using graphite-monochromated Mo Kα radiation (λ = 0.71073 Å) from an x-Ray Tube. Programs used: data collection, Smart version 5.631 (Bruker AXS 1997-02); data reduction, Saint + version 6.36A (Bruker AXS 2001); absorption correction, SADABS version 2.10 (Bruker AXS 2001). Structure solution and refinement was done using SHELXTL Version 6.14 (Bruker AXS 2000-2003). Data collection, structure solution, refinement was performed by X. Fontrodona (Serveis Tècnics de Recerca, Universitat de Girona, Spain).

Red crystals of radical **2** ($C_{19} Cl_{15}$) were grown from a slow diffusion of hexane in a CH_2Cl_2 solution of the compound, and used for room temperature (at 298(2) K) X-ray structure determination. The measurements were made in the range 1.469 to 28.285° for θ. Hemi-sphere data collection was carried out with ω and φ scans. A total of 19909 reflections were collected of which 14000 [R(int) = 0.0510] were unique.

The structure was solved by direct methods and refined by full-matrix least-squares methods on F^2. The non-hydrogen atoms were refined anisotropically. A considerable amount of spurious electron density non attributable to any solvent molecule was removed with the SQUEEZE option of PLATON.

Final R indices [I>2sigma(I)]   **R1 = 0.0691,** wR2 = 0.1541

R indices (all data)   R1 = 0.1766, wR2 = 0.2052

Dark crystals of radical dyad **1** ($C_{35} H_{10} Cl_{14} N S_4$), were grown from hexane/dichlorometane, and used for room temperature (at 298(2) K) X-ray structure determination. The measurements were made in the range 2.040 to 28.354° for θ. Full-sphere data collection was carried out with ω and φ scans. A total of 64741 reflections were collected of which 20060 [R(int) = 0.1286] were unique.

The structure was solved by direct methods and refined by full-matrix least-squares methods on F^2. The non-hydrogen atoms were refined anisotropically. The H-atoms were placed in geometrically optimized positions and forced to ride on the atom to which they are attached.

Final R indices [I>2sigma(I)]   **R1 = 0.0614**, wR2 = 0.1036

R indices (all data)   R1 = 0.2193, wR2 = 0.1457

More information about the crystal structure of **1** is reported in reference S1.

Table S1. Crystal data and selected intermolecular distances for **1** and **2**.

	1	2
Formulas	$C_{35}H_{10}Cl_{14}NS_4$	$C_{19}Cl_{15}$
FW (g/mol)	1069.06	760.00
a (Å)	17.411(3)	8.960(3)
b (Å)	7.951(6)	13.051(5)
c (Å)	30.177(3)	27.917(10)
V (Å³)	4060.98	3190.08
space group	$P\,2_1$	$P\bar{1}$
Z	4	4
R-factor (%)	6.14	6.91
ipso-C--*ipso*-C (Å)	7.952	13.05
Ph-C---*Ph*-C planes (Å)	6.48 (7.952)	11.87 (13.05)
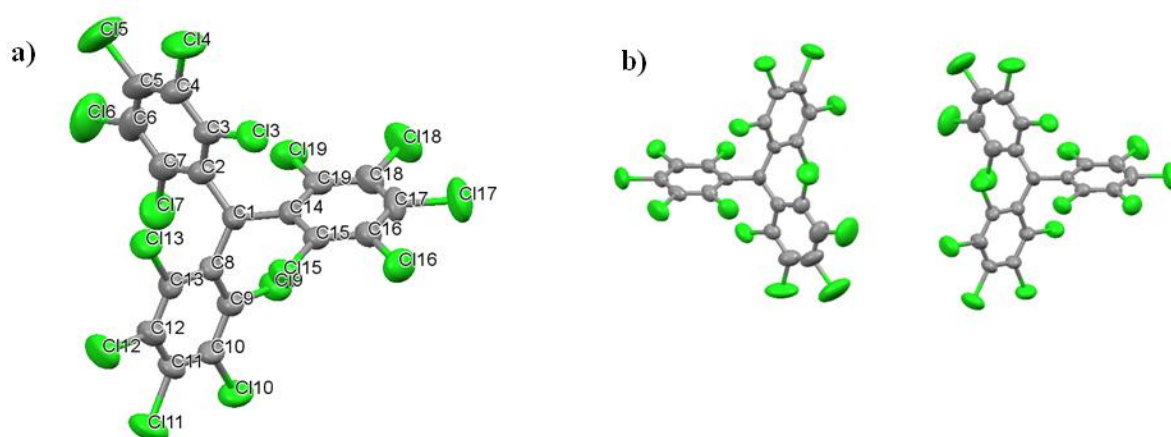
Figure S1. (a) ORTEP view of radical **2** at 300 K. (**b**) Asymmetric unit of radical **2**. Atoms are shown at the 50% probability level.
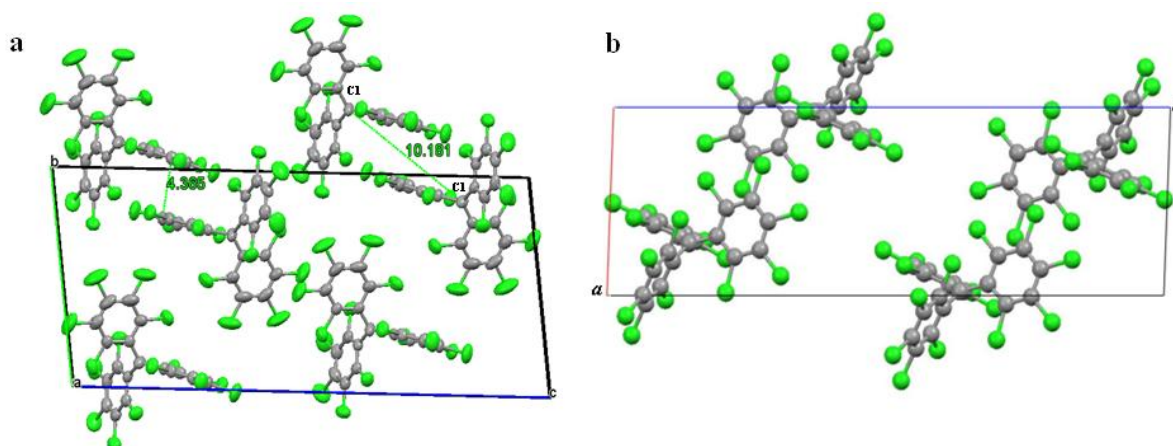
Figure S2. Molecular arrangement of radical **2** on the *bc* (*left*) and *ac* planes (*right*).
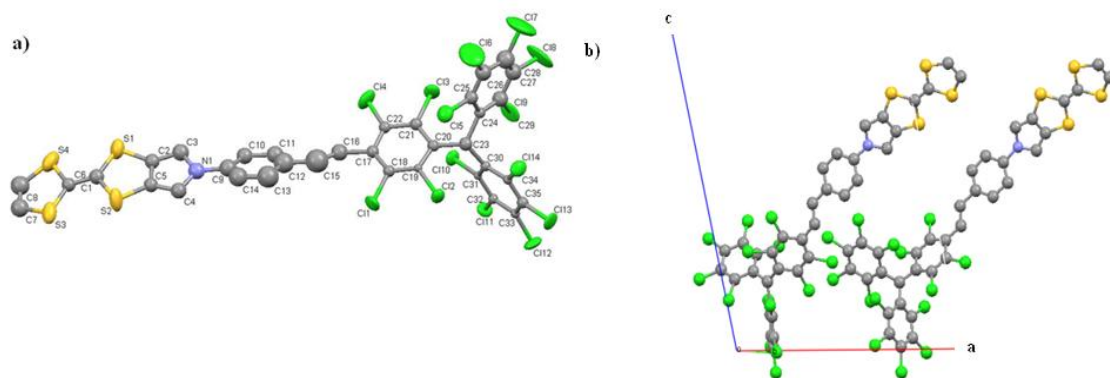
Figure S3. (a) ORTEP view of radical dyad **1** at 300 K. (**b**) Asymmetric unit of **1** on the *ac* plane. Hydrogen atoms are omitted for clarity. Atoms are shown at the 50% probability level.
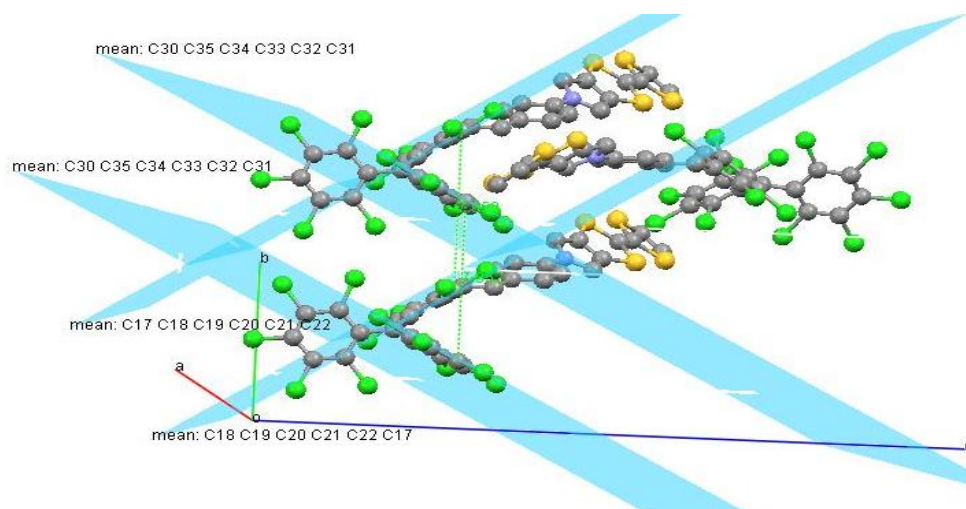
Figure S4. Planes including the phenyl rings of the PTM unit of two adjacent molecules of radical dyad **1** on the *bc* plane.
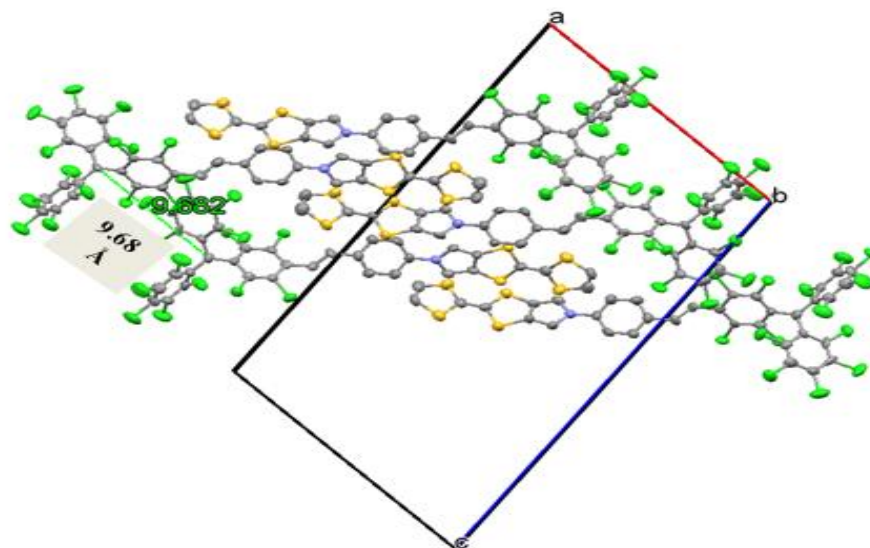
Figure S5. Molecular arrangement of radical dyad **1** on the *ac* plane.

2. High-pressure conductivity measurements of radicals 1 and 2

High-pressure resistivity measurements of radicals **1** and **2** were carried out following the reported procedure by a diamond anvil cell (DAC) four-probe DC measurements.[2] Three single crystals of radical dyad **1** and three of radical **2** with average sizes of 0.11-0.13 mm were used for the high-pressure measurements. The four contacts were made by 10 μm(or 5 μm) gold wires and attached to the crystal with gold paint. The diamond culet size 0.7 mm and tension annealed SUS301 were used for the two first samples, and the diamond culet size 0.56 mm and Inconel 625 were used for the third sample, respectively. Daphne Oil 7373 was used as the pressure-transmitting medium. The pressure was determined by the shift of the ruby fluorescence $R1$ lines at room temperature.
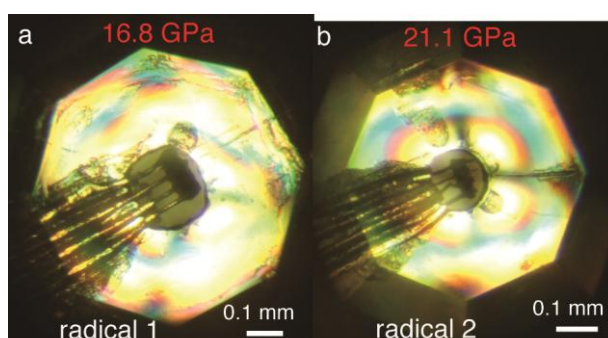
Figure S6. Pictures of resistivity measurements of crystals (**a**) radical dyad **1** under 16.8 GPa, (**b**) radical **2** under 21.1 GPa.

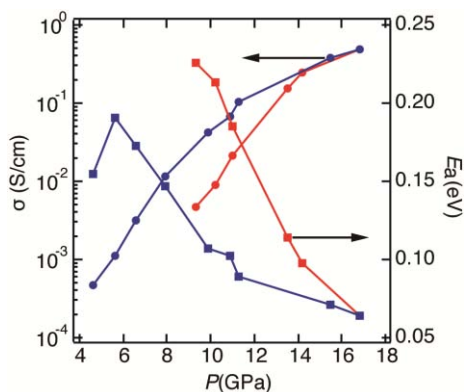### Reversibility and reproducibility of conductivity measurements
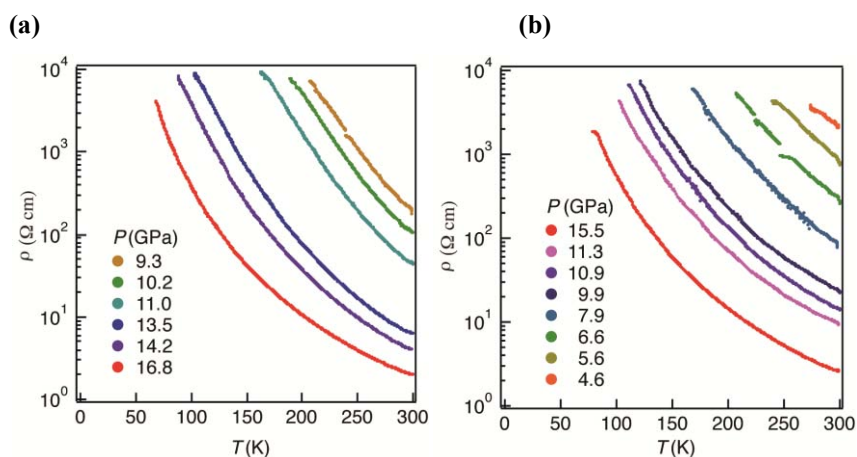
(c)

Figure S7. Reversibility measurements on one sample of radical dyad **1** under (**a**) increasing pressure, (**b**) decreasing pressure and (**c**) pressure dependence of the conductivity σ(298 K) and of activation energy E_a (circle). The red symbols are increasing pressure data and the blue symbols are decrease pressure data.

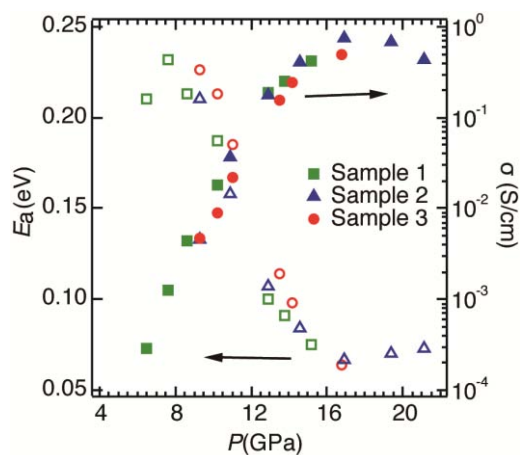**Figure S8**. Pressure dependence of the conductivity σ(298 K) (closed symbols) and E_a (open symbols) of three different crystals of radical dyad **1**.
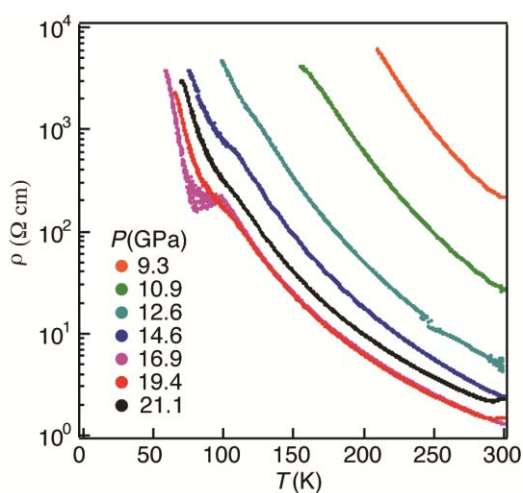
Figure S9. Pressure and temperature dependence of the resistivity of sample #2 of radical dyad **1.**
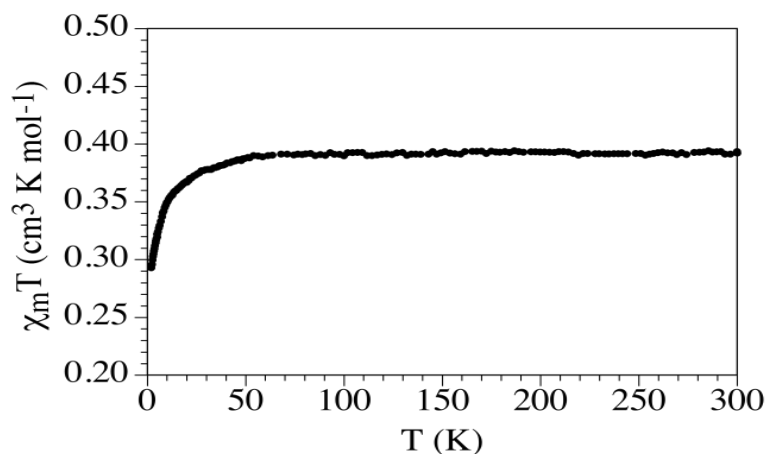
3. Magnetic susceptibility of radical dyad 1

Figure S10. Magnetic susceptibility of crystals of radical dyad **1** as function of temperature.
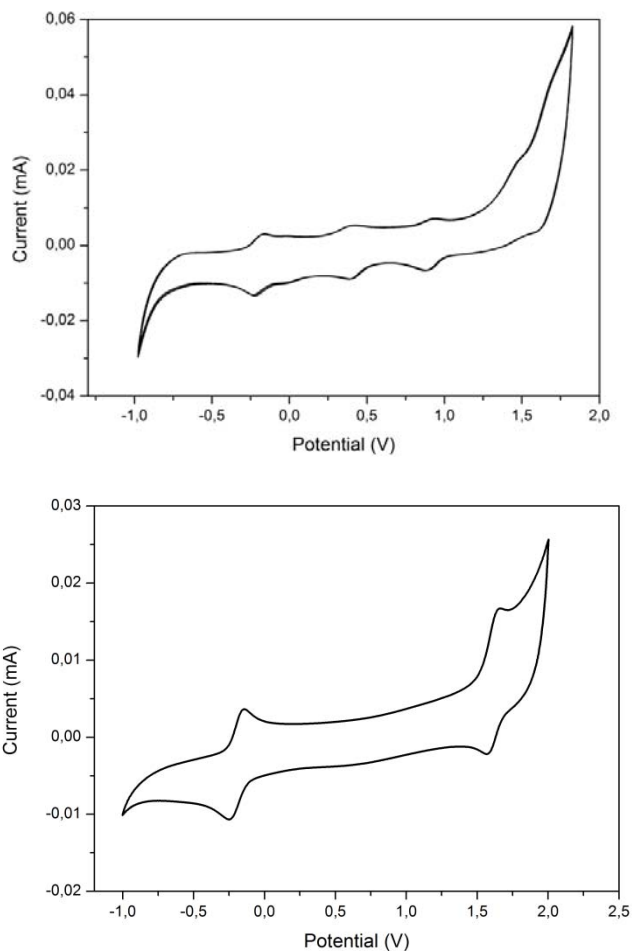
4. Cyclic voltammetry of radicals 1 and 2

Figure S11. Cyclic voltammetry of solution of radical dyad **1** (above) and radical **2** (below) in CH_2Cl_2 vs. Ag/AgCl using n-Bu_4PF_6 (0.1 M) as electrolyte at 300 K under argon at a scan rate of 0.1 V/s. Ferrocene/ferrocinium (Fc/Fc$^+$) couple was used as internal reference.

5. Simulated crystal structures, band structures and charge transfer calculations of radical dyad 1 under pressure

We employed the projector augmented wave basis as implemented in VASP [3] to predict the structure of **1** at elevated hydrostatic pressure. The calculations have been performed in two different ways: First as constant pressure predictions of the structure, using the Γ point only; then by constant volume calculations using a $2 \times 4 \times 2$ k mesh. Fig. S12 shows how lattice parameters *a*, *b* and *c*, monoclinic angle *β* and volume *V* evolve as function of hydrostatic pressure. The constant volume calculations yield lower enthalpies and are thus of higher quality (see Fig. S13). In Fig. S12, the constant pressure calculations are shown with dashed lines for comparison. Plane wave cutoff for the calculations shown here is 400 eV.
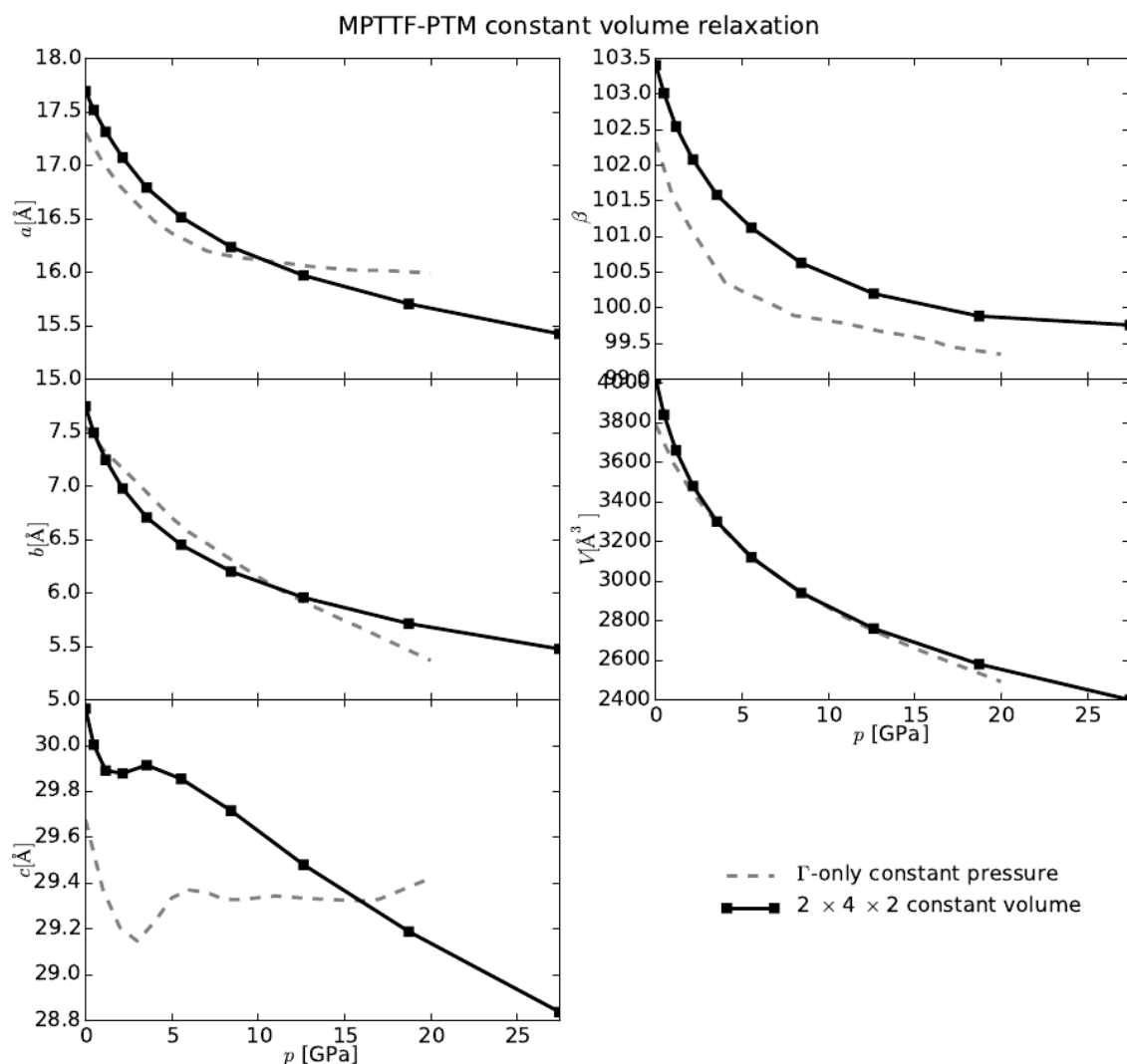

Figure S12. Simulation of the evolution of structural parameters of radical dyad **1** with hydrostatic pressure
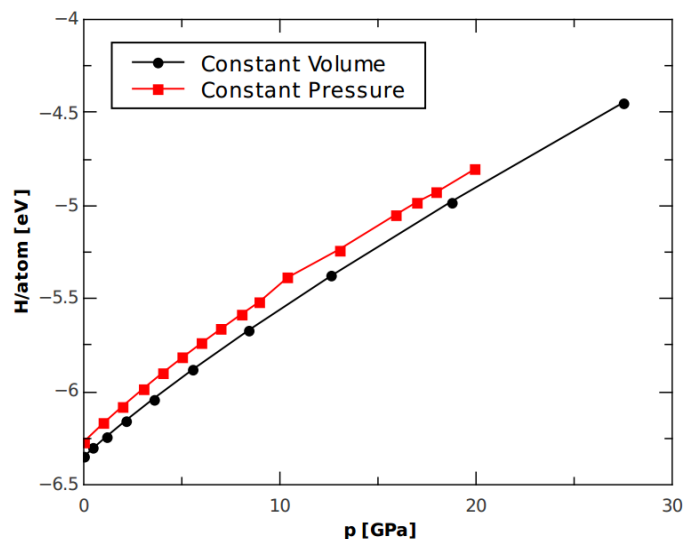
Figure S13. Comparison of enthalpies as function of hydrostatic pressure for constant volume and for constant pressure simulations of radical dyad **1**.

Table S2. Pressure, cell parameters and energies of optimized crystal structures at different pressures.

| Pressure (GPa)	Volume ($Å^3$/molecule)	a (Å)	b (Å)	c (Å)	α (º)	β (º)	γ (º)	Energy (Hartree/molecule)
-0.3	1050	17.9073	7.9494	30.3635	90	103.6619	90	-9451.547208
0.13	1005	17.6934	7.7440	30.1612	90	103.4075	90	-9451.533527
0.6	960	17.5180	7.4985	30.0033	90	103.0129	90	-9451.514042
1.3	915	17.3133	7.2453	29.8910	90	102.5447	90	-9451.486834
2.3	870	17.0720	6.9768	29.8789	90	102.0810	90	-9451.449433
3.7	825	16.7916	6.7062	29.9147	90	101.5859	90	-9451.398515
5.7	780	16.5148	6.4492	29.8550	90	101.1240	90	-9451.328662
8.6	735	16.2357	6.2001	29.7162	90	100.6296	90	-9451.232341
12.8	690	15.9698	5.9566	29.4803	90	100.1986	90	-9451.098249
18.9	645	15.7042	5.7134	29.1882	90	99.8841	90	9450.909632
27.8	600	15.4229	5.4755	28.8371	90	99.7591	90	-9459.643142
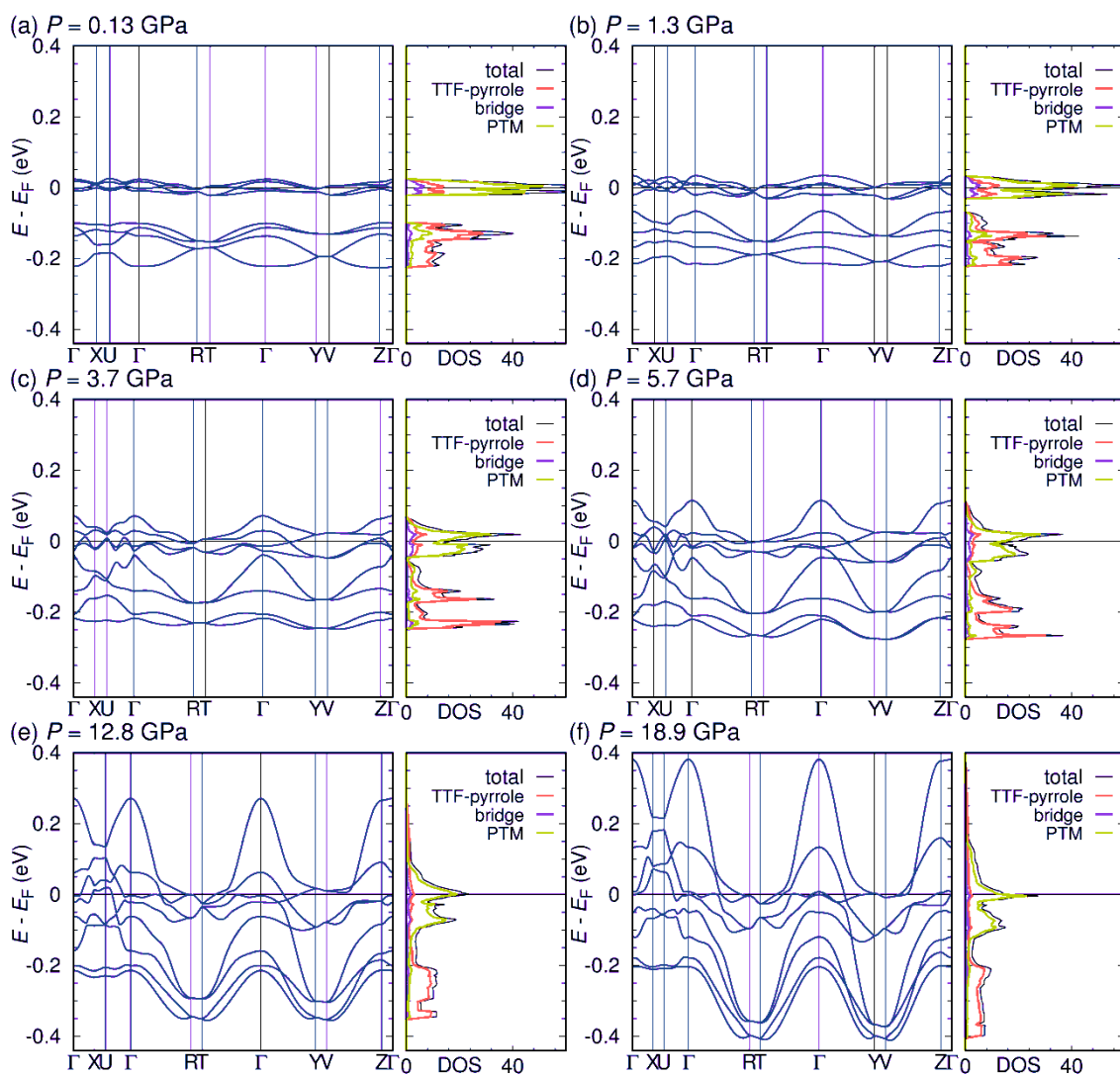
Figure S14. Evolution of band structure and density of states of radical dyad **1** with hydrostatic pressure.
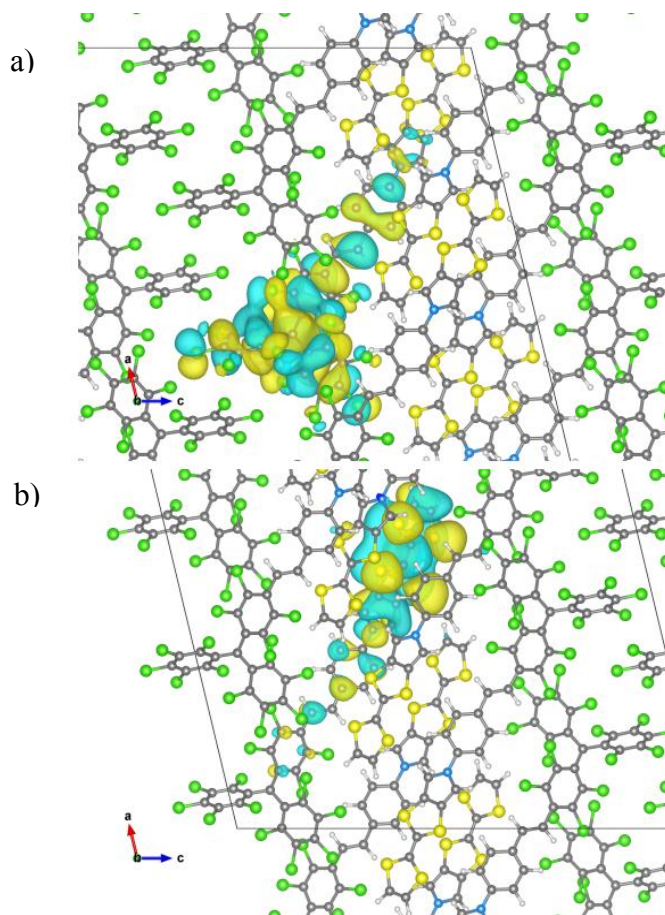
Figure S15. Wannier functions of radical dyad **1** around ambient pressure. (**a**) Wannier function for bands around EF. (**b**) Wannier function for bands at E = −0.15 eV.
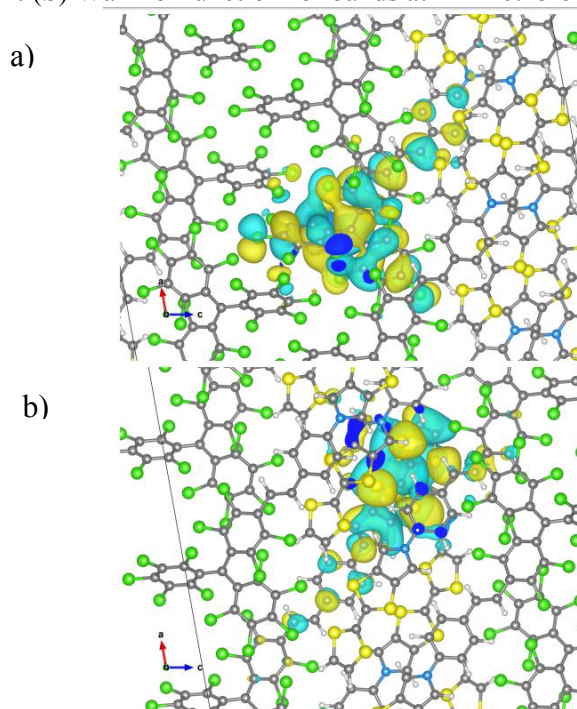

Figure S16. Wannier functions of radical dyad **1** at P = 12.8 GPa. (**a**) Wannier function for bands around EF. (**b**) Wannier function for bands at E = −0.25 eV.

6. Experimental and simulated Raman spectra at ambient pressure of radical dyad 1

Raman measurements at high pressure were performed in a sapphire cell with a diameter culet of 360 μm and a gold gasket. No pressure transmitting medium was used and diamond chips were placed as the pressure calibrant. Raman measurements were performed using an air-cooled argon ion laser, a Spectra-Physics solid state laser, at 532.0 nm. Diamond chips were used as pressure sensor.[4] The device is equipped with a 10x Mitutoyo long working distance objective coupled to a 10x Navitar zoom system and focused onto the slit of an ISA HR460 monochromator with a grating of 600 grooves mm^{-1} and a liquid nitrogen cooled CCD detector (ISA CCD3000, 1024−256 pixels). Spectra were measured with a spectral resolution of about 2−3 cm^{-1} and calibrated with a standard neon emission lamp. The SAC is mounted on a xyz stage, which allows us to move the sample with an accuracy of 1 μm. The typical sampling area was about 1−2 μm in diameter.

For all calculations the UM06 density functional theory was used [5] in conjunction with the 6-31G** basis set.[6] All computations were done with Gaussian 09.[7] Reported frequencies are harmonic frequencies and were uniformly scaling throughout with the scaling factor of 0.96. The energy minimization of a single molecule was performed with starting geometry from the crystal structure. The minimum was confirmed by a vibrational frequency analysis: all computed frequencies were real. ChemCraf program was used for representing vibrational displacements.[8] Spectra were generated by the GaussSum-2.2.5 program with a broadening of 3 cm^{-1}.[9]
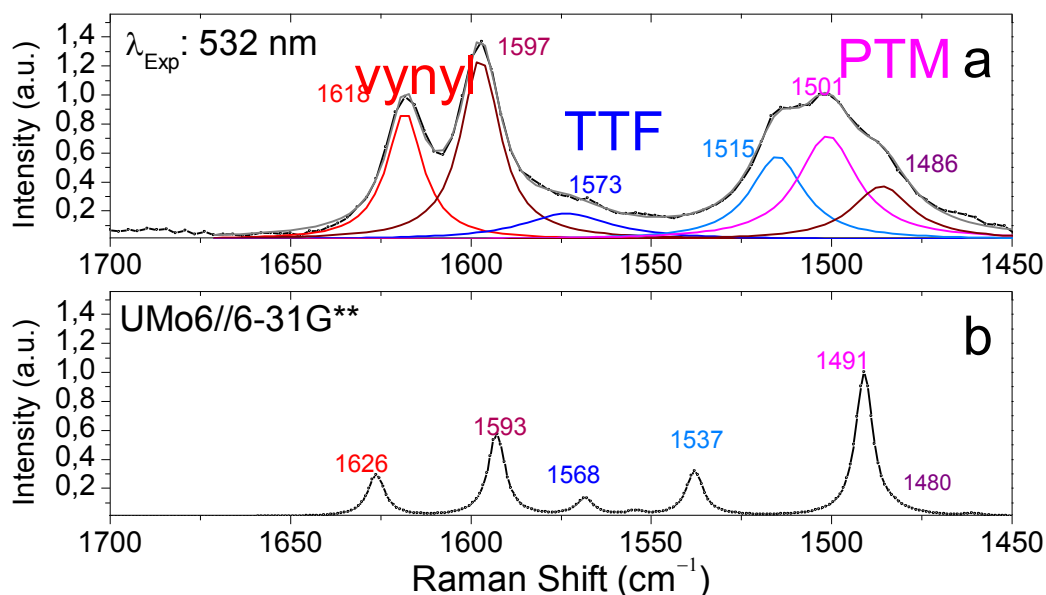

Figure S17. Raman spectra at ambient pressure. (**a**) Experimental Raman spectrum of crystals of **1** measured at ambient pressure with a laser of 532 nm in the 1700-1450 cm^{-1} region. (**b**) Simulated Raman spectrum of **1** in the 1700-1450 cm^{-1} region.
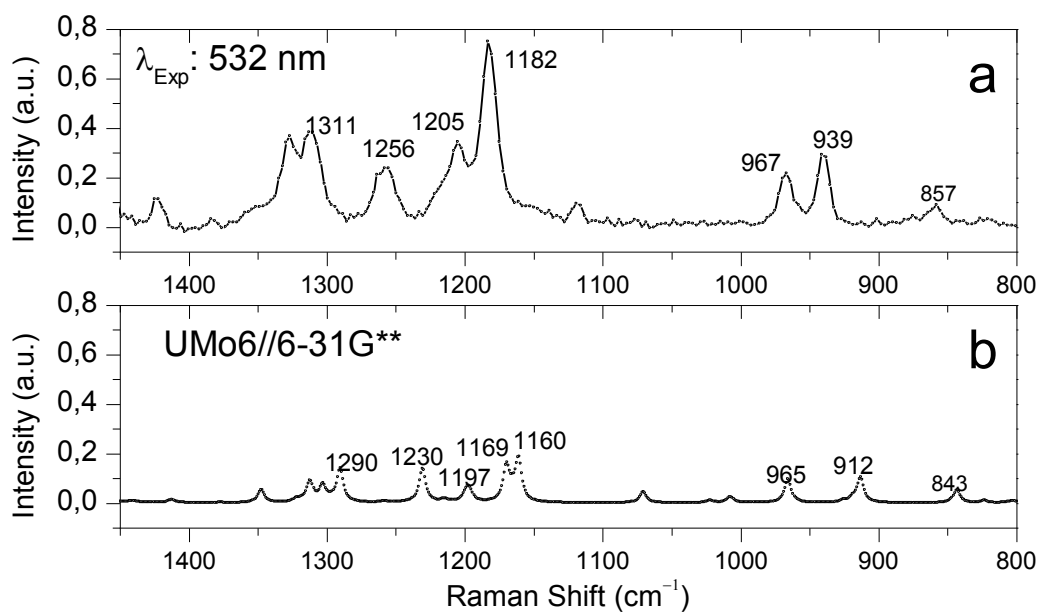
Figure S18. Raman spectrum at ambient pressure. (a) Experimental Raman spectrum of crystal of **1** measured at ambient pressure with a laser of 532 nm in the 1450-800 cm^{-1} region. **(b)** Simulated Raman spectrum of in the 1450-800 cm^{-1} region.

7. Raman bands assignments

Experimental Raman shift (cm^{-1})	Calculated Raman shift 0.96 scaled (cm^{-1})	Eigenvectors	Description
1618	1626		C-C stretching of vinylene + Inner phenyl C-C stretching
1597	1593		+ Inner phenyl C-C stretching + C-C stretching of vinylene
1573	1568		C=C stretching of the TTF
1515	1537		C=C stretching of the TTF + C=C stretching of the pyrrol
1501	1491		Anti-symmetric C=C stretching of the inner PTM
1486	1480		PTM anti-symmetric C=C stretching
1311	1290		Pyrrol breathing +Phenyl breathing +in plane CH bending
1256	1230		PTM breathing + in plane CH bending
1205	1169		Pirrol breathing + in plane CH bending
1182	1160		In plane CH bending +phenyl breathing + pirrol breathing + PTM stretching
967	965		Vynil's CH out of plane bending
939	912		Pyrrol breathing + phenyl breathing
887	843		Phenyl CH Out of plane bending

Figure S19. Vibrational eigenvectors associated with the most relevant bands of the Raman spectrum of 1 dye. Values obtained from calculations with UM06/6-31G(d,p) followed by uniform frequency scaling with a value equals to 0.96.

8. Experimental and simulated Raman spectra of radical dyad 1 at different pressures

For all calculations the UM06 density functional theory was used in conjunction with the 6-31G** basis set.[6] All computations were done with Gaussian 09.[8] Reported frequencies are harmonic frequencies and were uniformly scaling throughout with the scaling factor of 0.96.[7] A single molecule from the predicted crystal structure was performed with starting geometry from the crystal structure optimization at each pressure with full potential local orbital (FPLO) basis set and GGA functional. Spectra were generated by the GaussSum-2.2.5 program with a broadening of 3 cm^{-1}.
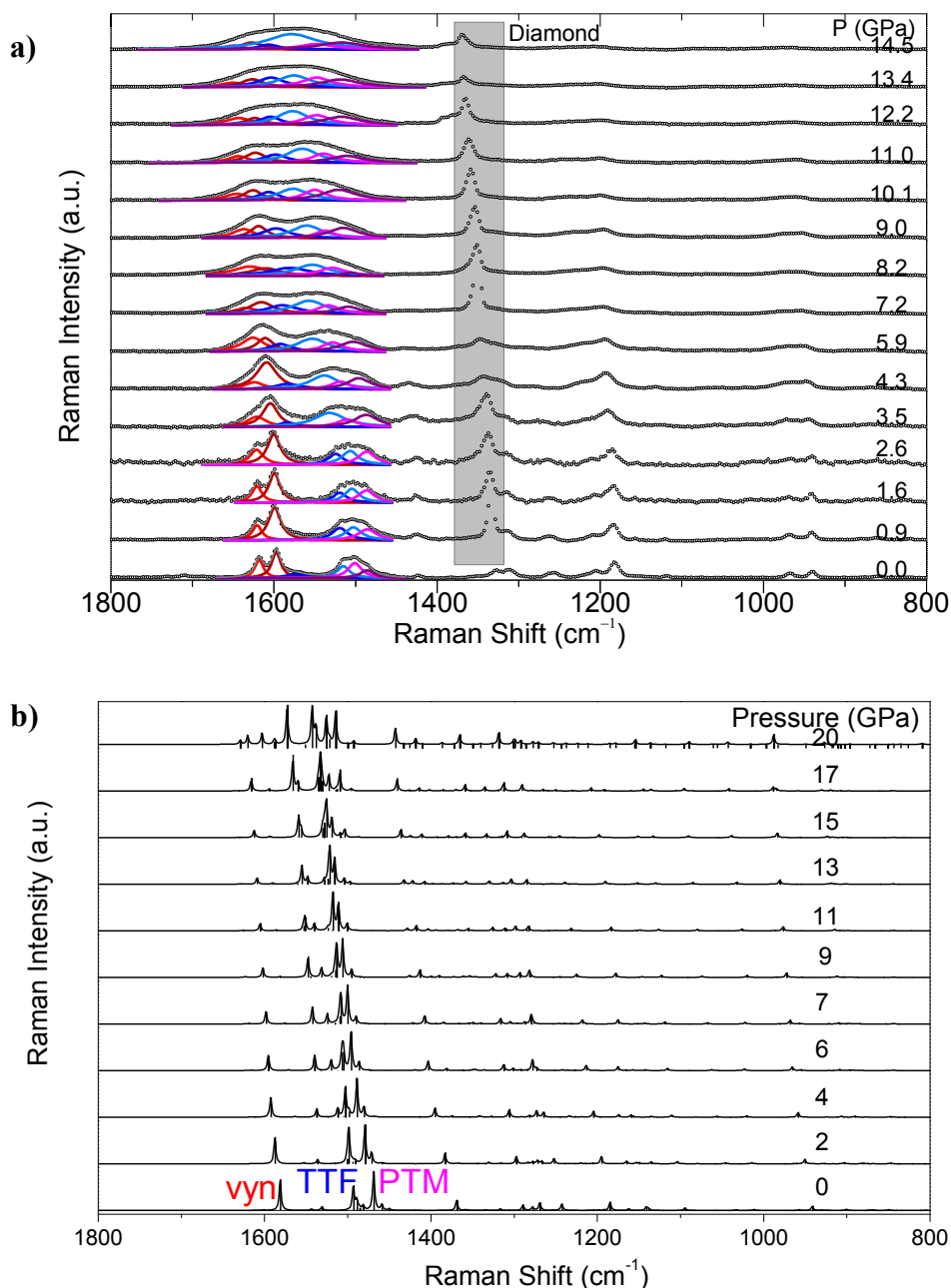

Figure S20. (**a**) Experimental and (**b**) UMO6/6-31G** simulated Raman spectrum of crystal of radical dyad **1** in the 1800-800 cm^{-1} region at different pressures.
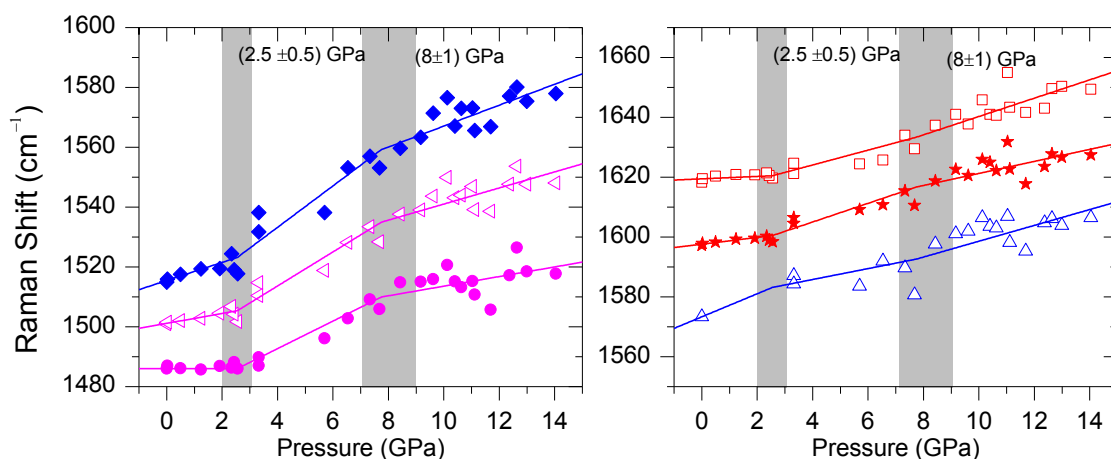
Figure S21 Raman shift pressure evolution of the dyad **1**. Pink symbols correspond to the PTM anti-symmetric C=C stretching modes; blue symbols to the C=C stretching of the TTF modes and red symbols to the C-C stretching of vinylene + Inner phenyl C-C stretching mode. Open and closed symbols are used to distinguish between the two different contributions of each kind of vibrational mode. Experimental data have been fitted to a triple linear trend; solid lines correspond to such fit. Vertical grey regions correspond to the pressures of interception between each linear trend.

Table S3. Experimental interceptions and pressure coefficients of the dye 1 Raman bands before in the first, second and third regimens, S_1, S_2 and S_3, respectively

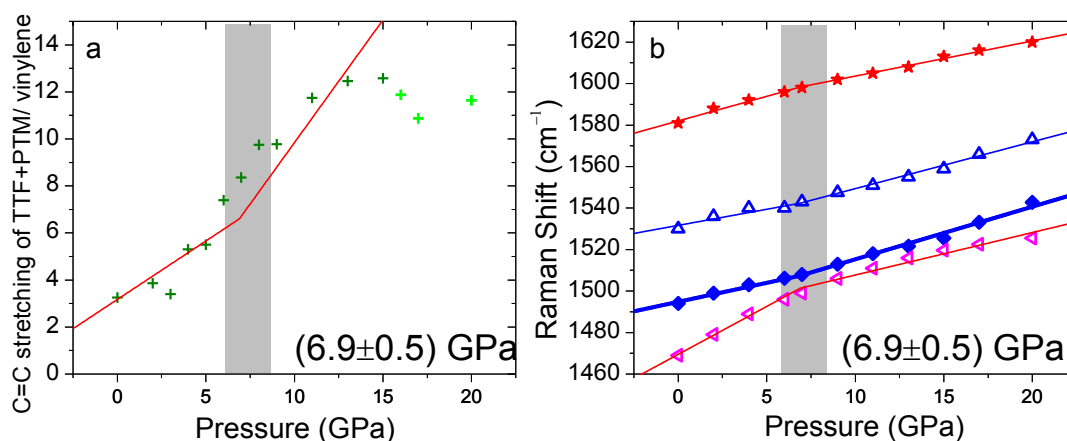|	PTM anti-symmetric C=C stretching		C=C stretching of the TTF		C-C stretching of vinylene + Inner phenyl C-C stretching	
ω_0 (cm^{-1})	1488	1501	1515	1573	1597	1618
$S_1(cm^{-1}/GPa)$	0±0	2±1	3±1	4±2	1.1±1.0	0.4±1.0
$S_2(cm^{-1}/GPa)$	4.6±0.6	5.7±0.6	6.9±0.6	1.8±0.8	3.1±0.5	2.5±0.5
$S_3(cm^{-1}/GPa)$	1.6±0.5	2.7±0.5	3.5±0.5	2.6±0.5	2.0±0.5	3.1±0.5

Figure S22. Pressure dependent data obtained from the calculated M06/6-31G** Raman spectra a) Intensity ratio of Raman bands of radical dyad **1** assigned to: C=C stretching of TTF+PTM/vinylene. b) Raman shift pressure evolution of the dyad **1**. Pink symbols correspond to the PTM anti-symmetric C=C stretching modes; blue symbols to the C=C stretching of the TTF modes and red symbols to the C-C stretching of vinylene + Inner phenyl C-C stretching mode. Data have been fitted to a double linear trend; solid lines correspond to such fit. Vertical grey regions correspond to the pressures of interception between each linear trend

Table S4. Calculated UM06/6-31G** interceptions and pressure coefficients of the dye 1 Raman bands before in the second and third regimens, S_2 and S_3, respectively. There is no first regimen since experimentally it is assigned to changes in molecular packing and for Raman calculations we are taking into account a single molecule.

	PTM anti-symmetric C=C stretching	C=C stretching of the TTF		C-C stretching of vinylene + Inner phenyl C-C stretching
ω_0 (cm^{-1})	1470	1491	1530	1580
S_2(cm^{-1}/GPa)	4.6±0.3	1.8±0.2	1.6±0.2	2.4±0.2
S_3(cm^{-1}/GPa)	2.0±0.1	2.5±0.1	2.3±0.1	1.7±0.1.

Experimentally it is observe that all the analyzed bands shift in there different regimens: 0-(2.5±0.5) GPa; -(2.5 ± 0.5) - -(8 ± 1), and -(8 ± 1) to the upper limit. This fittings have been done with a triple linear fit in which the transitions points are shared between all the data. The Raman shift in the first regimen is significantly lower than in the second one. This is because in this first low pressure range molecular changes related with crystal rearranges occur and these do not induce large intra molecular effects. Thus it can be said that it is in the second regimen when pressure induces intramolecular effects which alter C-C distances. It is seen that pressure coefficients of the terminal units are larger than those of the central vinylene unit, in agreement with a structural and electronic reorganization towards this central unit. Additionally, these experimental values are in good agreement with those theoretically calculated: larger coefficients in the terminal units. However, in the single molecule high pressure dependent calculated spectra the first regimen which confirms that experimentally mainly inter molecular reorganization occurs. Because of the Raman computations on the high pressure molecules are done without energy minimization on a single molecule taken from the optimized crystal, these Raman spectra do show imaginary frequencies and also not all the bands are observed. Nevertheless, the pressure transition at 8 GPa would correspond with that predicted at around 6 GPa from the calculated Raman spectra.

On the other hand, this high pressure behavior is uniquely observed to this molecular system. High pressure studies reported in the literature on analogues systems gathered Raman shift linear trends with lower pressure coefficients.[9]
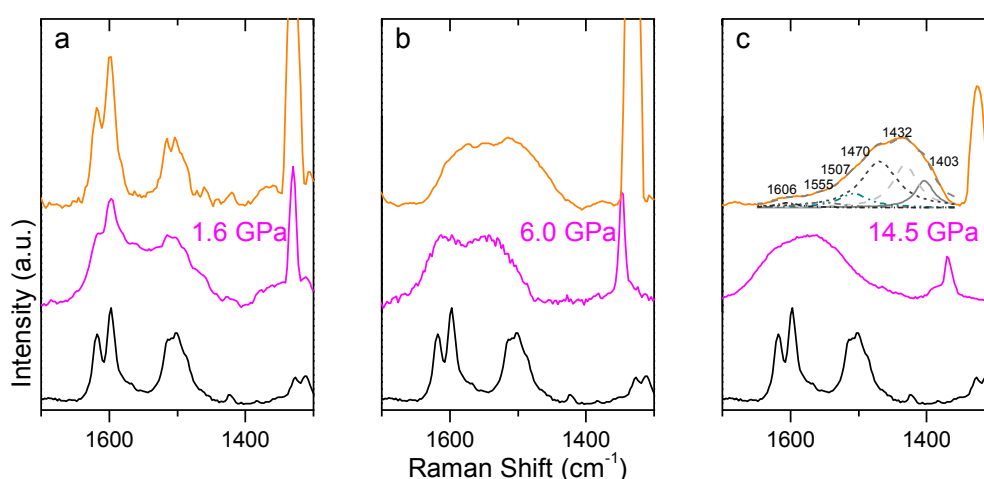

Figure S23. Three individual Raman experiments at pressures of a) 1.6 GPa, b) 6.0 GPa, c)14.5 GPa. Black line from below shows the initial Raman at ambient pressure, pink line the spectrum at the highest pressure reached in that experiment, and orange line is the spectrum after applying the pressure outside the cell.

9. High-pressure photoluminescence measurements

Two different high pressure experiments were conducted in a sapphire anvil cell (Figure S24) [4,11]. The pristine sample was used as starting material which was placed on a non-drilled gold gasket in the same conditions. In the experiments diamond chips were placed as the pressure calibrant and anvils had culets of with a 380 μm. Raman and photoluminescence measurements were performed using an air-cooled argon ion laser, a Spectra-Physics solid state laser, operating at 532.0, nm.
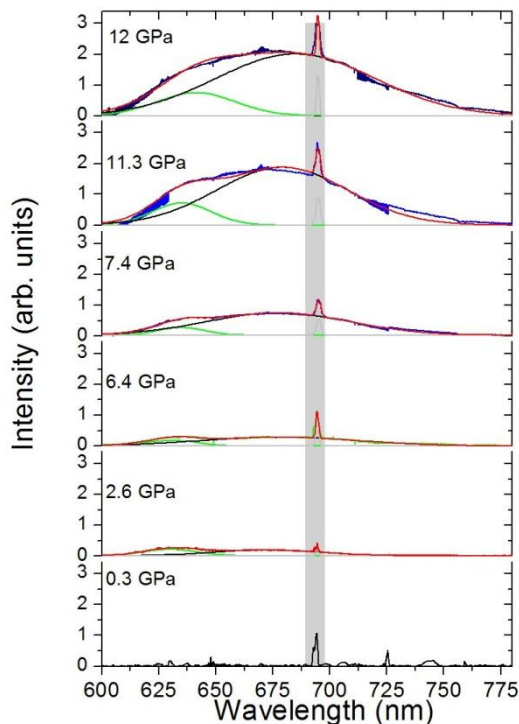

Figure S24. Deconvolution of the high resolution photoluminiscence spectra of crystals of radical dyad **1** at selected pressures when the sample was monochromatically excited with 532 nm. The experiments were conducted with a sapphire anvil cell. In green a low wavelength band have been fitted and in black the growing high wavelength band, assigned to the intermolecular charge transfer. Red line corresponds to the sum of both contributions.

In Figure S24 it can be seen that parallel to the intensity growth of the band assigned to the SOMO-LUMO transition, 680 nm, another feature appears at slightly higher energy (1.9 eV). The intensity of the latter is lower than that of the band at 680 nm. However, when the photoluminescence spectrum of the sample out of the anvil was measured (Figure S26) none of these bands were visible. We speculate about the possibility that the high energy band sets its origin in an analogues intermolecular charge transfer transitions.
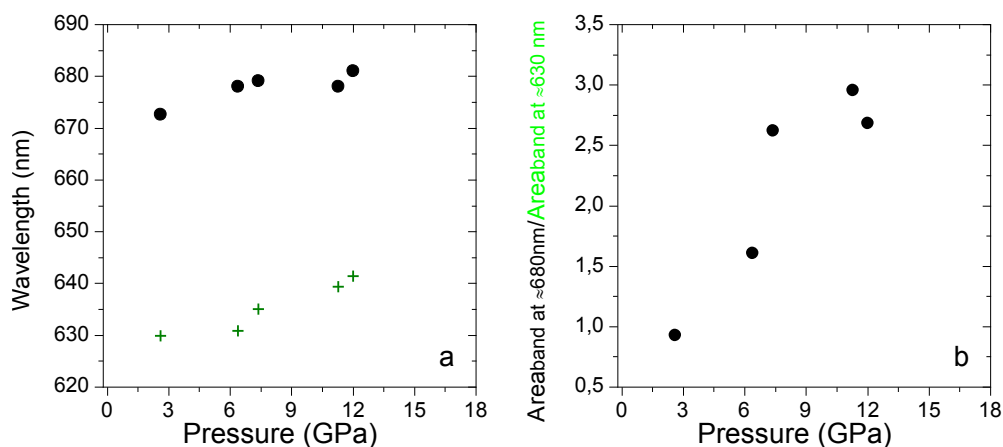
Figure S25. Pressure evolution of: a) wavelength of the bands, b) intensity ratio of the 680 nm band divided by the intensity of the 630 nm band.

In Figure S25a we have represented the wavelength of both contributions as a function of pressure. It seems like there is a slight upshift with increasing pressure in both bands. Additionally in Figure S25b the relative area of the 680 nm band respect the 630 nm band is represented as a function of pressure. It is seen how the intensity of the band at 680 nm rapidly increases with pressure.

In Figure S26 the photoluminescence spectrum of the recovered sample after pressure cycle is represented together with the spectrum of the pristine sample. It is seen that in the recovered sample both of the contributions remain but that around 1.8 eV has strongly increased in intensity.
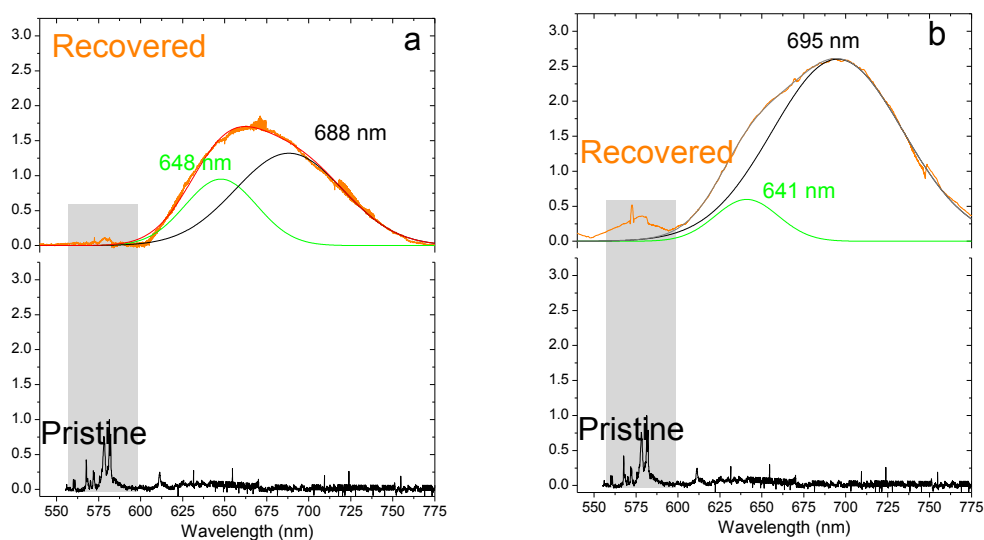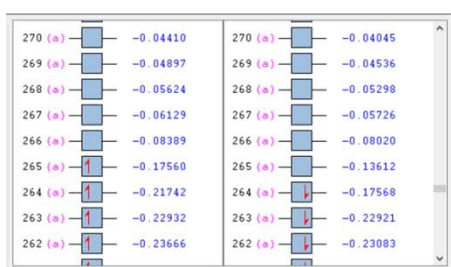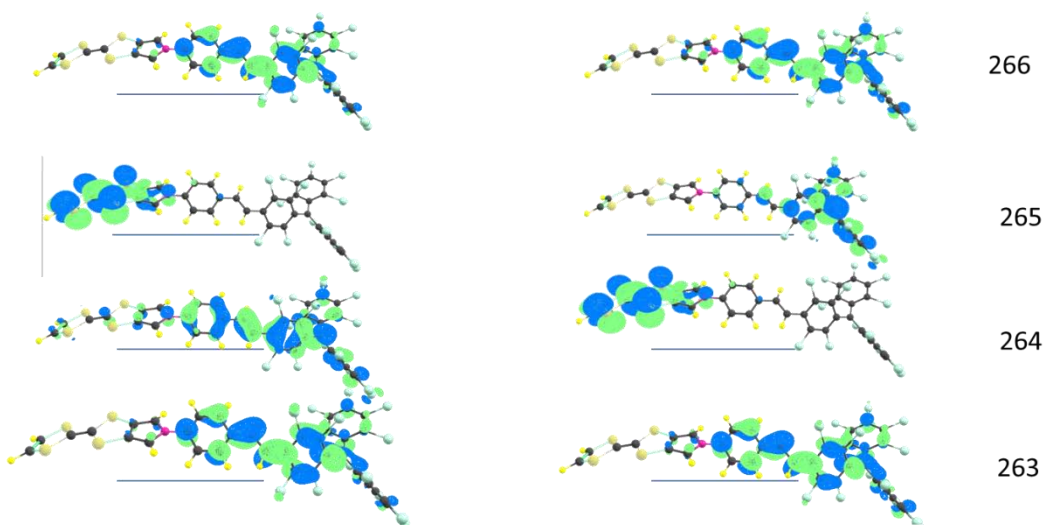

Figure S26. Photoluminescence spectra when the sample was excited at 532 nm of crystals of radical dyad **1** at room pressure before (black line) and after pressure (orange line) treatment (a) up to 6 GPa and (b) up to 12 GPa.

Table S5. Extracted results of DFT calculations (UM06/6-31G**) (264A is SOMO). Orbital energies in Hartrees.

P (GPa)	Absorption wavelength (nm)	Oscillator strength	Main transition involved	
0	522.61 nm	f=0.1885	264A ->266A	0.54855
1	524.66 nm	f=0.1844	264A ->266A	0.55246
2	527.05 nm	f=0.1790	264A ->266A	0.55221
3	529.35 nm	f=0.1690	264A ->266A	0.54782
4	532.85 nm	f=0.1653	264A ->266A	0.54648
5				
6	538.15 nm	f=0.1779	264A ->266A	0.54336
7	539.12 nm	f=0.1846	264A ->266A	0.55816
8	539.54 nm	f=0.2044	264A ->266A	0.56917
9	539.95 nm	f=0.1987	264A ->266A	0.57295
11	539.19 nm	f=0.1767	264A ->266A	0.57176
13	537.67 nm	f=0.1507	264A ->266A	0.56447
15	535.98 nm	f=0.1250	264A ->266A	0.55425
16	534.80 nm	f=0.1106	264A ->266A	0.54843
17	559.18 nm	f=0.3355	264B ->266B	0.88149
20	544.74 nm	f=0.4052	264B ->266B	0.86930

0GPa

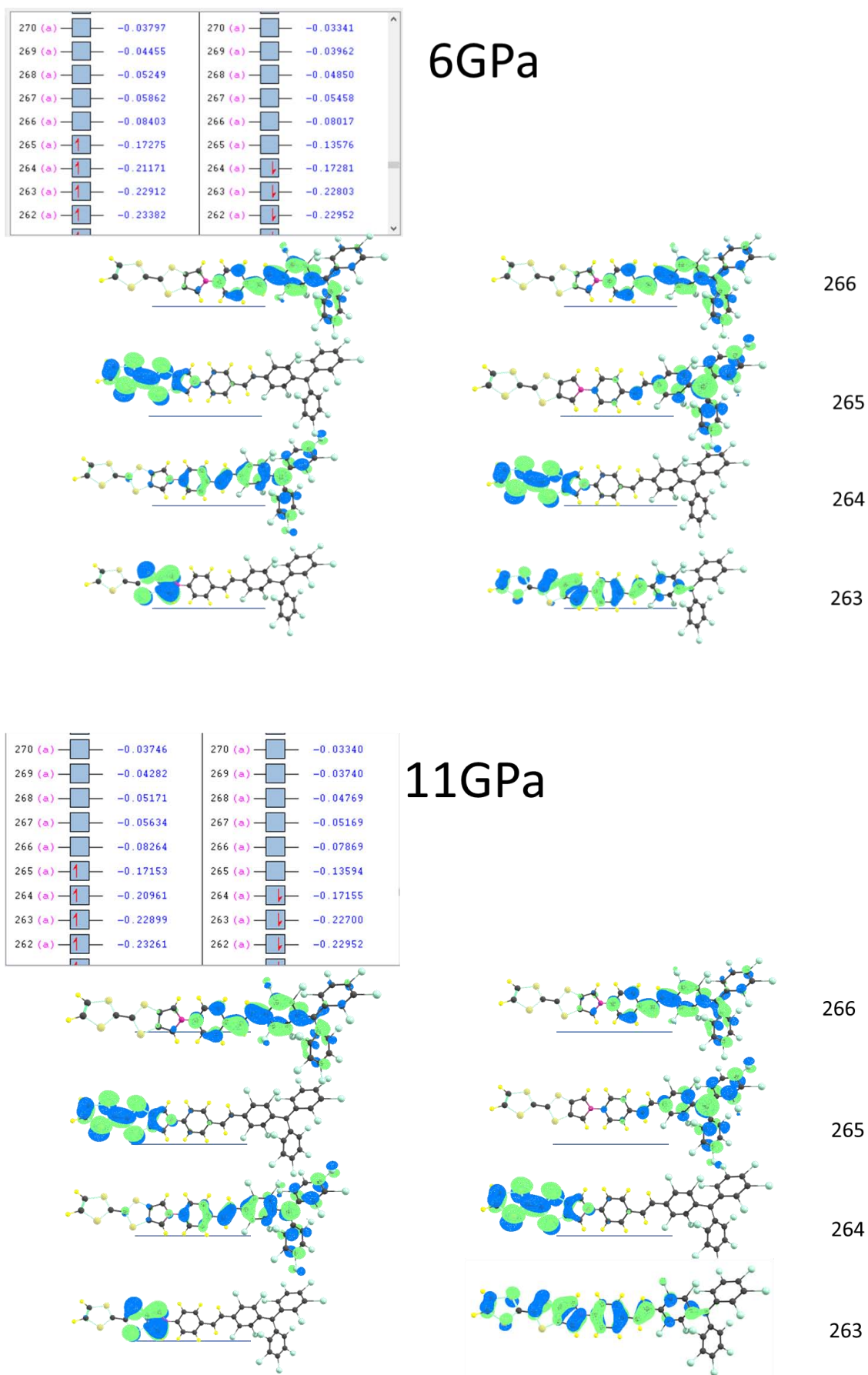| 270 (a) | −0.04410 | 270 (a) | −0.04045 |
269 (a)	−0.04897	269 (a)	−0.04536
268 (a)	−0.05624	268 (a)	−0.05298
267 (a)	−0.06129	267 (a)	−0.05726
266 (a)	−0.08389	266 (a)	−0.08020
265 (a)	−0.17560	265 (a)	−0.13612
264 (a)	−0.21742	264 (a)	−0.17568
263 (a)	−0.22932	263 (a)	−0.22921
262 (a)	−0.23666	262 (a)	−0.23083

266

265

264

263

Figure S27. Selected frontier orbitals of dyad **1** calculated at 0, 6 and 11 GPa.

10. Evolution of magnetic moment and spin density of 1 with pressure

The evolution of the magnetic moment in all radical dyad **1** (and for the MPTTF unit) was estimated from crystalline calculations observing that it changes only slightly with pressure. Indeed, the total magnetic moment of the dyad is reduced under pressure when the material becomes metallic in the calculations. MPTTF contribution is small (0.1 – 0.2) and even slightly decreased with the pressure.
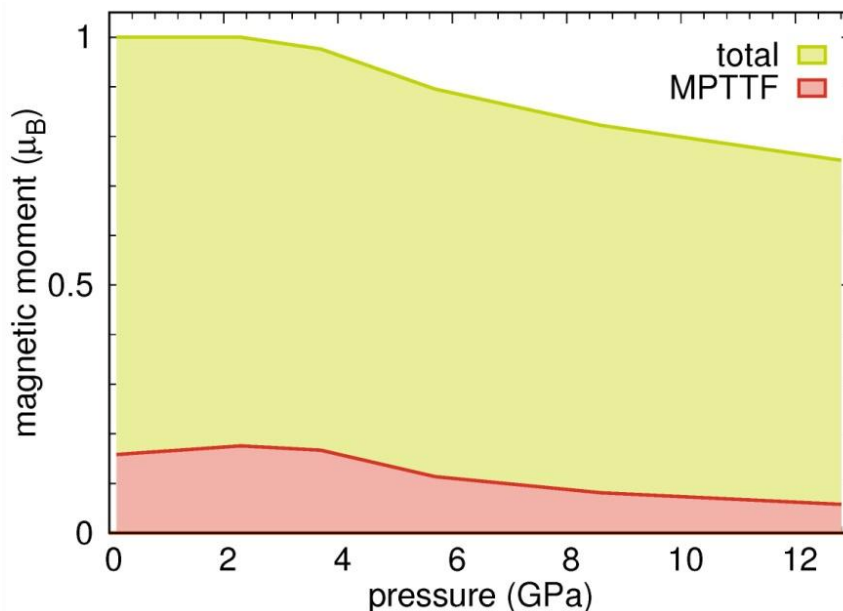

Figure S28. Evolution of the total magnetic moment (μ_B) of radical dyad **1** and for the MPTTF unit when increasing the pressure.

The spin density for a single molecule was calculated for comparison purpose. The geometry of the molecules was taken from the optimized crystal structures at different pressures within density functional theory calculations by performing relaxations of lattice parameters, monoclinic angle and internal atom positions at constant volume with the VASP code. Then over the taken molecular geometry for each pressure DFT single point calculations on at the UMo6/6-31G(d,p) level were conducted with Gaussian 09. The corresponding results are represented in Figure S29, were we have divided the molecule in several sections, as done along the manuscript. Initially at 0 GPa, the 94% spin density is located in the center C of the PTM radical. This radical character of the PTM remains with the increasing pressure and there is a minor decrease of the radical character in the PTM to 92%, which occurs by its proportional increase in the bridge and TTF units, 2% and 6% of radical character, respectively. Thus, we can see that although the spin density is mainly localized on the PTM moiety is slightly delocalized over the rest of the molecule.
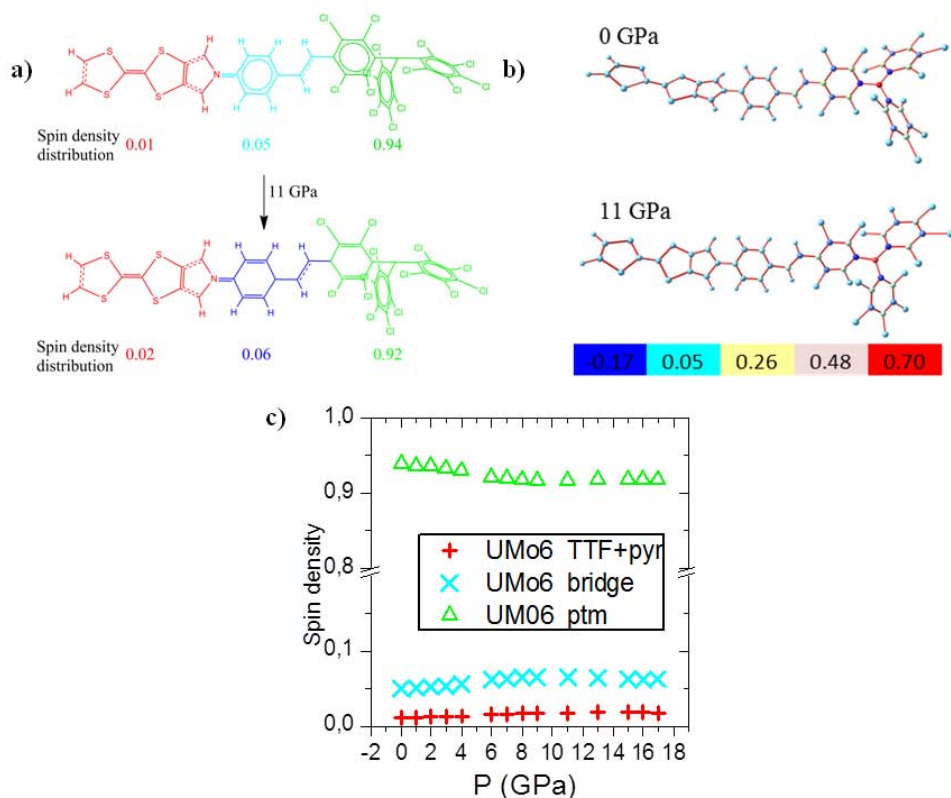
Figure S29. a) Valence bond representation of the a single molecule taken from the optimized crystal structures of **1** at different pressures within density functional theory calculations by performing relaxations of lattice parameters, monoclinic angle and internal atom positions at constant volume with the VASP code. Spin density as function pressure, for a single molecule is calculated at the UMo6/6-31G(d,p) level. b) Image of per-atom spin density, at 0 GPa and 11 GPa, the bottom chart corresponds to the color scale representing the spin density distribution. c) Spin density calculated for a single molecule of **1** at the UMo6/6-31G(d,p) level divided for the different molecular sections.

11. References

1. Souto, M.; Solano, M. V.; Jensen, M.; Bendixen, D.; Delchiaro, F.; Girlando, A.; Painelli, A.; Jeppesen, J. O.; Rovira, C.; Ratera, I.; Veciana, J. *Chem. Eur. J.* **2015**, *21*, 8816.

2. Cui, H.; Kobayashi, H.; Ishibashi, S.; Sasa, M.; Iwase, F.; Kato, R.; Kobayashi, A. *J. Am. Chem. Soc.* **2014**, *136* (21), 7619.

3. Kresse, G.; Hafner, J. *Phys. Rev. B* **1993**, *47*, 558.

4. Baonza, V. G.; Taravillo, M.; Arencibia, A.; Cáceres , M.; Núñez, J. *J. Raman Spectrosc.* **2003**, *34*, 264.

5. Zhao, Y.; Truhlar, D.G. *Theor Chem Account* **2006**, *120*, 215.

6. Gaussian 09, Revision A.02, M. J. Frisch, G. W. Trucks, H. B. Schlegel, G. E. Scuseria, M. A. Robb, J. R. Cheeseman, G. Scalmani, V. Barone, B. Mennucci, G. A. Petersson, H. Nakatsuji, M. Caricato, X. Li, H. P. Hratchian, A. F. Izmaylov, J. Bloino, G. Zheng, J. L. Sonnenberg, M. Hada, M. Ehara, K. Toyota, R. Fukuda, J. Hasegawa, M. Ishida, T. Nakajima, Y. Honda, O. Kitao, H. Nakai, T. Vreven, J. A. Montgomery, Jr., J. E. Peralta, F. Ogliaro, M. Bearpark, J. J. Heyd, E. Brothers, K. N. Kudin, V. N. Staroverov, R. Kobayashi, J. Normand, K. Raghavachari, A. Rendell, J. C. Burant, S. S. Iyengar, J. Tomasi, M. Cossi, N. Rega, J. M. Millam, M. Klene, J. E. Knox, J. B. Cross, V. Bakken, C. Adamo, J. Jaramillo, R. Gomperts, R. E. Stratmann, O. Yazyev, A. J. Austin, R. Cammi, C. Pomelli, J.

W. Ochterski, R. L. Martin, K. Morokuma, V. G. Zakrzewski, G. A. Voth, P. Salvador, J. J. Dannenberg, S. Dapprich, A. D. Daniels, O. Farkas, J. B. Foresman, J. V. Ortiz, J. Cioslowski, and D. J. Fox, Gaussian, Inc., Wallingford CT, **2009.**

7. Pulay, P.; Fogarasi, G.; Pongor, G.; Boggs, J. E.; Vargha, A. *J. Am. Chem. Soc.* **1983**, *105,* 7037.

8. http://www.chemcraftprog.com (browsed January 22nd, 2014)

9. http://gausssum.sourceforge.net/ (browsed January 22nd, 2014)

10. Rodríguez, S.; Nieto-Ortega, B.; González-Cano, R. C.; Lloveras, V.; Novoa, J. J.; Mota, F.; Vidal-Gancedo, J.; Rovira, C.; Veciana, J.; Del Corro, E.; Taravillo, M.; Baonza, V. G.; López-Navarrete, J. T.; Casado, J. *J. Chem. Phys.* **2014**, *140*, 164903/1-164903/9.

11. Del Corro, E.; González, J.; Taravillo, M.; Flahaut, E.; Baonza, V. G. *Nano Lett.* **2008**, *8*, 2215.